HARVARD UNIVERSITY
Graduate School of Arts and Sciences

DISSERTATION ACCEPTANCE CERTIFICATE

The undersigned, appointed by the

School of Engineering and Applied Sciences

have examined a dissertation entitled

"Aqueous solution synthesis of ZnO for applications in optoelectronics"

presented by : John Hwajong Joo

candidate for the degree of Doctor of Philosophy and here by certify that it is worthy of acceptance.

Signature _____

Typed name: Prof. E. Hu

Signature _____

Typed name: Prof. D. Clarke

Signature _____

Typed name: Prof. R. Westervelt

Date May 8, 2013

Aqueous solution synthesis of ZnO for application in optoelectronics

a dissertation presented
by
John Hwajong Joo
to
The School of Engineering and Applied Sciences

in partial fulfillment of the requirements
for the degree of
Doctor of Philosophy
in the subject of
Applied Physics

Harvard University
Cambridge, Massachusetts
May 2013

Thesis advisor: Evelyn L. Hu John Hwajong Joo

Aqueous solution synthesis of ZnO for application in optoelectronics

Abstract

Recently, ZnO has garnered widespread attention in the semiconductor community for its large set of useful properties, which include a wide bandgap and its resulting optical transparency, a large exciton binding energy, a significant piezoelectric response, and good electrical conductivity. In many ways, it shares many properties with a widely used and technologically important semiconductor GaN, which is widely used for blue LEDs and lasers. However, ZnO cannot substitute for GaN in most optoelectronic applications, because it cannot be doped p-type. On the other hand, unlike many traditional, covalently bonded semiconductors like GaN, ZnO can be easily formed aqueous solutions at close to room temperature and pressure in the form of large crystals or a variety of nanostructures, making possible applications that are normally very difficult with traditional semiconductors.

In this light, we aimed to take advantage of aqueous solution-based, ZnO growth techniques and incorporated ZnO structures novel optoelectronic and photonic structures. By controlling the morphology of ZnO, we studied the effects of nanowire-based ZnO/Cu_2O solar cells. Carrier collection was increased using a nanowire-based device architecture. The main result, however, was the time evolution of the performance of these devices due to the movement of ionized defects in the material. The effects of geometry on the ageing characteristics were studied, which

showed that the carrier collection could be increased further with ageing in a nanowire Cu_2O solar cell. The aging behavior was substantially different between nanowire and planar solar cells, which implies that future design of nanostructured solar cells must long term aging effects. In addition to solar cells, we explored the possibilities of using aqueous solution growth of ZnO to fabricated whispering gallery mode optical cavities and waveguides for enhancing extraction from a single photon source. In both applications, we used templated growth of ZnO to fabricate geometrically (near) perfect rods and disks for these photonics applications. Finally, since epitaxy is important in the process of optimizing device performance and fabrication, we showed the ability to grow ZnO epitaxially on single crystalline plates of Au, expanding the options of epitaxial substrates to include a metal.

Contents

Listing of figures

This work is dedicated to my parents, Eun Chu Joo and Jae Hoon Joo.

Acknowledgments

"Science is hard." It's something we say often in the lab and the office. And, it's true. But, it's also a lot of fun. It's even more fun when you have people around you who support and help you on the way. In fact, it would have been impossible for me to tackle even this tiny piece of science without them.

I first would like to thank my advisor, Evelyn Hu. When I started graduate school, I didn't really know what to expect. We were embarking on a completely new research project, doing research on biomineralization, in a group that had done nanofabrication on traditional semiconductor materials. Throughout graduate school, she has supported and trusted me, allowing me entertain all of the ridiculously crazy ideas that I have had, and has been wise enough to make me slow down and ask good questions before I got in too deep. She has allowed me to learn from the many mistakes that I have made, making me a more thoughtful researcher and person. She truly cares about the well-being of her students and so often puts her students' interests ahead of her own. I feel extremely blessed to have had the opportunity to be her student. We don't deserve her, but I am very glad that she has been our advisor.

I would also like to thank Elaine Haberer and Kasey Russell, two postdocs who I could talk to about anything related to graduate school. Elaine helped me navigate my time at UCSB as we worked together on the phage project and complained and encouraged each other on research, academia, science, and life. Kasey has been a

great mentor and sort of a big brother to me at Harvard. He has encouraged me when my project seemed to be failing, helped me think through research problems when they hit, introduced me to Python and climbing, and helped keep me sane and productive.

The subject of this whole thesis would not have gotten off the ground without my labmate, officemate, and friend at UCSB, Ridah Sabouni. On August 14, 2008, we made a little wager on whether silicon would have greater than 75% of the photovoltaics market share in 10 years. A few months later, to gloat, he forwarded me a thesis by Andersson who showed how precious the elements that made up the thin film solar cells were. A chart in that thesis started my thinking about solar cells made from Earth abundant elements, which led me to ZnO and my lunch buddy Jake Richardson. Jake had been working on aqueous solution synthesis of ZnO in Fred Lange's group and so we started a collaboration that sought to make ZnO/Cu_2O solar cells. When I moved to Harvard, I expanded my use of ZnO, but Jake taught me basically everything I know about ZnO. Thank you for your friendship, support, and selflessness, Jake. I'd also like to thank Jake's advisor, Prof. Fred Lange who was also very supportive in this whole endeavor even after we moved to Harvard. Unfortunately, he suddenly passed away during my second year at Harvard. I will always remember him for his generous intellectual spirit.

My other collaborators were both instrumental and inspirational in getting the work done. Mor Baram and Prof. David Clarke, thank you for helping me understand crystal structures and TEM and giving me confidence on my work. I would like to thank Jonathan Guyer from NIST for the FiPy help and Alberto Mittiga at ENEA for helpful discussions on the ZnO/Cu_2O work.

Thanks also to those in the group who directly worked with me on ZnO-related projects. Tsung-li, I will always be envious of your math skills, your mastery over device physics, your ever reliable insight, and your Costco card. Thanks for the late night video game sessions and, more seriously, the honest encouragement and evalution that you gave me. Katie and Scott, I have benefited greatly from your dedication to the ZnO project, your hard work, your new perspectives to the project, and your friendship. Nan, thank you for the late night discussions, exposing me to

nice restaurants, business, and what good karaoke sounds like. Thank you for your eagerness to work on science and collaborate. Your perseverence is an inspiration. Shanying, thank you for being the Tiger mom when I needed it, my workout partner, the object of my wrath as a safety officer, and a seriously great friend. You earned extra special thanks for pouring so much into helping me on my editing my thesis and preparing my defense presentation.

The Hu group has been my family for 8 years. We've had belly busting laughing and frustration cries. Many eras have ended as we've said goodbye to graduating students. I thank the family away from home that I have grown to love and depend on. Thanks to Jonathan, whose friendship I have relied on as we shared many late nights and weekends in the office and lab together. You've served as a great sounding board when discussing science problems as well as any other life issue under the sun. Thank you to the other groupmates who have shared a part of their lives with me: Liz, Fabian, Andrew, Yan, Sanden, Igor, Adele, Kelly, Kevin, David Rink, David Bracher, Yong-Seok, Chiou-fu, Christine, Alex Woolf, Alex Zhang, Tina, Danqing, and Andy.

I am grateful for the special friendship that I made at UCSB. Shawn and Natasha, we were kindred spirits at UCSB. I am grateful for all the interesting food, basketball, and interesting adventures we took as grad students. Your perspectives on life and your sense of style will always be a part of me. Will and Chris, thank you for bringing me into the community of Christ as a grad student at UCSB. Jake, Corey, and Josh, our lunchtime adventures every day were a welcome break that I looked forward to every day. (Corey, I can't believe you still have that dollar that you won off of me.) It was a little harder to make friends like these outside of the group at Harvard, but I'm glad that I got to be friends with Yinan, who introduced me to good Chinese food and history. I am always reminded me of what a "humble" person he is (mostly by him).

I would like to thank my apartment-mates at Antrim. Karen, Charles, and Jin, who have been my friends since the years at Northwestern, you were able to sympathize with me on my seemingly neverending work in grad school. Thank you for all of your support, pranks, jokes, and awesome cooking. Keith and Bryan, our

bond made through just that one year at Antrim has already shown to be stronger than many other friendships (although you'd never say it in such a mushy way).

I am indebted to the Christian communities that I was involved in at Santa Barbara and Cambridge. The Santa Barbara Community Church and Highrock Church have both given me communities of people that have supported me throughout my graduate studies. They have loved in such a way that it has been impossible for me to ignore the claims of Jesus. I thank them for showing me how much more there is to life than achievement.

Last but not least, I must acknowledge my family. I am grateful for my sister who supported me by mailing me new clothes, razors, and snacks as if I could not do these things myself. It turns out she was right for the most part. I am eternally grateful for the sacrifice and support that my parents have given me. They are typical immigrant parents, who have sacrificed everything and worked harder than I could ever work to provide me and my sister the opportunity to succeed in America. We went through some hard time together, but we were always together. They taught us what true perseverance meant. I thank them for the values that they have instilled in us. Those values have prepared us to tackle almost any problem but also made sure that we never forgot just how lucky and blessed we are. Thank you.

1

Introduction

When Jack Kilby[1] and Robert Noyce[2] separately invented the integrated circuit, it ushered in an age where millions of transistors could be made not one at a time but millions at a time, paving the way for the basis for all modern computation. Standard photolithography became the crucial element of the manufacturing process to make modern computer microchips, enabling us to produce computer

chips in a very similar way to the way we make books. However, for the last half century, in the same way that books must be printed on two-dimensional sheets of paper, the manufacturing process for computer chips often limited the design of computer chips to two-dimensional layers. As new forms of materials synthesis and fabrication now extend the control of structure in relevant materials to three dimensions, the architecture of devices must still be somewhat two-dimensionally based in order to be compatible with existing technologies and designs. Therefore, the ability to form controlled semiconducting or conducting nanostructures, in ways differenct from those used in the integrated circuits industry, has been critical for many new emerging technologies.

In the recent decades, the number of publications on ZnO have exploded[3]. At the same time the promises of "nanotechnology" garnered widespread attention and GaN was discovered as material for blue LEDs[4] and lasers[5], ZnO nanoparticles and thin films also started to become heavily investigated as a material to be used in optoelectronics. Better understanding of the properties of ZnO and the increased control of ZnO structure has fueled the dramatic increase in publications related to ZnO since the 1990s. ZnO, sharing many of the desirable properties as GaN, has been investigated as a low-cost replacement to GaN[6]. ZnO, like GaN[7], is a high bandgap material making it attractive for blue LEDs and lasers[8]. An exciton binding energy (60 meV[8]) that is greater than the room temperature thermal energy (26 meV[7]) is a major advantage of ZnO over other materials, making it possible to create a low threshold laser. It has an internal piezoelectric field, suitable for surface acoustic wave applications[9]. Highly conductive

ZnO can be achieved with proper doping, which has been used for creating transparent electronics[10, 11].

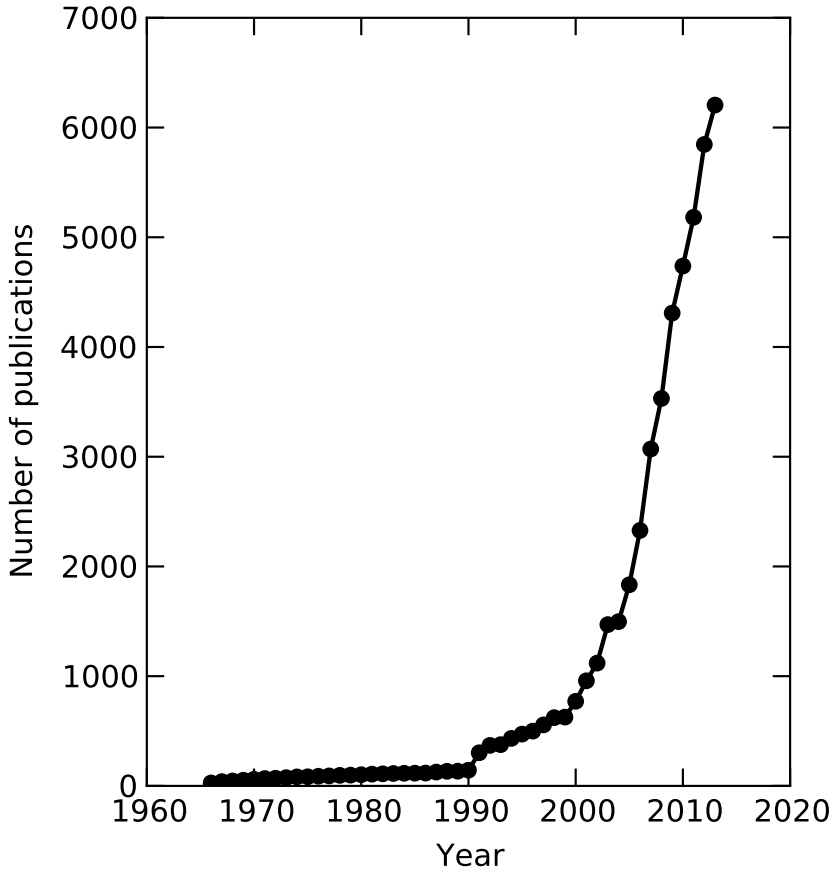

Figure 1.0.1: Number of ZnO publications by year, resulting from a search of "ZnO" in ISI Web of Science.[3]

Despite these attractive properties of ZnO for optoelectronic applications, ZnO remains a low-cost alternative to the more commonly employed material, GaN. However, ZnO cannot substitute for GaN in most applications, because it can-

not be doped p-type and remain stable[12]. Experimental reports of p-type doping usually come with the caveat that eventually the p-type doping degrades over time[13]. Although most optoelectronic devices rely on the presence of a p-n junction, n-type ZnO can be used creatively to form structures and devices without the need for p-type ZnO, such as some of the examples previously mentioned.

While ZnO as a powder has been long used in metallurgy, medicine, and as a pigment[14], newer applications that take advantage of these newly discovered or re-discovered properties have required ZnO to be used as a thin film. The ability to make fantastic new structures– ranging from nanowire arrays to stars and structures resembling UFOs[15–19]– also potentially enables even more exotic applications. Bottom up control of thin films and these ever more complicated nanostructures can be well-controlled, but making arbitrary structures in a well-controlled manner while integrating them into a thin film remains a challenge.

Already, the ability to control the morphology and grain size of ZnO in thin film form has proven to be critical to material properties and subsequent device performance. Conduction in a thin film of ZnO is partially dependent on the grain size of the crystals making up the thin film[20, 21]. Conduction electrons scatter off of or get trapped at grain boundaries[21, 22], impeding current flow and acting detrimentally on devices that depend on maximizing conduction in thin films of ZnO. Therefore, minimizing the grain boundaries in ZnO when used as transparent conducting oxide (TCO) in solar cell, light emitting diode (LED), and display applications is important. Control over the crystal direction in ZnO has enabled the utilization of the piezoelectric properties of ZnO in surface acoustic wave de-

vices (SAW)[9]. Without the ability to align ZnO crystals within a thin film, devices that rely on the piezoelectric response of ZnO would not be able to take full advantage of the additive effects of multiple ZnO crystals in a thin film.

The integration of three-dimensional structures with a two-dimensional film has been applied to varied field for improved device performance. ZnO "nanotips" have been used as excellent field emitters that avoid the problems of oxidation and radiation damage upon continued use[23]. Nanopiezoelectric generators can convert small amounts of mechanical energy into small amounts of electrical energy, making them ideal for implanted biomedical devices[24, 25]. ZnO nanostructures have been used as sensors for gas[26], liquid chemicals[27], and biomolecules[28–31], taking advantage of high surface area and changes in conductivity or mechanical resonance when specific molecules are adsorbed on the surface of ZnO. Furthermore, surface functionalization can tune the wettability of ZnO nanostructures from superhydrophillic to superhydrophobic. [32]

Nanowires have also been incorporated into ZnO films for optoelectronics purposes. Highly branched ZnO nanowires are used as an electrode in dye-sensitized solar cells (DSSCs), because they provide a large surface area for dye adsorption and direct pathways for charge transport. Still, power efficiencies of state-of-the-art DSSCs made from ZnO nanowire arrays still lag far behind those made with sintered TiO_2 nanoparticles[33]. Typical DSSCs use liquid electrolytes in order to achieve these high efficiencies. The drawback is that liquid electrolytes have lower thermal and chemical stability[23]. Attempts to use gel electrolytes to ameliorate the problems of liquid electrolytes have failed due to the difficulties of effectively

impregnating a sintered nanoparticle film with viscous gels[23]. ZnO nanowire arrays have performed better in DSSCs based on gel electrolytes, because the gel electrolyte can more easily penetrate the straight gaps between nanowires compared to the tortuous pathways found in the nanoparticle films. Thus, the spacing and morphology of the ZnO nanowire film become important to the ability to load the film with electrolyte and still maximize surface area for dye adsorption and, therefore, solar cell performance.

ZnO nanowires have also been incorporated in GaN LEDs to increase light extraction efficiency. In planar GaN LED structures, much of the light generated is trapped within the device. Only 3.3% of the internally generated in a planar GaN LED is extracted[34]. ZnO nanowire arrays grown on the top layer of the LED structure can improve the extraction efficiency by increasing the roughness on the surface of the LED, which allows much more of the light to approach the air/LED interface with an angle that is less than the critical angle for total internal reflection[23, 34]. The thin film of ZnO that supports the nanowire array can also be used as a current spreading layer in GaN LEDs, increasing the electrical performance of LEDs[35].

Despite these advances in incorporating 3D ZnO structures in 2D devices to increase the performance of optoelectronic devices, much more is possible. Most of the methods to create these ZnO films and nanowire arrays have been completely bottom-up. That is, the ZnO structure was made by atoms and molecules being assembled to create the resulting structure. Conversely, top-down approaches remove material until the desired structure is obtained. The bottom-up strategy re-

duces material waste and forms structures with often atomic precision but is limited to making simple structures. Top-down processing can make complicated, arbitrary structures with high precision and accuracy but can be very costly for large area applications and can damage important parts of the material during processing. By combining the bottom-up ability to alter ZnO growth and taking advantage of the top-down capabilities that have been the foundation of silicon microelectronics, new opportunities in ZnO optoelectronics can be uncovered.

1.1 Structure of this work

This work aims to expand the capabilities of ZnO in the realm of optoelectronics. Specifically, I will show how ZnO growth can be tailored by both bottom-up and top-down techniques to achieve desired structures for some optoelectronics applications.

In Chapter 2, I will highlight some of the important optical and electrical properties and the crystalline structure of ZnO. The basic concepts and techniques for the synthesis of ZnO nanostructures by aqueous synthesis methods will also be reviewed. In addition, past works on the control of ZnO growth will be reviewed.

We have already briefly reviewed how ZnO nanowire arrays have been used in DSSCs. In Chapter 3, we will discuss how we used ZnO nanowire arrays to increase the efficiency of fully solid-state solar cells, specifically for ZnO/Cu_2O solar cells. We will discuss how carrier collection increased with the incorporation of a nanostructured interface and the problems associated with ageing that were not as apparent in the planar version of these solar cells. The morphology and control

of morphology of the ZnO became important in being able to tune the efficiency parameters.

In order to more fully control the morphology of ZnO growth on substrates, we employed a combination of top-down lithographic process to template bottom-up growth of ZnO. Chapter 4 describes effort to grow ZnO patterned polymers and metals in order to build optical resonator structures and waveguides to enhance single photon collection. The growth of ZnO on patterned templates was found to depend on the type of material from which the template was made.

In Chapter 5, we describe a method to achieve epitaxial growth of ZnO on single crystalline Au microplates and methods to change the morphology of the ZnO film. Epitaxial films of ZnO on metal enabled the possibility of making better electrical contacts for devices and having precise control of crystal orientation of the grown ZnO. The quality of the interface was investigated through transmission electron microscopy (TEM) and atomic force microscopy (AFM), showing a rough but continuous epitaxial interface with periodic line defects.

Finally, Chapter 6 offers a summary of conclusions of the accomplished work in this thesis.

2

Review of ZnO properties and solution growth

This chapter is a review of ZnO optical and electrical properties and the solution growth of ZnO films and nanowires. We will focus on the role of surfaces on the optical and electrical properties of ZnO. Discussion on the solution growth of ZnO

will review the chemistry of the growth process and previous epitaxial thin films formed with ZnO grown in aqueous solutions. Finally, we end the chapter with a review of previous works of templated ZnO growth.

2.1 Crystalline structure

ZnO can crystallizes into two forms: the hexagonal wurtzite crystal structure and the cubic rocksalt crystal structure. The cubic rocksalt structure is a metastable phase and is seldom seen without high pressure synthesis or in ZnO nanocrystals[36, 37]. The hexagonal wurtzite crystal structure belongs to the C_{6v}^4 Schoenflies space group or the $P6_3mc$ in short standard notation[6]. The hexagonal unit cell of ZnO has lattice constants a = 0.325 nm and c = 0.52 nm and consists of two interpenetrating close-packed hexagonal lattices. The Zn sublattice is shifted along the c-axis from the O sublattice. Each Zn atom is surrounded by 4 O atoms in a slightly distorted tetrahedral configuration. The Zn-O distance along the c-axis direction (0.190 nm) is slightly smaller than the other three Zn-O distances (0.198 nm)[38].

The most referenced and important surfaces of the ZnO crystal are the basal planes (0001) and $(000\bar{1})$, the prism planes $(10\bar{1}0)$ and $(11\bar{2}0)$, and the pyramidal planes $(1\bar{1}02)$. The basal plane is often refered to as the c-plane. The c^+-plane refers to the (0001) plane, and the c^--plane refers to the $(000\bar{1})$. The low-index prism planes are known as the a-plane and m-plane, and the low-index pyramidal planes are known as the r-plane. Figure 2.1.1 shows where these low-index planes lie in the hexagonal crystal structure.

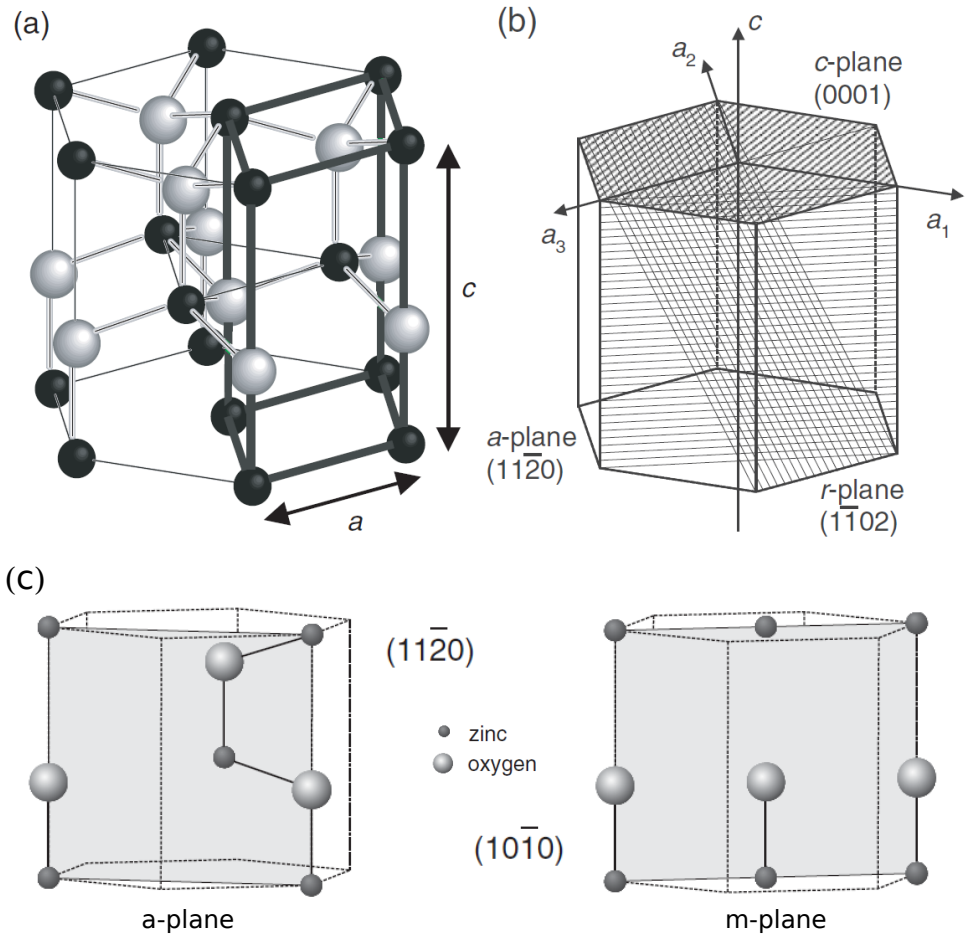

Figure 2.1.1: Crystal structure and important planes of ZnO. a) Heavy lines outline the primitive unit cell of the wurtzite lattice within the hexagonal prism. b) Selected surface planes are depicted in the schematic drawing. An example for a polar, non-polar, and semi-polar surface is selected. c) Both non-polar planes (a-plane and m-plane) are shown in the schematic.[6, 39]

In the model picture of a ZnO crystal, the (0001) plane is composed of Zn atoms only, while the $(000\bar{1})$ plane is only composed of O atoms. The non-zero dipole moment in the unit cell along the c-axis direction produces a diverging electrostatic surface energy with increasing crystal size, creating an unstable surface[39]. Compensation of the diverging electrostatic potential is possible through the rearrangement of charges at the surface through a variety of mechanisms: (1) creation of a metallic surface through surface states or excessive potential to create free carriers, (2) removal of surface atoms, and (3) adsorption of charge impurities at the surface [39, 40]. All of these mechanisms have been invoked for compensating charge on the polar surfaces of ZnO[40]. Regardless, the polar surface of ZnO is a feature in the ZnO crystal structure that strongly influences electronic and piezoelectric properties and growth behavior in ZnO.

2.2 Optical properties

ZnO has become an alternative material to GaN, because their fundamental band gap energies are very close to each other – ZnO has a fundamental direct band gap energy of 3.37 eV[8]; GaN's fundmental direct band gap is 3.4 eV[7] – making both materials suitable for UV optoelectronics devices. An advantage of ZnO over GaN is that it has a exciton binding energy that is substantially larger than thermal energy at room temperature. ZnO's exciton binding energy is 60 meV[8], while GaN's exciton binding energy is only 18-28 meV[6]. Since thermal energy at room temperature is 26 meV, excitons in GaN are easily dissociated by thermal energy, while excitons in ZnO can stay bound. Conseqeuently, stimulated excitonic

emission in ZnO devices is possible at room temperature, but may be impossible in pure GaN devices[41].

Many ZnO defects also emit in the visible wavelength range and, therefore, can greatly influence overall emission characteristics of any forthcoming optical device. The deep level emission from these defects can be divided into emission from extrinsic and intrinic defects. Native defects in ZnO include oxygen vacancies (V_O), zinc vacancies (V_{Zn}), oxygen interstitials (O_i), zinc interstitials (Zn_i), oxygen anti-sites (O_{Zn}), and zinc anti-sites (Zn_O)[42, 43]. Defect complexes or clusters can also form when two or more defects bind to each other like V_OZn_i[42, 43]. Extrinsic defects refer to defects in the crystal lattice that are the result of incorporation of an atom that is neither zinc or oxygen. Common impurities that originate deep level emission are Li, Cu, Fe, Mn, and OH[42, 44, 45].

The most common bands due to deep level emission are the green, yellow, and red luminescence bands[42]. The green band is the most common and emits at energies of 2.4-2.5 eV[42]. It is the most studied band and, in regards to understanding the origin, the most controversial. Many authors have suggested that zinc vacancies are the single source responsible for the green band luminescence[46–48]. Among the intrinsic defects in ZnO, V_{Zn} has the lowest formation energy in n-type ZnO[43]. In thermodynamic equilibrium, the concentration of point defects is related to the formation energy by [43]

$$c = N_{sites} exp\left(\frac{E^f}{k_B T}\right), \tag{2.1}$$

where c is the defect concentration, E^f is the formation energy, N_{sites} is the number

of available sites where the defect can form, k_B is Boltzmann's constant, and T is the temperature. Therefore, the concentration of V_{Zn} should be the highest among the intrinsic defects. Zinc vacancies occupy an energy level 0.9 eV above the valence band minima, yielding emission of 2.4 eV when transitions occur between the conduction band and the defect[43]. In positron annihiliation spectroscopy studies, it was confirmed that zinc vacancies were the dominant defect in electron-irradiated n-ZnO samples[49, 50]. Other defects including oxygen vacancies, zinc interstitials, and extrinsic defects that include copper have also been suggested as the source of the green luminescence band in ZnO[44, 45, 51]. There is also increasing evidence that the green luminescence is located at the surface[52, 53].

The yellow luminescence band appears at 2.2 eV. At first, it was entirely attributed to Li dopants and impurities, which appear 0.8 eV above the valence band and are considered deep acceptors in ZnO[54, 55]. However, experiments in which the green luminescence was bleached revealed a yellow luminescence band, suggesting that the yellow emission band is always present at a low density[45]. The yellow emission observed in aqueously grown ZnO nanorods have been attributed to O_i or Li impurities[56]. Residual $Zn(OH)_2$ groups on the surface of ZnO nanorods have also been proposed as the source of the yellow luminescence in solution grown ZnO nanorods[57]. Post-annealing of the solution grown ZnO can eliminate the yellow emission band by desorbing the OH groups on the surface of ZnO[57], although eventually it can be replaced by orange, orange-red, and red luminescence[57]. Orange luminescence, rarely seen in ZnO, is attributed to oxgyen interstitials[58]. Orange-red luminescence is attributed to zinc vacancy complexes[59]. Zinc inter-

stitials are proposed to the be the origin of red luminescence[53].

2.2.1 The surface

Photoluminescence (PL) from various ZnO nanostructures results in variations in the position and intensity of the peak. The room temperature near band-edge PL for ZnO nanostructures has been reported at 373, 378, 380, 381, 383, 384-391, 387.5, 389, and 390 nm[60]. Time-resolved PL has shown that defect densities on ZnO nanostructures with high surface-to-volume ratios can also be very different from the bulk. Even when the sizes of ZnO nanostructures are larger than the Bohr radius of ZnO[61], the critical size for the manifestation of quantum confinement effects, a blue shift in the near band-edge luminescence can be observed in several systems[19, 62, 63]. It has been proposed that the blue-shift in these systems are the result of surface effects[60].

As mentioned earlier, the often observed green band luminescence is often attributed to surface effects. In experiments with aligned ZnO nanorods, polarization-dependent PL showed that the near band-edge emission in the UV and the green band emission were both highly polarized[64]. The intensity of the UV emission was maximum in the c-axis direction of the ZnO nanorod, while the green emission was minimum in the same direction. The polarization-dependent emission provided information to identify that the green emission mostly occurs at surface defects on the nanorods. Additionally, the green band could be suppressed by coating the surface of nanostructures with a surfactant[65]. Analysis on the radius of nanowires also showed that once a nanowire becomes thin enough, the near

band-edge emission can be completely quenched by the surface recombination[66]. Furthermore, because of the high absorption coefficient for photons in ZnO, most excitons are generated near the surface of the material, increasing the probability of interaction with surface defects. Consequently, surface defects are incredibly important to the emission properties of ZnO nanostructures.

2.3 Electrical properties

ZnO is often used as a transparent conducting oxide and in thin film transistors because of its superior electrical properties. The mobility for single crystal ZnO needles was first characterized by Hutson from Bell Labs in 1957 [67]. The room temperature mobilities for his crystals with carrier concentrations lower than 10^{17} cm^{-3} were 180 $cm^2V^{-1}s^{-1}$. It is a testament to the high quality of crystal growth achieved by Hutson in 1957 that the room temperature mobility of single crystal ZnO has not improved much since then.

As doping levels in ZnO increase, scattering due to ionized impurity atoms increases causes mobility to decrease. Mobility *meta*-data from single crystal ZnO were collected by Ellmer as a function of carrier concentrations as low as 10^{15} cm^{-3} in undoped ZnO to as high as 7 x 10^{19} cm^{-3} in indium-doped ZnO (See Figure 2.6 in [21]). Scatter in the data is high between carrier concentrations between 10^{17} to 5 x 10^{18} cm^{-3}, but they range from 70-150 $cm^2V^{-1}s^{-1}$. The highest reported mobilities are in the 220-225 $cm^2V^{-1}s^{-1}$ range. The low mobility value compared to Si (1415 $cm^2V^{-1}s^{-1}$) or GaAs (8500 $cm^2V^{-1}s^{-1}$)[21] is due to the strong polar optical scattering in ZnO. The functional relationship between mobility and car-

rier concentration can be described by the empirical equation originally derived for silicon[68]:

$$\mu = \mu_{min} + \frac{\mu_{max} - \mu_{min}}{1 + (n/n_{ref_1})^{a_1}} - \frac{\mu_1}{1 + (n/n_{ref_2})^{a_2}}, \tag{2.2}$$

where μ is the mobility of electrons; μ_{max} is the lattice mobility at low carrier concentrations; μ_{min} is the ionized impurity mobility at high carrier concentrations; ($\mu_{max} - \mu_1$ is the clustering mobility at very high carrier concentrations, n is the carrier concentration; and a_1, a_2, n_{ref_1} and n_{ref_2} are fitting parameters.

In comparison to single crystal ZnO, polycrystalline ZnO thin films have much lower mobilities of 10 $cm^2V^{-1}s^{-1}$[69]. Epitaxially grown ZnO on c-plane GaN through aqueous solution deposition has a mobility of 70 $cm^2V^{-1}s^{-1}$ with a carrier concentration of 2.3 x 10^{19} cm^3[35], which corresponds to other single crystalline ZnO at similar carrier concentration levels. Polycrystalline ZnO grown by aqueous solution methods exhibits lower mobilities of 7 $cm^2V^{-1}s^{-1}$[70]. The grain size of these films plays an important role in the mobility and electrical properties of these films, since the grain boundaries are the site of electron traps and scattering events[22]. Some authors however have reported unusually high mobilities and low resistivities for polycrystalline films[71, 72], although the reason for these electrical characteristics remains unclear.

The other major contributor to the conductivity of a film is the carrier concentration, which is determined by the effectiveness of doping of the material. ZnO is typically unintentionally doped n-type[73, 74] and very difficult to dope p-type[12]. Extrinsic n-type doping of ZnO by group-III elements B, Al, In, and

Ga have been used to make degenerately doped ZnO, increasing conductivity by orders of magnitude[60]. Currently, Al-doped ZnO is often used as a low cost alternative to tin-doped indium oxide (ITO) for use in thin film solar cells[75].

Yet, the most important dopant in ZnO is hydrogen. Hydrogen is present in nearly all growth processes; and due to its small size, it is incredibly difficult to isolate it from ZnO. While the role of hydrogen as a shallow donor was discovered in the 1950s[76–78], the knowledge was forgotten for several decades. Instead, intrinsic defects like oxygen vacancies and zinc interstitials[79] (and references therein) were thought to be source of the n-type conductivity in ZnO. In 2000, van de Walle[80] showed that hydrogen always acts as a shallow donor in ZnO through a density functional theory study. In 2002, Hofmann et al.[81] confirmed experimentally that hydrogen was a shallow donor in nominally undoped ZnO single crystals using electron paramagnetic resonance and Hall measurements. In aqueously grown ZnO, hydrogen is readily incorporated into the lattice during growth as residual water or $Zn(OH)_2$[57, 82]. Upon annealing at 200-250°C, trapped hydrogen is activated and serves as a dopant, thereby dramatically increasing the conductivity of ZnO[83] in some cases so much that the conductivity rivals ITO without the need for intentional extrinsic doping[35]. In some cases of doping ZnO with hydrogen, the conductivity was observed to increase over time, although it was attributed to chemisorption of oxygen and water at grain boundaries and surfaces rather than diffusion of excess hydrogen[84].

2.3.1 The surface

The state of the surface of ZnO affects the electical transport behavior, especially in nanostructured ZnO. The switching of the transport behavior is strongly correlated to the presence of adsorbed oxygen at the surface of ZnO. A common theory is that when oxygen molecules chemisorb onto the surface of ZnO, they capture electrons from the lattice, depleting the surface of free electrons [$O_2(g) + e^- \rightarrow O_2^-(ad)$] and forming an electronic depletion layer at the surface[60]. The surface depletion of free electrons decreases the surface conductivity and can dramatically affect the carrier concentration in nanowires if they become fully depleted. Furthermore, the mobility of carriers is affected by scattering and trapping by the newly formed surface states. The surface can be restored with heating in a vacuum or inert gas[85], UV light exposure[86], or exposure to reductive gases, like ethanol, H_2, CO, or H_2S[60, 87]. These surface treatments cause the adsorbed oxygen molecule to desorb from the surface of the ZnO, restoring the original conductivity of the surface.

However, a significant drop in conductivity due to oxygen exposure can be measured even when the thickness of the sample is much larger than the thickness of the depletion layer. Instead, it has been proposed that a highly conducting surface layer, which has a higher conductivity than the bulk, is eliminated or masked by the presence of the adsorbed oxygen molecules[88]. The origin of the highly conducting surface layer is not well known. It has been hypothesized that a high density of oxygen vacancies, generated by ambient light, could create the conducting layer[87]. Other pre-existing positively charged donors could be drawn

to the surface, forming the conducting layer, by the adsorbed negatively charged oxygen[87]. Mobile donors could be hydrogen or other group III dopants. Evidence of the accumulation of group III dopants at the surface was found through secondary ion mass spectroscopy (SIMS)[89]. X-ray photoelectron spectroscopy and electron irradiation experiments have also demonstrated accumulation of hydrogen donors near the surface[90].

2.4 Growth of ZnO in aqueous solution

ZnO thin films can be made through conventional thin film deposition techniques that include magnetron sputtering[91], chemical vapor deposition[92], pulsed-laser deposition[93], molecular beam epitaxy[94], and atomic layer deposition[95]. Other methods not generally available to more traditional, covalently bonded, semiconductor materials are methods that rely on chemical reactions and solution depositions including spray-pyrolysis[96], electrodeposition[97], and sol-gel deposition [98], hydrothermal deposition[99], and chemical bath deposition (CBD)[100].

In this section, we will describe some of the details of low temperature aqueous ZnO synthesis. This technique shares many features with chemical bath deposition, where the desired material is deposited on a substrate via an *in situ* chemical reaction typically in an aqueous solution. Unlike chemical bath deposition, this technique does not take place in an open bath. Instead, the deposition occurs in a closed container, in which the pressure can increase to above atmospheric pressure. Under these conditions, growth is expected to proceed in a manner similar to hydrothermal growth, where solubility of ZnO is greater and growth is typically

slower[100].

Typically, the synthesis begins with the seeding of the substrate with nanocrystalline ZnO. The seed layer can be synthesized through the decomposition of a solution deposited zinc-organic precursor[101], the solution deposition of preformed ZnO nanoparticles[102], or vapor deposition. The aqueous growth step slowly grows ZnO from a supersaturated solution onto any existing ZnO surface, since growth of ZnO on ZnO requires a smaller driving force than either the growth of ZnO on a foreign surface or the homogenous nucleation of ZnO in solution[103]. Growth occurs preferentially in the c-direction of ZnO, in the absence of any additives, because the polar faces in ZnO have the highest surface energies[104]. As a result, arrays of nanowires are formed on the substrate. The orientation of the nanowires are subject to the orientation of the initially deposited seed layer. It is also possible to skip the deposition of the seed layer by forcing heterogenous nucleation on the substrate during the aqueous growth step[105].

The growth process is affected by the specifics of the solution, such as the choice of ligand, pH, zinc counter-ion, ionic strength, and other parameters, like the temperature, the substrate, and concentration of the zinc salt. Details of how these can affect ZnO growth can be found in the work by Govender et al.[100] However, the general solution chemistry can be summarized. Zn^{2+} cations are dissolved in an aqueous solution, which are solvated by water, resulting in aqua-ions $[Zn(OH_2)_n]^{2+}$. The aqua-ion undergoes hydrolysis, because the polarized M-OH_2 bond facilitates the deprotonation of the attached water. A range of monomeric species can exist, depending on how many waters are solvating the cation with the

general form of $[Zn(OH_2)_{n-p}(OH)_p]^{(2-p)+}$, also written as $[M(OH)_p]$ by omitting the water. Condensation reactions occur for the polynuclear species which eventually become ZnO. The first step is called olation, where an "ol" bridge is formed:

$$M - OH + M - OH_2 \rightarrow M - OH - M + H_2O. \tag{2.3}$$

The second step is oxolation, where dehydration of the hydroxo-species results in an "oxo" bridge:

$$M_2 - (OH)_2 \rightarrow M - O - M + H_2O. \tag{2.4}$$

Often, in literature, hexamine, also known as hexamethylenetetramine (HMT), is used as a pH buffer[100]. Hexamine slowly decomposes into formaldehyde and ammonia, which increases the pH of the solution, forcing hydrolysis of the aquaions in solution and eventually leading to the formation of ZnO.

Ammonia also serves as a complexing ligand for Zn ions. Other ligands like ethylenediamine and triethanolamine[100] have been used in ZnO growth. Richardson and Lange analyzed the thermodyamics of aqueous ZnO solution growth using ammonia as the ligand, because it appears to be the fundamental unit for the other complexing ligands that are also often used[106]. They found that the zinc-amine complex that is formed in solution causes ZnO to have retrograde solubility. As the temperature of the solution is raised to 90°C, the solubility of the Zn ions surprisingly decreases. As the reaction vessel is slowly heated, ZnO becomes supersaturated slowly and growth proceeds to alleviate the supersaturation of ZnO

in solution.

In order to achieve thin coalesced films of ZnO, citrate is used to slow the c-axis growth. Citrate ions bind to the (0001) surface of ZnO and block access to the surface from zinc ions. As a result, increasing the concentration of citrate ions decreases the height-to-width ratio of the ZnO crystals that are formed[107]. At very high citrate concentrations, layered structures form instead of monolithic ZnO pillars or plates[107]. A consequence of using citrate ions at low concentration is the ability to shape the tips of ZnO needles. Normally without the use of citrate, ZnO needles have pointed tips. Those tips become flat with the inclusion of citrate, which may be useful when using similar synthesis technique to make field emitters, where a sharp tip is desired[108], or piezoelectric nanogenerators, where a flat top is desired for making electrical contact[25, 109].

The ability to coalesce ZnO crystals on a substrate to make thin films has allowed exploration into finding epitaxial relationships with some substrates. Substrates with similar crystal structures, like c-plane GaN and (111) $MgAl_2O_4$ have been used to form epitaxial thin films of ZnO[35, 110–112]. Epitaxial thin films of ZnO on c-plane GaN have been used as a current spreading layer in GaN-based LEDs, with performance equivalent to the more expensive alternative of ITO[35, 112]. More applications for epitaxial ZnO in electronics and optoelectronics is expected to be forthcoming.

Photolithography was also used to mask the surface of the substrate to create lateral epitaxial overgrowth (LEO) films[113]. Similar to LEO films in GaN, the overgrown regions had fewer dislocations than the regions grown directly from the

substrate. Patterned growth was also possible on epitaxial films to form microrods and microtunnels, because, unlike films seeded by randomly oriented nanocrystalline ZnO, the direction of vertical growth was defined by the epitaxial relation to the substrate[114].

3

Effects of nanowire morphology on the aging of ZnO/Cu_2O solar cells

3.1 Introduction

Although invented almost 200 years ago[115], solar cells remain an attractive method of converting solar energy into electrical energy. The problem remains that photo-

voltaics, in their current form, are still too expensive to overthrow fossil fuels like coal and natural gas from the dominant position that they have established themselves in over the last 100 years. For practical economic reasons, the figure of merit has become Watts per dollar, in efforts to truly reflect the costs of electricity from solar cells. The costs for solar cells have dropped in the recent years, obtaining a cost curve similar to Moore's Law[116, 117]. Still, concerns over the toxicity of Cd[118, 119] and the material scarcity of Te[120] in CdTe solar cells and the high capital costs for Si solar cells[121] have pushed researchers to look for alternative materials for solar cells.

Among the materials with the highest potential for making efficient but extremely cheap solar cells is Cu_2O [122, 123]. If solar cells are to supply the energy with a significant fraction of its energy demand, the solar cell must consist of materials that are abundant and easy to process. A survey done by Anderson[123] (Figure 3.1.1) shows that the copper is an element that is both widely available in the Earth's crust and that has the established infrastructure to extract large quantities.

Cuprous oxide's (Cu_2O) non-toxic nature, its abundance, and simple processing made it extremely attractive as a potential solar cell material in the 1970s and 1980s[124–128]. The theoretical maximum efficiency has been estimated to be as high as 20%[128]. It has a direct band gap of 2.0 eV[1][129, 130], making it a good candidate for the top cell in a multijunction solar cell. However, Cu_2O could

[1] Cu_2O actually has a direct forbidden bandgap, which means that electric dipole transitions are forbidden at the absorption edge due to parity selection rules even though the bottom of the conduction band and top of the valence band occur at the zone center. The transition is only disallowed at the critical k=0 point. As a result, absorption is better than indirect bandgap semiconductor but worse than normal direct bandgap semiconductors.

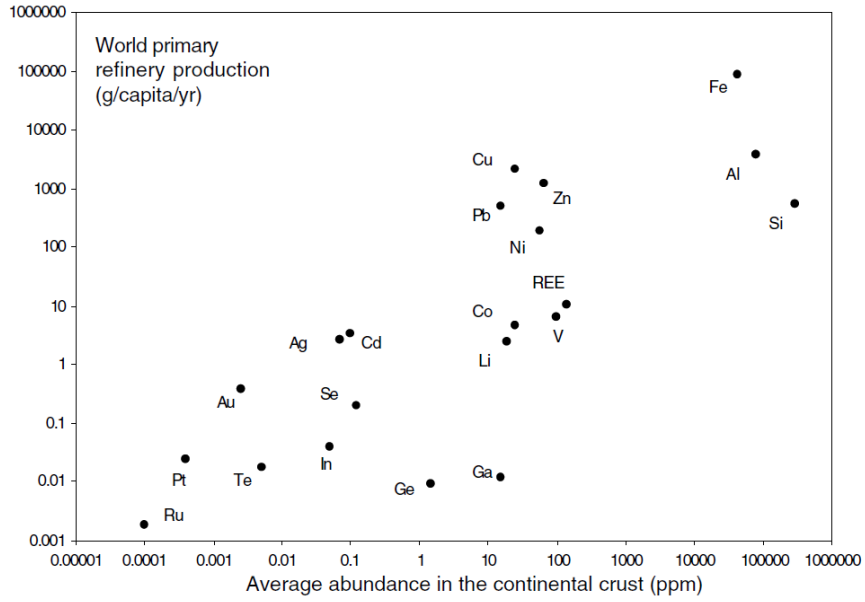

Figure 3.1.1: Metal abundance in the Earth's crust and metal use in society.[122]

not be doped n-type, making homojunction impossible. It became clear that a heterojunction device was necessary to maximize the potential efficiency. ZnO became the material of choice as the n-type complement to the inherently p-type Cu_2O[125, 131–133].

The method of deposition for Cu_2O has been an important factor in determining the final efficiency of the device. Cu_2O can be grown using inexpensive methods such as electrochemical deposition[134, 135], hydrothermal growth[136, 137], chemical solution deposition[138], or high temperature oxidation of copper[139]. However, substantial increases in efficiency have been observed only for ZnO/Cu_2O solar cells made through the furnace oxidation of Cu. The efficiency of solar cells made through the electrochemical deposition of Cu_2O have remained low[140–

144]. Smaller grain sizes, the inability to increase carrier concentration through extrinsic dopants, and more defective interface states are all barriers for creating high efficiency devices through electrodeposition.

Due to the lower crystalline quality and smaller diffusion length in solution deposited Cu_2O, an effort to increase the efficiency of ZnO/Cu_2O solar cells has led to the incorporation of nanowires into the solar cell structure. Planar solar cells must have a minority carrier diffusion length on the order of the optical absorption length if one hopes to efficiently collect most of the photoexcited carriers. On the other hand, nanowire solar cells have shown potential in improving solar cell efficiencies by enabling increased light absorption while retaining efficient carrier collection. Using a nanowire structure, the thickness of the absorber layer is no longer limited to the minority carrier diffusion length. The photogenerated carriers no longer travel the same path as the incident photon. Instead, the carriers have a much shorter distance to travel to reach a nanowire junction. Despite observing increased carrier collection compared to planar structures[145–154], efficiencies of nanowire ZnO/Cu_2O solar cells are still well below the record 4% efficient ZnO/Cu_2O solar cells[155].

Many studies have drawn attention to the additional design considerations needed for nanowire solar cells[146, 156–161]. Light manangement schemes may be developed by engineering the nanowire dimensions and placement within the Cu_2O matrix to increase photon absorption[162]. Musselman et al. have done considerable work in developing design rules for the charge transport within ZnO/Cu_2O solar cells[146, 161]. They found that, although the nanowires do increase charge

collection, the high density of nanowires inhibits the formation of the full built-in potential, effectively restricting the open circuit voltage. The diffusion length for Cu_2O is less than 1 μm, but more than 2 μm of Cu_2O are required to sustain the full built-in potential. Additionally, the increase junction area leads to a larger leakage current, which can have further deleterious effects on the built-in potential. A more detailed explanation is save for the following section.

In order to be viable as a useful solar cell, ZnO/Cu_2O solar cells must also be stable for long periods of time. While it may seem that oxides are inherently stable in atmospheric conditions because the materials are already oxidized, oxides are famously known to have ionic conductivity and to be very sensitive to defects[163]. Some exploration has been done regarding the aging of ZnO/Cu_2O solar cells, however we are not aware of any studies regarding the aging of nanowire-based solar cells. In the work on planar ZnO/Cu_2O solar cells, persistent photoconductivity and the movement of copper vacancies in Cu_2O have been investigated through capacitance transients[164].

In this work, we created both nanowire and planar ZnO/Cu_2O solar cells through aqueous deposition methods. ZnO deposition was controlled through solution chemistry to yield either nanowire arrays or coalesced, polycrystalline thin films. The relative ease of forming and controlling both structures of ZnO allowed us to fairly compare the performance of the resulting solar cells. Furthermore, we investigated how the nanowire architecture of ZnO/Cu_2O solar cells affected aging and their performance over time. We show that the movement of copper vacancies by the internal electric field affects the performance of nanowire solar cells very differ-

ently from planar solar cells. We believe that the results from this relatively simple material system helps broaden our understanding in ionic photoconductive materials, where ionized dopant atoms are not necessarily fixed in the lattice. The results also have implications on the future design of nanowire solar cells made from non-traditional semiconductor materials.

3.2 The Ideal Solar Cell

A solar cell is a device that creates an electrical current due to the absorption of photons in a material. Semiconductor p-n junctions are often used to create the driving force necessary to separate photoexcited holes and electrons. The p-n junction creates an internal electric field at the junction that drives the separation of electrons and holes. The equilibrium band diagram is defined by the Poisson equation:

$$\bigtriangledown^2\phi = -\frac{\rho}{\varepsilon}, \tag{3.1}$$

where ϕ is the electric potential, ρ is the charge density, and ε is the permittivity of the medium. In the depletion approximation, we assume that there are no free carriers within the charged regions surrounding the junction. This region, "depleted" of majority carriers, is called the depletion region (Figure 3.2.1). As a result of the approximation, the potential drop is confined within the depletion region near the junction, and the electric field vanishes to zero beyond the boundaries of the depletion region, leaving the remainder of the p- and n-type regions neutral. Since the internal electric field is confined to the depletion region, minority carriers can

only move outside of the depletion region through diffusion.

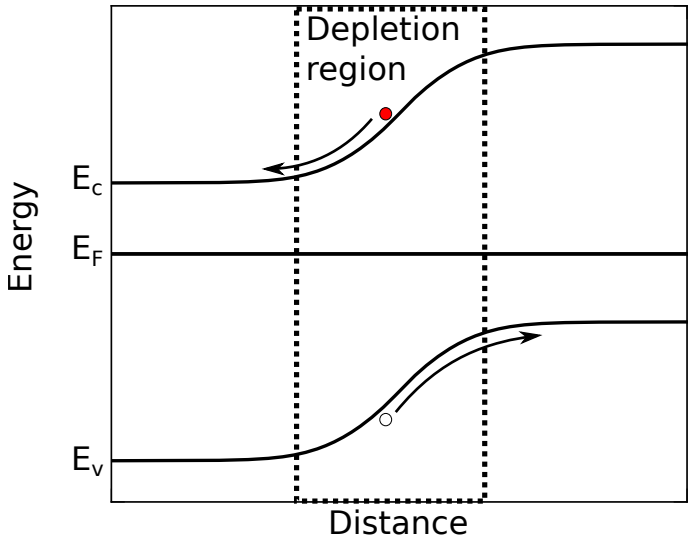

Figure 3.2.1: Schematic of model p-n junction. The depletion region is marked in dashed lines. E_c is the conduction band, E_v is the valence band, and E_F is the Fermi level. The red abd white circles depict an electron and hole, respectively.

In an ideal solar cell, light is incident on a p-n junction. The amount of electron-hole pairs that are created at a specific depth is described by the Beer's Law:

$$I(x) = I(0)exp(-a(\lambda)x), \tag{3.2}$$

where $I(x)$ is the intensity of light that has penetrated a distance x into the material, $I(0)$ is the intensity of the light incident on the material, and $a(\lambda)$ is the wavelength-dependent absorption coefficient of the material. Carriers that are generated within the depletion region are considered to be collected with 100% efficiency. The limiting factor in the collection of all carriers is considered to be the diffusion length of the minority carriers. If carriers cannot diffuse to the junctions

and instead recombine, the energy from those excited carriers is lost and cannot contribute to the energy output of the device.

A common method to evaluate the ability for the device to collect the photogenerated carriers is through a measurement of external quantum efficiency (EQE). EQE is the probability that an incident photon of a certain wavelength will deliver an electron to the external circuit. It is determined by measuring the current generated by monochromatic light of a known intensity. EQE is a product of the photon absorption probability and carrier collection probability.

Solar cells are often designed with a thin, heavily doped, n-type layer closer to the surface followed by a thick, lightly doped, p-type layer. Since short wavelength photons have high absorption coefficients in most crystalline materials, they are absorbed near the surface of the solar cell; and since the junction is close to the surface, carriers generated by these short wavelength photons are easily collected. Therefore, the EQE is nearly 100% for highly efficient solar cells in the spectral range that is above the bandgap of the material. As the absorption coefficient decreases for longer wavelength photons, the depth at which most of the photons are absorbed increases. Eventually, the wavelength of light is long enough such that most of the photons are generated beyond the depletion region and beyond the minority carrier diffusion length. As the electron-hole pairs are generated deeper within the device, the collection probability of the minority carriers decreases, which causes EQE to decrease. The rate that the EQE decreases with increasing wavelength often follows the absorption curve for the material.

The short circuit current density (J_{sc}) is the current density measured when the

solar cell is measured in AM 1.5 light under 1 Sun illumination without an applied bias. AM 1.5 described the spectrum of light incident on the Earth's surface if the sun was at an angle of elevation of 42°; it is the standard for solar cell measurements. 1 Sun illumination corresponds to an integrated irradiance of 1000 W/m². J_{sc} can also be obtained by the EQE and incident spectral photon flux density, $b_s(E)$:

$$J_{sc} = q \int b_s(E) EQE(E) dE, \tag{3.3}$$

where E is the photon energy and q is the charge of an electron.

While a solar cell can be considered a current generator, we often apply a voltage to simulate the presence of a load. The current density vs. voltage curve then provides information about the power efficiency of the device. The ideal p-n junction solar cell is described as an ideal p-n junction with an added photogenerated current:

$$J = -J_{sc} + J_o(e^{qV/k_BT} - 1), \tag{3.4}$$

where J is the current density, J_o is the saturation current density, V is the applied voltage, k_B is Boltzmann's constant, and T is temperature.

V_{oc}, along with J_{sc}, is another figure of merit for solar cells, and is marked by the voltage when zero current flows. By solving for the case of zero current, one can find the formula for V_{oc} from the diode equation:

$$V_{oc} = \frac{k_B T}{q} ln\left(\frac{J_{sc}}{J_o} + 1\right), \tag{3.5}$$

where V_{oc} is the open circuit voltage. The current densities, J_{sc} and J_o, are normal-

ized by device area projected on a 2D plane. An extra consideration for nanowire solar cells is that the actual junction area of the device is much larger so J_o is much larger for nanowire devices, which according to the above equation, decreases V_{oc}. Fortunately, V_{oc} only depends logarithmically on the junction area.

Power density is defined by

$$P = JV. \tag{3.6}$$

The region of highest power density in a solar cell is marked in Figure 3.2.2 with a star. From the diagram, one can see that the rectangle defined by the point of maximum power (and the associated current J_m and voltage V_m points) is smaller than the rectangle defined by the J_{sc} and V_{oc}. The correction is accomodated by another figure of merit called the fill factor,

$$FF = \frac{J_m V_m}{J_{sc} V_{oc}}, \tag{3.7}$$

which describes "squareness" of the curve. The overall power efficiency η of the solar cell is described by the maximum power generated divided by the power incident on the solar cell P_s:

$$\eta = \frac{J_m V_m}{P_s}. \tag{3.8}$$

In terms of the solar cell's figures of merit, the efficiency can be described as

$$\eta = \frac{J_{sc} V_{oc} FF}{P_s}. \tag{3.9}$$

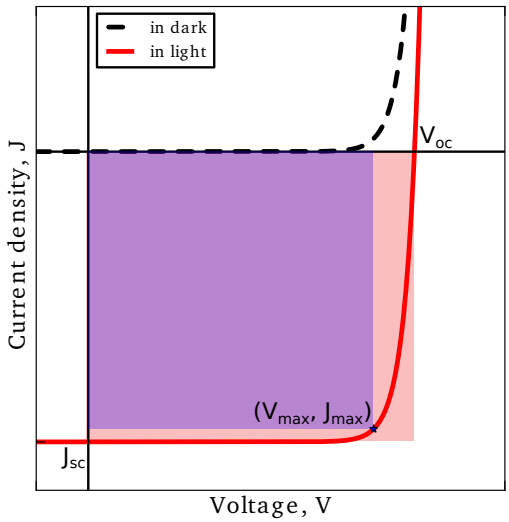

Figure 3.2.2: Model JV curve for ideal p-n junction solar cell. The star marks the point of maximum power.

3.3 Doping in Cu_2O

In this work, we control the structure of ZnO in the ZnO/Cu_2O solar cell, but the solar cell would not be possibe without the unique doping characteristics of Cu_2O. Most wide bandgap oxides are electrically insulating, but a few exhibit semiconducting properties, like ZnO. An even smaller group of wide bandgap oxides are naturally p-type semiconductors. Cu_2O is the model of a p-type wide bandgap semiconductor and, therefore, has been investigated thoroughly[165–170].

Cu_2O often exists in a non-stoichiometic state. The fact that the cation, Cu^+, is futher oxidizable to Cu^{2+} naturally leads to a cation-deficient state for the oxide. Copper vacancies, therefore, are abundant in this material in order to compensate

for the cation deficiency.

Raebiger et al. have studied the origins of the p-type nature and cation deficiency in Cu_2O through first principles calculations[165]. They showed that Cu_2O satisfies all of the conditions for making a p-type conductor: (i) a low formation energy for hole-producing defects, (ii) a small ionization energy for those defects to release the holes, and (iii) a high formation energy for compensating defects. They calculated an ionization energy of 0.28 eV above the valence band, which is in agreement with the hole trap experimentally found at 0.28 eV above the valence band. The potential compensating defects were oxygen vacancies and copper interstitials. Oxygen vacancies have a low formation energy but are not sufficiently stable as charged defects to fully compensate holes. Copper interstitials have a high formation energy and, therefore, do not exist in sufficient concentrations to compensate the copper vacancies. Thus, the copper vacancies lead to the p-type doping in Cu_2O.

3.4 Persistent photoconductivity in Cu_2O

Cu_2O also exhibits persistent photoconductivity (PPC). In typical semiconductors, the conductivity of the semiconductor switches to a state of increased conductivity when illuminated and returns to its more insulating state when the light is removed. Photoconductivity can be explained by the generation of excess carrier by the incident light. Since conductivity is proportional to the concentration of carriers, conductivity of the semiconductor increases. When the light is removed, the carriers recombine quickly and the conductivity returns to its dark state con-

ductivity.

When a semiconductor exhibits PPC, the switching response is much slower. When the semiconductor is illuminated, conductivity increases for some time before it plateaus. Similarly, when the light is removed, conductivity very slowly decays over a long period of time.

For many decades, the PPC in Cu_2O was explained by a simple electronic model where deep donors slowly trapped and re-emitted electrons but had a very small capture cross section for holes[171–173]. As the donor states were filled by photogenerated electrons, the conductivity slowly increased since they no longer compensated the copper vacancies. When light was removed and electrons were no longer photogenerated, the conductivity slowly decreased as trapped electrons were emitted and again began to compensate the copper vacancies.

Recently, it was shown through a disagreement between the time constants obtained through transient capacitance measurements and those calculated through PPC decay curves (resistivity vs time) that this simple model could not be correct [164]. A new model based on vacancy complexes was proposed[164].

In this model, the compensating donors are charged oxygen vacancies V_O^+ or V_O^{++}. The highly mobile copper vacancies V_{Cu}^-[174] associate with the charged oxygen vacancies through electrostatic interactions, forming a complex W^+ or W° (Figure 3.4.1). W^+ is the stable complex; W° simply dissociates again at room temperature. When the sample is illuminated, the W^+ captures a photogenerated electron, becoming W°. The W° complex dissociates, increasing the acceptor density. Since V_{Cu}^- is extremely mobile, it diffuses in the lattice after some time and

is redistributed away from the V_O^+ that had originally captured it. When the light is removed, V_O^+ cannot be restored to its original oxidation state by hole capture, because we assume that the V_O^+ energy level is below the Fermi level. This assumption is supported by the calculations by Raebier et al.[165] Instead, the V_{Cu}^- must diffuse back to a V_O^+ to make the W°, which can be stabilized to W^+ with hole capture. The PPC in Cu_2O can therefore be seen to be intimately connected to the highly mobile nature of the copper vacancies.

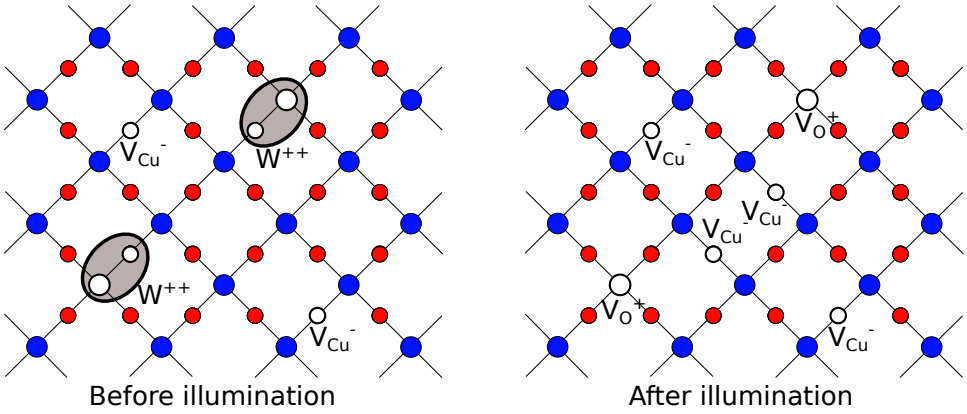

Figure 3.4.1: V_{Cu}^- and V_O^{++} bind to form a complex W^+ to prevent V_{Cu}^- from donating a hole to the valence band. Illumination breaks this complex apart and the V_{Cu}^- can migrate to contribute a hole to the valence band.

3.5 Experimental methods

3.5.1 Fabrication of planar and nanowire solar cells

FTO-coated glass (TEC 8 grade), purchased from Hartford Glass Co. Inc. (Hartford City, IN), acted as the substrate for the solar cell. Prior to any deposition, it was cleaned thoroughly with Alconox soap and water, rinsed with deionized water,

and ultrasonically cleaned with deionized water, acetone, and finally isopropanol. Cleaning the substrate was important in ensuring uniform growth of both ZnO and Cu_2O in subsequent steps. Organic material, such as fingerprints, could block the growth and cause dewetting of solution.

A seed layer was spin-coated onto the substrate with a solution of 0.7 M zinc acetate dihydrate and 0.7 M monoethanolamine in isopropanol at 3000 rpm for 45 seconds. Monoethanolamine was used to complex the zinc ions, increasing the solubility of zinc acetate in isopropanol, and to increase the viscosity of the solution. The coated substrate was immediately heated to 350°C on a hotplate for 1 hour. This annealing step ensures the oxidation of the existing zinc-organic coating into ZnO: the organic material in the film is burned off leaving behind nanocrystalline film of ZnO about 60 nm thick.

ZnO nanowires or ZnO thin films were then grown from the seeded substrate. For ZnO nanowires, the growth solution consisted of 0.2 g of zinc nitrate hexahydrate and 1.25 mL of 15 M ammonium hydroxide in 24 mL of deionized water, which was equivalent to 0.028 M $Zn(NO_3)_2{\cdot}6H_2O$ and 0.75 M NH_4OH. The substrate was suspended with the growth-side down in a Teflon vessel to prevent unwanted ZnO particle from settling onto the growth face. The vessel with the solution and substrate was heated to 90°C in an oven for typically 2 hours, resulting in nanowires that were about 2 μm tall. Longer growth times greatly increased the length of the nanowires. Shorter wires were much more difficult to obtain, because the growth rate at the beginning of growth is very high. For example, at 1.5 hours, no growth of ZnO nanowires was observed. After the designated growth

period, the sample was removed from the vessel and the rinsed throroughly with deionized water.

Continuous ZnO thin films were made with procedure that is almost identical to the procedure described for synthesizing ZnO nanowires. The growth solution for ZnO thin films consisted of 0.2 g zinc nitrate hexahydrate, 1.25 mL of 15 M ammonium hydroxide, and 0.05 g of sodium citrate tribasic dihydrate in 24 mL of deionized water, equivalent to 0.028 M $Zn(NO_3)_2{\cdot}6H_2O$, 0.75 M NH_4OH, and 0.008 M $HOC(COONa)(CH_2COONa)_2 \cdot 2H_2O$. The addition of sodium citrate inhibited the normal c-axis growth rate of ZnO. As growth proceeded, neighboring ZnO crystals merged together, forming a coalesced thin film. These films were grown similarly at 90°C, but the growth times were 4 hours or more. The typical thicknesses of these ZnO thin films were 3-4 μm.

To increase the conductivity, ZnO was annealed and exposed to UV light, which improved the quality and uniformity of the electrodeposited Cu_2O. ZnO nanowires or thin films were annealed at 250°C for 30 minutes. The annealing step improved the conductivity of ZnO due to liberation of hydrogen in the remaining $Zn(OH)_2$ [83], which remains to some extent in all aqueously derived ZnO due to incomplete conversion to ZnO[57, 82]. Hydrogen is known to be an n-type dopant in ZnO, and the annealing step has been observed to push the carrier concentration to 10^{18} cm^{-3}[83]. The UV light exposure further increased the conductivity of the ZnO by surface modification[86] as described in Chapter 2.

Immediately following the UV light treatment, a Cu_2O film was electrodeposited onto the ZnO[135, 175–179]. The aqueous solution for Cu_2O electrodeposition

was made using 0.4 M $CuSO_4 \cdot 5H_2O$ and 3 M lactic acid, where pH was adjusted to 12 using 4 M NaOH solution. The sample was suspended in this solution where deposition occurred cathodically at 0.45 V with respect to a standard calomel electrode at 60°C[175]. The sample was thoroughly washed with deionized water and blown dry with nitrogen. Gold contact pads were deposited using an electron beam evaporator through a shadow mask with areas of 0.2 cm^2 each.

3.5.2 Characterization of solar cells

Current density-voltage (J-V) measurements were taken with a Keithley 2636A by sweeping voltage from -1V to 1V. Current-time measurements were also taken with the Keithley 2636A by applying a 1V bias and measuring current over time under different illumination conditions. For measurements under illumination, a 300 W mercury xenon arc lamp with a AM 1.5 global filter was used at an illumination intensity of 100 mW/cm^2. EQE measurements were completed using a Newport Merlin digital lock-in radiometry system with the 300 W mercury xenon arc lamp focused on a Newport Cornerstone 260 monochromator with appropriate bandpass filters and chopper. A calibrated UV Si photodetector (Newport) was used to measure the intensity of the incident light for EQE measurements. The EQE scan rate was 1 nm/sec.

3.6 Cross-sectional structure of nanowire and planar solar cells

Cross-sectional scanning electron microscopy confirmed the architectures of the planar and nanowire ZnO/Cu_2O solar cells (Figure 3.6.1). The interface of the planar solar cell was slightly rough since the ZnO was polycrystalline and each columnar crystal was oriented slightly differently with respect to the substrate (Figure 3.6.1a). In the nanowire solar cell, nanowires grew initially in random directions, but the fast c-axis growth eliminated nanowires that did not grow vertically (Figure 3.6.1b). Therefore, the aggregate structure was much more chaotic near the substrate compared to the tops of the nanowires, where they were nearly completely vertically oriented. The cross-sectional view also showed that the ZnO nanowires were completely encased in the Cu_2O matrix (Figure 3.6.2). Due to the violent nature of the cleaving process, which was necessary to create the cross-section of the sample, some ZnO nanowires were pulled out. Impressions of the ZnO nanowires indicated intimate contact with the Cu_2O and complete filling of the space between nanowires with the electrodeposited Cu_2O.

3.7 Nanowire geometry increases carrier collection

We confirmed through J-V measurements and EQE measurements that carrier collection was improved through the incorporation of ZnO nanowires. In the comparison of the J-V plots between solar cells made with planar and nanowire mor-

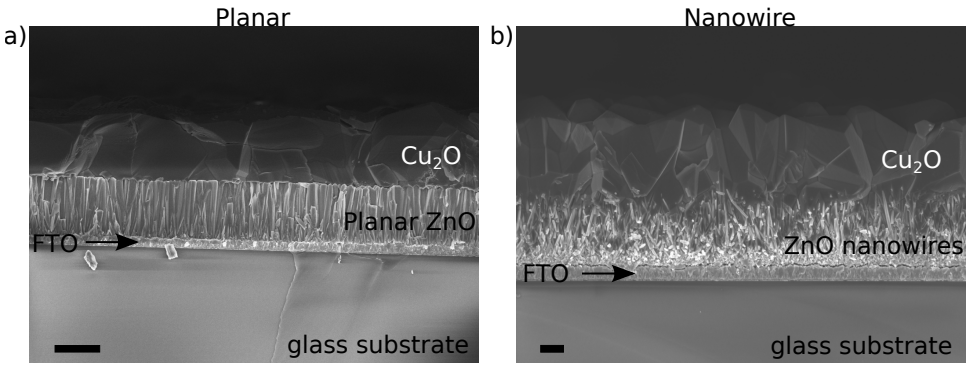

Figure 3.6.1: Cross-sectional SEM micrographs compare the microstructure of (a) the planar ZnO/Cu_2O solar cell and (b) the nanowire ZnO/Cu_2O solar cell. Scale bars = 3 μm and 1 μm, respectively.

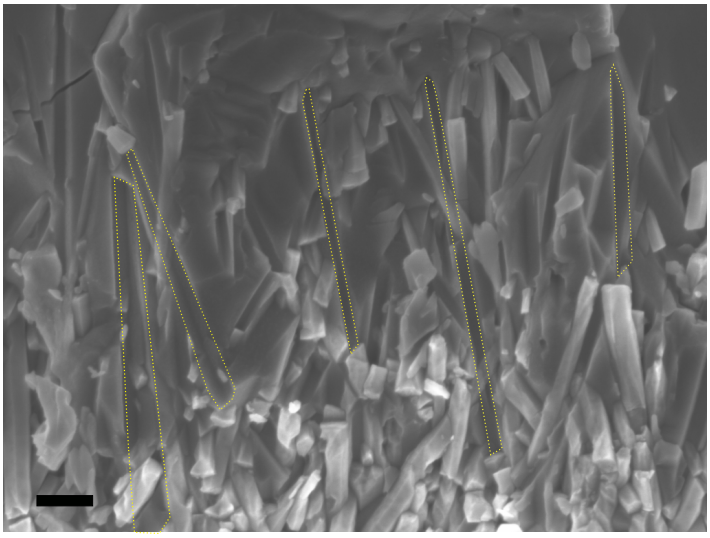

Figure 3.6.2: High magnification, cross-sectional, SEM micrograph of a nanowire ZnO/Cu_2O solar cell, showing the impression of ZnO nanowires in the Cu_2O matrix after pull out. Several of the many nanowire impressions have been highlighted. Scale bar = 300 nm.

phology (Figure 3.7.1), short circuit current J_{sc} was markedly increased in solar cells with nanowire architecture. However, the open circuit voltage V_{oc} roughly stayed the same or even decreased with the incorporation of nanowires. The mechanism for the decrease in V_{oc} for nanowire solar cells was explained in the "Ideal Solar Cell" section.

EQE measurements confirmed that the increased J_{sc} was due to the increased collection efficiency for carrier generated deep in the material by long wavelength photons. A comparison of EQE between the planar and the nanowire solar cells (Figure 3.7.2d) showed the difference in carrier collection for longer wavelength photons. Figure 3.7.2a,b show how the planar and the nanowire structure collect carriers differently, which affects the resulting EQE. For the planar solar cell, the drift-diffusion length (L_{dd}) must be greater than the absorption length (a_L) in Cu_2O for efficient collection. EQE measurements of the planar solar cells followed this general explanation. Short wavelength photons with energies greater than the bandgap of ZnO were all fully absorbed in the ZnO and did not contribute to photocurrent in the Cu_2O. These carriers were not generated close enough to the interface of ZnO and Cu_2O to be separated by the internal electric field. For photons in the 375 - 500 nm range, the absorption length[130] is less than the minority carrier drift-diffusion length in Cu_2O, which has been measured to be 200 nm[161]. Figure 3.7.2c,d shows how the carriers generated by these photons have a high EQE and how the EQE saturates in this wavelength range. For longer wavelength photons, the absorption length is longer than the minority carrier drift-diffusion length, and so the EQE decreased to nearly zero in these wavelength ranges, even

for photons with energies above the bandgap of Cu_2O. In contrast, the EQE measurements for the nanowire solar cell did not show the same limitations of carrier collection as a function of absorption length (Figure 3.7.2d). EQE was increased for long wavelength photons in nanowire solar cells. Even though the absorption length was much larger in the 500 - 650 nm range, EQE remained high in this region. Thus, we showed that the incorporation of nanowires in the solar cell increased the collection of carriers generated by photons with an absorption length longer than the L_{dd}.

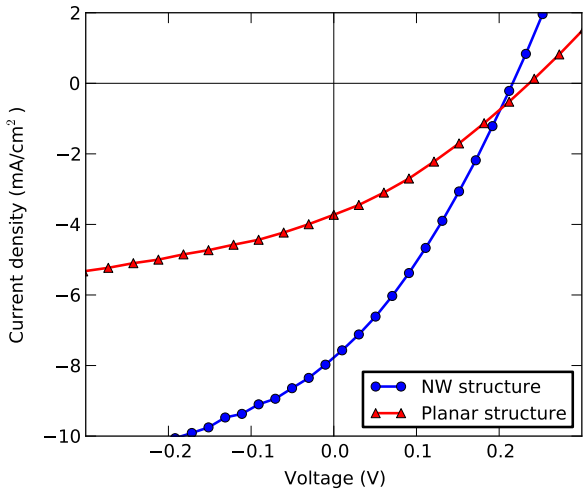

Figure 3.7.1: Current density - voltage comparison between nanowire and planar ZnO/Cu_2O solar cell geometries.

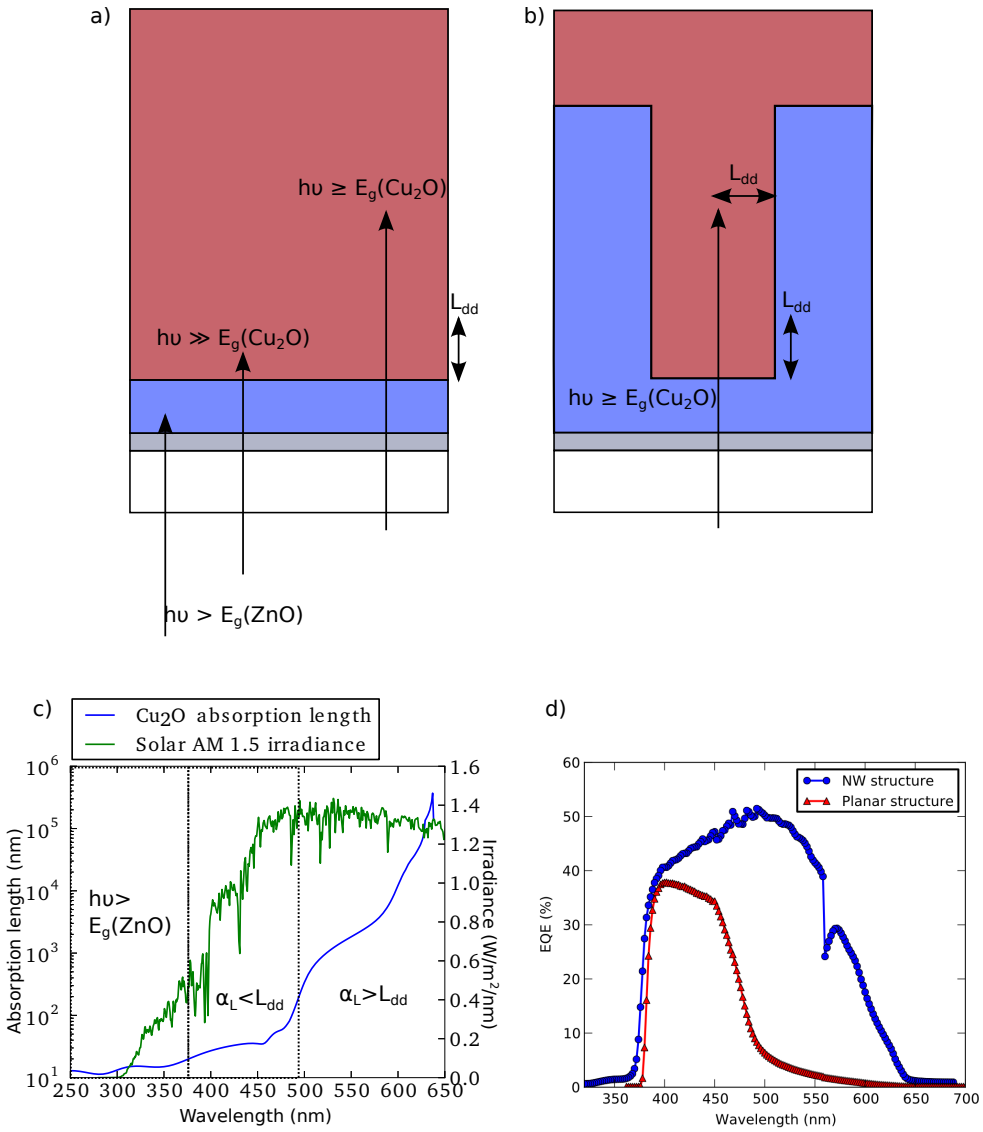

Figure 3.7.2: The conflict between minority carrier drift-diffusion length (L_{dd}) and photon absorption length (α_L) in comparing EQE for planar and nanowire solar cells. a) In a planar solar cell, carriers are not collected, where $\alpha_L > L_{dd}$, since path of the photon and the minority carrier are in the same direction. b) In a nanowire solar cell, carriers can be collected, where $\alpha_L > L_{dd}$, since path of the photon and the minority carrier are in orthogonal directions. c) Absorption length[130] in Cu_2O and AM 1.5 solar irradiance. Critical wavelength ranges are delineated. d) EQE of planar vs. nanowire solar cell. EQE for nanowire solar cell is increased for wavelengths where $\alpha_L > L_{dd}$.

3.8 Effects of persistent photoconductivity

During J-V and EQE testing of many devices, it was noted that the performance of the devices depended on the history of the device. For example, the typical order of testing the J-V characteristics of these devices after being made was to test all of the devices in the dark, then illuminate and test in AM 1.5, 1 Sun illumination, then test again in the dark. The two J-V plots in the dark were always markedly different (Figure 3.8.1). Prior to illumination, rectification was extremely poor, if there was rectification at all. After illumination, the devices that generated photocurrent all displayed much better rectification.

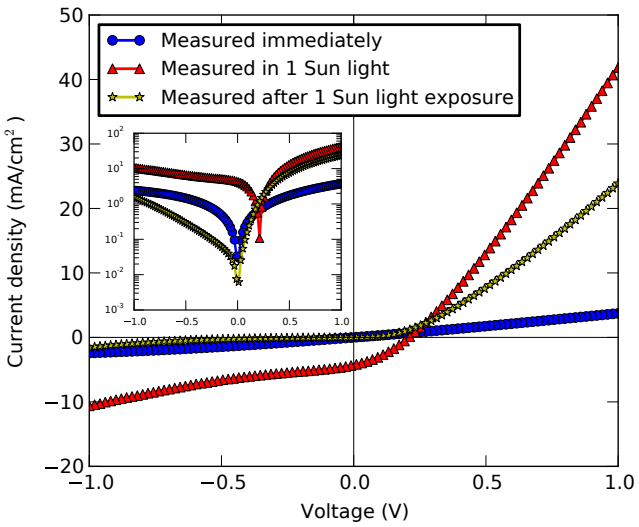

Figure 3.8.1: J-V plot of nanowire ZnO/Cu_2O solar cell. Prior light exposure to the solar cell made the diode more rectifying in the dark. Inset shows a semilog plot of the J-V plot, showing the different degrees of rectification.

The cause of this history-dependent behavior was traced back to the persistent

photoconductivity in Cu_2O. While ZnO has also been reported to display persistent photoconductivity (PPC), the mechanism has always been traced back to surface-related phenomena[60, 87]. In the case of ZnO/Cu_2O solar cells, the ZnO interfaces were buried. With buried interfaces, the PPC effects have been shown to decrease dramatically in ZnO[180]. On the other hand, PPC effect in Cu_2O were due to long-lived trap states that reside throughout the volume of the material as discussed earlier in this chapter[164, 171–173].

To further study the persistent photoconductivity, we monitored the EQE over time. The solar cells were initially illuminated with AM 1.5 light for 5 minutes to set the solar cell in the photoconductive state. Unlike other semiconductors that do not display PPC, Cu_2O remained in the photoconductive state after illumination ceased. EQE measurements were then taken periodically in the dark. During the EQE measurement, a spectrum of monochromatic light must shine on the sample. However, the intensity of the monochromatic light, that is a part of the EQE measurement, is low compared to the AM 1.5 illumination. Slowly, the photoconductive Cu_2O reverted to its more insulating state. As carrier density decreased, the series resistance in the solar cell decreased, accompanied by a general decrease in EQE (Figure 3.8.2). Since the decay in EQE was related to PPC, a bulk property, the decay in EQE was not selective to any particular wavelength, i.e., EQE decayed for all wavelengths.

Another method by which PPC was observed was through current-time measurements. Here, the solar cell was pre-illuminated for 5 minutes under 1V bias. The current decay was monitored after the illumination ceased (Figure 3.8.3). The

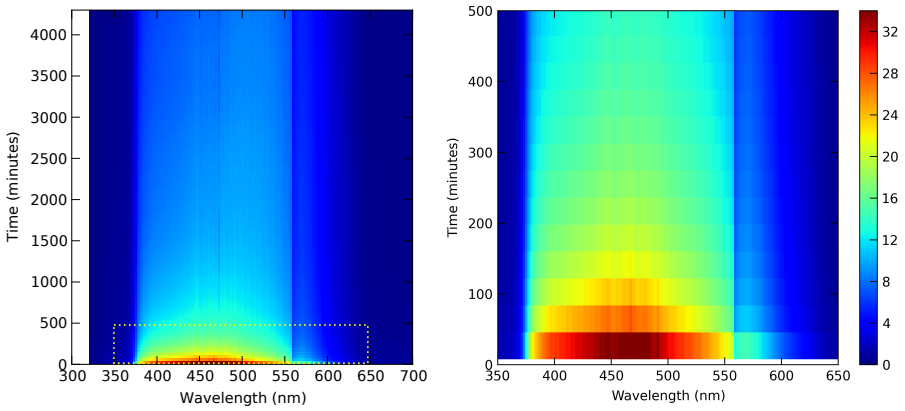

Figure 3.8.2: EQE decay over time of ZnO/Cu_2O nanowire solar cell. (b) shows the magnified version of the highlighted box in (a). EQE intensity in units of percent.

decay in the current was faster than the EQE decay, because the device remained in the dark during the measurement period for current. However, even after 5 hours, the current was still decaying to the insulating state, the state of the device before any illumination. The EQE measurement, on the other hand, required low intensity, monochromatic light to be incident on the device to measure photocurrent, which decreased the rate of decay. Both measurement techniques showed that the devices displayed characteristics of PPC.

An important caveat to PPC decay is that charging the device to be in the fully photoconductive state also takes time[172, 173]. Measurements of current vs. time under a 2V bias and illumination showed that the device took more than 1 hour to become fully charged (Figure 3.8.4).

There are better methods of measuring PPC, such as Hall measurements[164] and resistivity of a thin film of Cu_2O with semi-transparent Ohmic contacts[172].

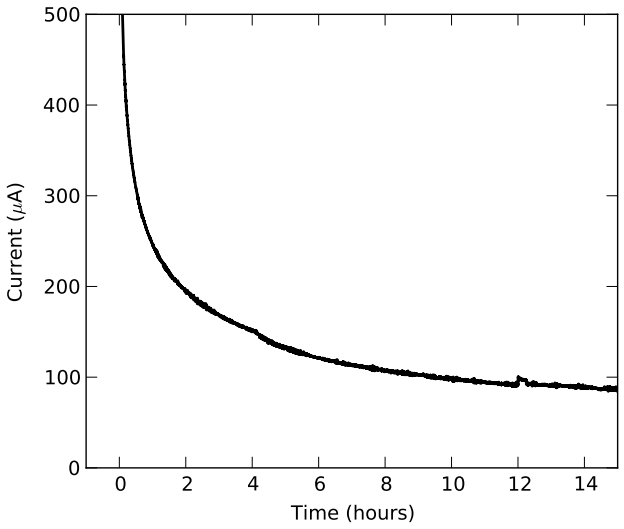

Figure 3.8.3: The decay of measured current on ZnO/Cu_2O with the application of 1V bias. The slow decay of current is observed after the initial illumination was turned off.

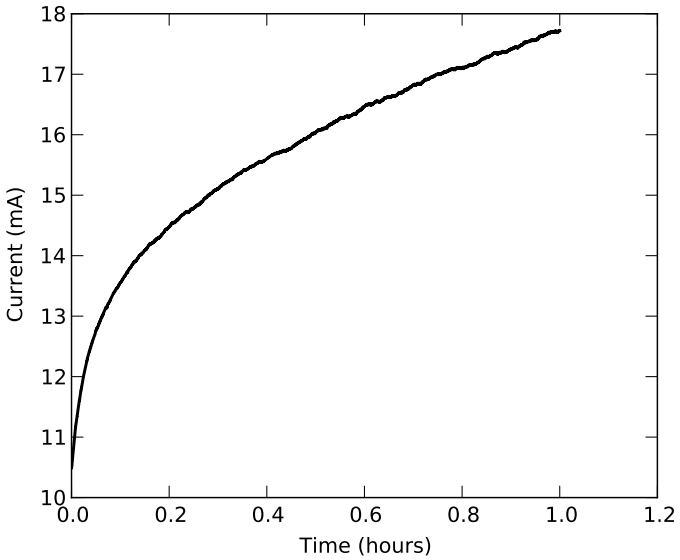

Figure 3.8.4: The measured current with the application of 2V bias slowly increased in the ZnO/Cu_2O solar cell under illumination.

However, these methods were not possible with these electrodeposited samples. Hall measurements required the Cu_2O to be separated from the conducting substrate. Although there were reports of separating the thin film from the conducting substrate though thermal or mechanical shock[181, 182], we were unable to separate the substrate and thin film and process it without inducing a network of cracks in the Cu_2O thin film (Figure 3.8.5). The cracking rendered the thin film too insulating to measure through Hall measurements. Measuring resistivity of thin films of Cu_2O was also difficult due to the insulating nature of electrodeposited Cu_2O. Prior reports measuring resistivity through semi-transparent Ohmic contacts used single crystal Cu_2O[172]. Electrodeposited Cu_2O was polycrystalline and much more insulating[182].

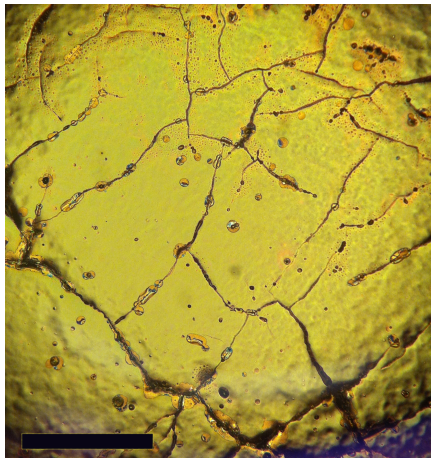

Figure 3.8.5: Picture of the cracks that formed after processing in electrodeposited Cu_2O films that had been separated from the substrate. Scale bar = 1mm.

3.9 EQE shifts due to dopant migration

Given these short-term changes in the electrical characteristics of the solar cell due to PPC, a longer time frame was studied with EQE measurements. These measurements started with the solar cell illuminated for 30 minutes before the first EQE measurement took place. During the actual EQE measurement, the device was only exposed to the monochromatic light that was used to measure EQE. Each scan took about 8 minutes. For the 30 minutes between each scan, the devices were illuminated with light. Both planar and nanowire solar cells were measured. The results show that over long periods of time, the EQE decreases as the devices age (Figure 3.9.1). Another striking feature was the leftward shift in the color bands during the first 5 hours of the measurement. EQE plots are typically characterized by a plateau, where the EQE is highest due to the wavelength of light being long enough to pass through the window layer (ZnO in our case) but short enough to be absorbed by the absorber layer (Cu_2O). The shift in the color bands indicated that this plateau was shifting toward higher energy regions. The shift was more markedly seen in the EQE for flat solar cells. The major difference between the two types of devices was that, for the nanowire solar cells, the shift was accompanied by a rightward shift at longer wavelength. This shift continued well past the first 5 hours. The end result of these two effects is that for nanowire solar cells the total plateau becomes wider as the solar cell ages.

In Figure 3.9.2, we plotted each EQE spectrum as a change from the first EQE spectrum. The changes in the EQE spectrum are easier to see. For the planar

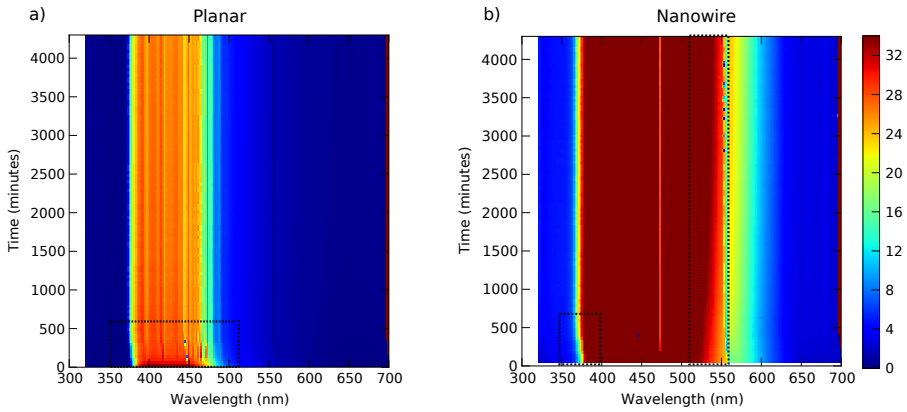

Figure 3.9.1: EQE shifts over time while under illumination for a) planar ZnO/Cu_2O solar cell and b) nanowire ZnO/Cu_2O solar cell. Colormap is in units of percent EQE. Dashed rectangles (1 in a and 2 in b) highlight the areas of changing EQE.

solar cell (Figure 3.9.2a), EQE increases just beyond the bandgap of ZnO. For wavelengths beyond this narrow wavelength range of increasing EQE, the EQE decreases substantially over time. Figure 3.9.2b shows the changes in EQE for the nanowire solar cell. Similar to the planar solar cell, the EQE increases in the region just below the ZnO bandgap and decreases in the region up to 500 nm. Unlike the planar solar cell, the EQE increases for much longer wavelengths in the region of 500 - 600 nm. The reasons for these changes will be explained in the following sections.

As previously discussed in the PPC section, the EQE evolution over time in the dark was different from the EQE evolution in the light. Figure 3.8.2 showed the EQE evolution over time in the dark after the initial illumination to light was turned off. As these solar cells aged in the dark, the EQE measurements did not indicate any shifting of the color bands. The boundaries of the plateau remained at

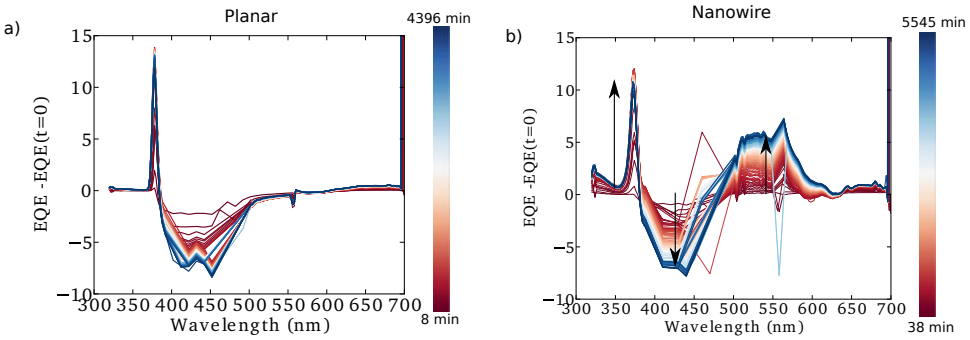

Figure 3.9.2: Change in EQE under illumination for a) planar ZnO/Cu_2O solar cell and b) nanowire ZnO/Cu_2O solar cell.

the same wavelengths as in the beginning of the aging process (Figure 3.9.3).

3.9.1 The idea

A typical assumption in semiconductor p-n junctions is that the ionized donors and acceptors, residing in the depletion region, are immobile even though the electrons or holes that they donate to the lattice are mobile. The mobile holes in the p-type region near the interface diffuse across the junction to the n-type region, and similarly, the mobile electrons from the n-type region near the interface diffuse across the junction to the p-type region. As the diffusion is occurring, the ionized acceptors and donors are assumed to not move and therefore constitute an electric field, establishing a potential difference to prevent more mobile holes and electrons from diffusing across the electric field.

The immovable nature of these ionized acceptors and donors appears not to hold true for the ZnO/Cu_2O solar cells studied here. Since the typical p-n junction in often modelled in silicon, this assumption is usually a very good approx-

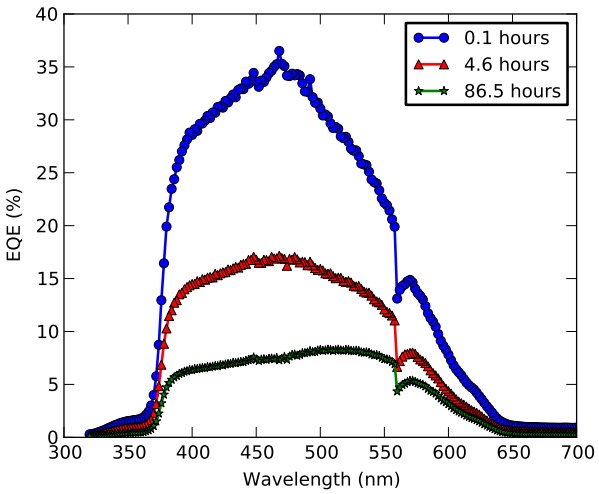

Figure 3.9.3: Selected EQE plots of ZnO/Cu_2O nanowire solar cell after ceasing initial illumination. EQE was measured after the specified time. EQE decayed very slowly over time after initial illumination was turned off.

imation of reality. The diffusion coefficients for typical silicon dopants residing in the silicon lattice are exceedingly small at room temperature[183]. However, the same is not true for other materials like Cu_2O and ZnO. The diffusion of free electrons and holes is still much faster than the diffusion of ionized donors and acceptors. Therefore, an electric field still forms due to the equilibration of holes and electrons. The electric field that is set up by these ionized donors and acceptors, though, now begins to act on the slightly mobile ionized donors and acceptors. In Cu_2O, the ionized acceptors are copper vacancies. In ZnO, the ionized donors are hydrogen atoms. The motion of these ionized acceptors and donors can cause changes to the electric potential profile of the device.

The movement of native point defects by an internal electric field has some precedence. Aluminum and gallium vacancies in AlGaN high electron mobility

transistors have been shown to move in regions of very high electric fields (10 MV/cm)[184]. In addition, native defects in ZnO have also previously been shown to massively redistribute near the surface, resulting in unexpected Schottky barrier heights[185, 186].

In solar cells, changes in the width of the depletion region and the electric field will cause changes in how effectively the charges generated at different positions in the device will be collected. Carriers are collected through a combination of drift and diffusion. Diffusion lengths are only a function of concentration gradient and quality of the material. We normally assume for Si p-n junction solar cells that the diffusion length limits carrier collection. Once the minority carrier crosses into the depletion region, we assume that the electric field is sufficient to sweep all carriers away. So, a larger depletion region will increase the collection efficiency of charge carriers generated deeper in the solar cell. However, in a case for very lightly doped materials, the electric field in the depletion region can be insufficient to sweep away minority carriers before recombination. A drift length can be defined:

$$L_{drift} = \mu \vec{E} \tau, \tag{3.10}$$

where μ is the mobility of the carrier, $\vec{E}$ is the electric field, and τ is the lifetime of the carrier. Therefore, a combination of drift and diffusion lengths L_{dd} is the more realistic limit to the length that minority carriers can travel before recombination. The L_{dd} and therefore the probability of carrier collection also a function of the electric field.

Like the drift-diffusion equations that govern the transport behavior of free elec-

trons and holes, drift-diffusion equations can be applied to the mobile, ionized acceptors and donors:

$$\frac{\partial c}{\partial t} = \nabla \cdot (D\nabla c) - \nabla \cdot (c\mu\vec{E}) + R, \tag{3.11}$$

where c is the concentration of the ionized acceptor or donor, t is time, D is the diffusion coefficient of the ionized species, μ is the mobility of the ionized species, $\vec{E}$ is the electric field and R is the rate of defect compensation. The drift component is found to dominate the motion of these ionized species initially. The diffusion component remains negligible until the driving force for diffusion, the concentration gradient, becomes appreciable due to the redistribution of the ionized species by the electric field.

The distance that an ionized defect, such as an ionized copper vacancy, can move in the depletion region in a specified period of time can be calculated. The velocity of the ionized defects is dependent on the mobility of the defects, μ and the electric field, E:

$$v = \mu\vec{E}, \tag{3.12}$$

where μ can be found from the diffusion coefficient from the Einstein relation:

$$\mu = \frac{Dq}{k_B T}, \tag{3.13}$$

where k_B is Boltzmann's constant. The electric field profile can be calculated from the Poisson equation if the charge profile is known. Assuming an initially constant

charge profile within the depletion region,

$$v = \mu\vec{E} = \mu\frac{\rho x}{\varepsilon_r\varepsilon_o}, \tag{3.14}$$

where ρ is the charge density, x is position with x=0 at the edge of the depletion region, and ε_r is the relative dielectric constant of the material and ε_o is the permittivity of free space. By making the naive assumption that the electric field does not change as the defects move, an assumption that is later removed, we can find how far a defect moves within a period of time:

$$v = \frac{dx}{dt} = \frac{\mu\rho}{\varepsilon_r\varepsilon_o}x \tag{3.15}$$

$$\int_{x_o}^{x}\frac{dx}{x} = \int_{t_o}^{t}\frac{\mu\rho}{\varepsilon_r\varepsilon_o}dt \tag{3.16}$$

$$\Delta x = x - x_o = x_o(exp[\frac{\mu\rho}{\varepsilon_r\varepsilon_o}(t - t_o)] - 1) \tag{3.17}$$

Since only the ionized defects move under the influence of the electric field, a region consisting of fewer defects is created near the edge of the depletion region. This region is called the highly compensated region by Mittiga et al.[164]

In the Cu_2O/ZnO system, the copper vacancies and hydrogen interstitials drift towards each other to the interface. Two types of boundary conditions are possible at the interface of ZnO and Cu_2O. In the first case, the hydrogen from the ZnO and copper vacancies from the Cu_2O are allowed to interact with each other. With

the confluence of the two ionized species, the mobile donor and acceptors compensate each other at the interface and the concentrations of both species are zero at the boundary. As donors and acceptors are removed from the system near the interface, the depletion region increases but the electric field decreases. In the second case, the flux of hydrogen and copper vacancies across the boundary is zero. Copper vacancies in the depletion region accumulate in a thin layer near the interface, draining the rest of the depletion region of copper vacancies. In the thin layer of copper vacancy accumulation near the interface, the electric field can be greatly increased. In the region of the depletion region that has been drained of copper vacancies, the electric field becomes much smaller. Overall, the depletion region is also increased. Regardless of which boundary condition is present, the PPC effects of Cu_2O also result in more ionized acceptors with some exposure to light. Therefore, the effects of mobile, ionized, copper vacancies in Cu_2O are much more evident under the exposure of light.

3.9.2 Mutual compensation of migrating, charged defects

Based on literature values of ZnO and Cu_2O prepared by similar methods, carrier densities of 10^{18} cm^{-1} and 10^{14} were used, respectively[35, 182]. Figure 3.9.4 shows the doping density and the calculated charge profile, electric field profile, and band diagram for a device where the doping density is constant in each material. Because the ZnO is so heavily doped compared to the Cu_2O, the depletion region in the ZnO is extremely thin and confined very close to the interface. The ionized hydrogen donors in the ZnO can therefore easily diffuse or drift across

the interface into the Cu_2O and compensate the acceptors that also cluster at the interface[187]. In fact, hydrogen has been used by others to passivate the surface and grain boundaries of Cu_2O[188, 189]. The compensation of the copper vacancies at the interface by hydrogen would imply that a build-up of copper vacancies would not occur at the interface. Rather, the concentration of copper vacancies would be fixed at zero at the interface.

As explained in the previous section, ionized copper vacancies move under the influence of the internal electric field. If the copper vacancies are compensated by the hydrogen in the ZnO at the interface, then accumulation of the copper vacancies will not occur. A cartoon version of this process can be seen in Figure 3.9.5. In this cartoon version, the depletion approximation is used, making the distribution of charged vacancies uniform within the depletion width. We also assumed that the electric field that was applied to the ionized copper vacancies was uniform, resulting in a simple translation in the ionized copper vacancy distribution. As seen in the middle panel of Figure 3.9.5, the movement of the charged vacancies results in a region without any copper vacancies near the edge of the depletion region. In order to drop the same built-in voltage, defined by the difference in work function of the Cu_2O and the ZnO and proportional to the area under the electric field profile, the electric field must be extended beyond the original depletion region. Thus, within these approximations and assumptions, the depletion region is extended when ionized copper vacancies move toward the ZnO/Cu_2O interface.

Similarly, when the depletion approximation is not used and diffusion is allowed

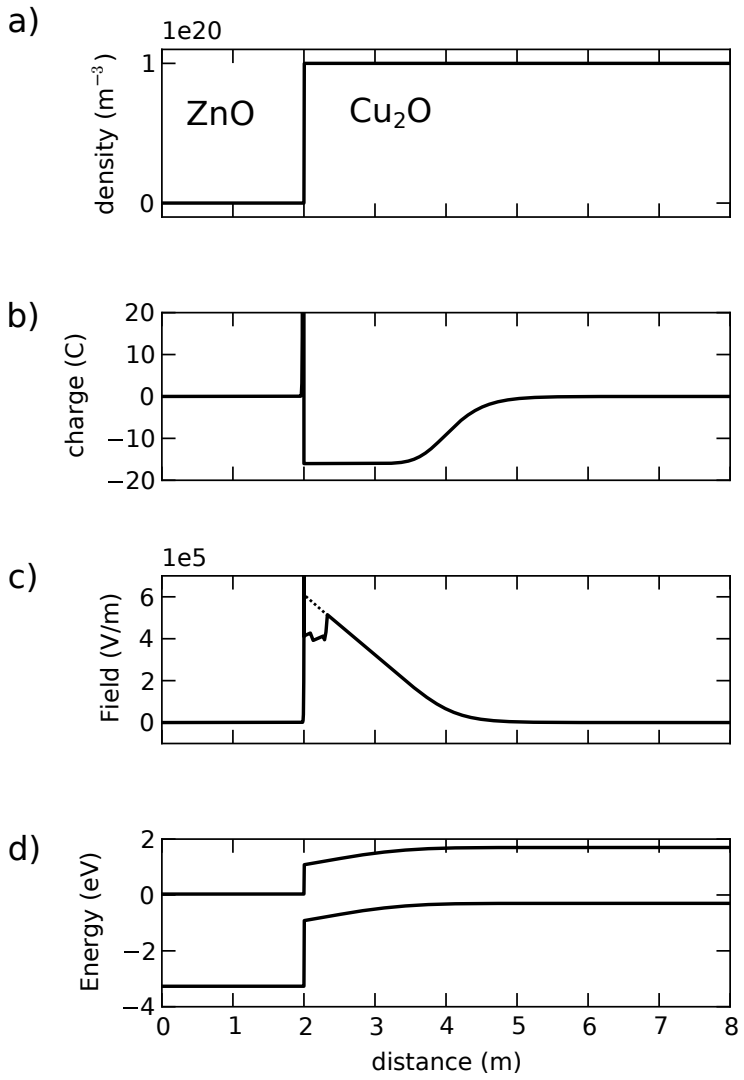

Figure 3.9.4: Initial condition of the simulated ZnO/Cu_2O solar cell. The interface between ZnO and Cu_2O is at 2 μm. The ZnO is on the left side of the interface and the Cu_2O is on the right. a)Doping density of the Cu_2O. b) Charge density. c) Electric field. d) Energy band diagram. Note: The solution to the electric field profile is numerically unstable very close the interface. The dashed line depicts the expected electric field profile near the interface in the Cu_2O. The charge density and the electric field of the ZnO has been cropped and is not fully depicted.

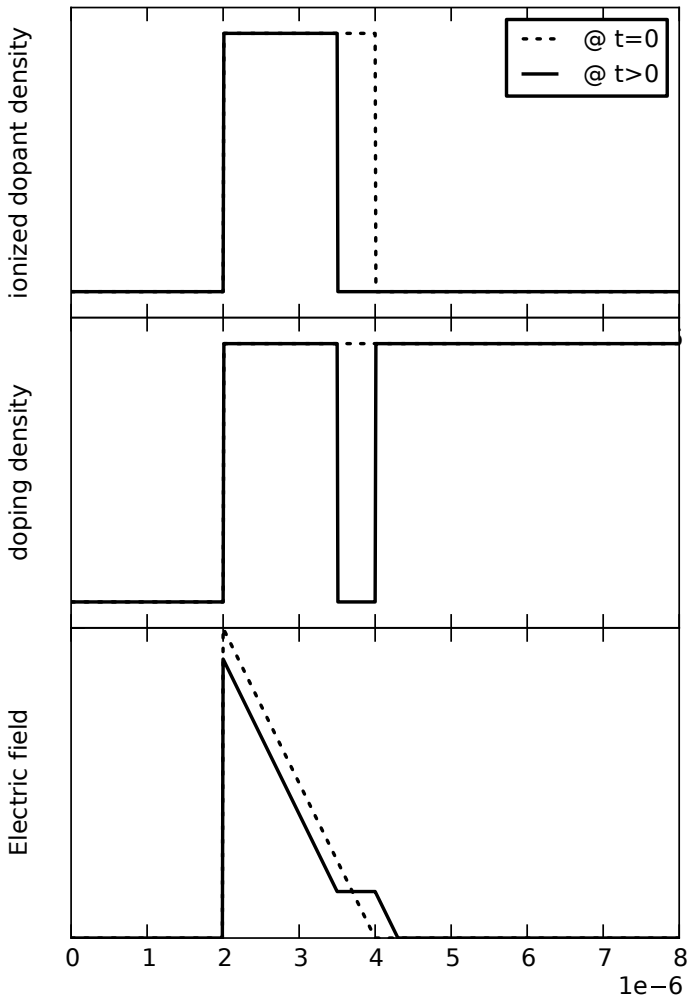

Figure 3.9.5: Schematic of how ionized copper vacancies move under the electric field. The ZnO/Cu_2O interface resides at $x = 2\mu m$. Top panel: plot showing the movement of the ionized copper vacancies assuming a uniform electric field and the depletion approximation. The ionized copper vacancies have moved uniformly to the left. Middle panel: plot showing the change in the distribution of the ionized copper vacancies within the Cu_2O. Bottom panel: plot showing the change in the electric field and the depletion width due to the changing distribution of the copper vacancies.

the depletion, a region forms near the edge of the depletion region with fewer copper vacancies, increasing the extent of the depletion region. Eventually, this region with fewer copper vacancies expands to encompass the entire depletion region. The depletion region as seen in Figure 3.9.6 expands well beyond the original depletion region after long time periods. The longer depletion region can increase the collection efficiency for carriers generated farther away from the ZnO/Cu_2O interface.

3.9.3 Accumulation of charge at the interface

The opposite case is where there is no compensation of the defects at the interface, and the copper vacancies are allowed to accumulate at the interface. Similar to the previous case, a region that is depleted of ionized copper vacancies is created at the edge of the original depletion region. The ionized copper defects at the edge of the original depletion region encounter sufficient electric field to move them toward the interface. The diffusion of the nearby copper vacancies is still too slow to fill in the region. However, unlike the previous case, a region with a high concentration of copper vacancies forms near the interface. Because there is back diffusion, the high concentration region will have a finite thickness. (Unfortunately, the motion and accumulation of ionized copper vacancies could not be simulated due to instabilities brought by the abruptness of the interface and the highly non-linear nature of the governing equations[190].)

We simulated a cartoon depiction of distribution of ionized copper vacancies after some period of time (Figure 3.9.7). Similar to the previous case, we assumed

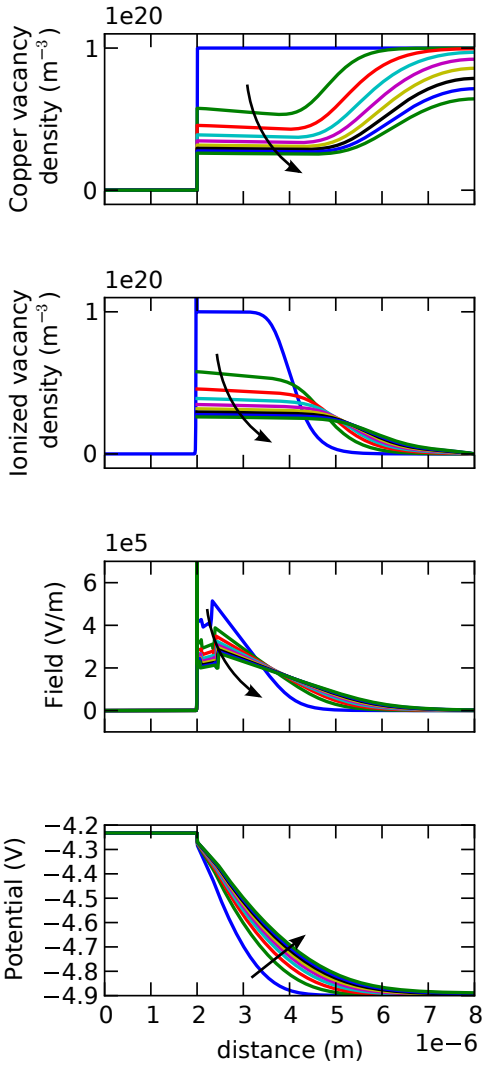

Figure 3.9.6: Simulation shows the resulting (a) copper vacancy density, (b) ionized copper density, (c) electric field, and (d) potential profiles with the assumption that all copper vacancies at the ZnO/Cu_2O interface will be compensated. Each line represents the state of the device progressing in time with an interval of 4.3 hours. The arrows show the trends as time proceeds.

that the electric field that drove the ionized copper vacancies was constant in the depletion region and that diffusion of the copper vacancies was negligible in the driving of the copper vacancies. The number of ionized copper vacancies is conserved and the flux of copper vacancies across the ZnO/Cu_2O interface is zero. The depletion region in the Cu_2O is slightly more than 2 μm wide, so the ionized copper vacancies residing in the final 1.5 μm of the depletion region were moved to a region 500 nm wide adjacent to the interface. Since the number of ionized copper vacancies was conserved, the concentration added to the 500 nm region was $1x10^{20}m^{-3}$ ▪$1.5x10^{-6}m/500x10^{-9}m = 3x10^{20}m^{-3}$.

While the band diagram was not affected very much by the dramatic redistribution of the ionized copper vacancies, the electric field profile changed dramatically. The maximum of the electric field within the Cu_2O region increased in order to satisfy the V_{bi} requirement set by the difference in ZnO and Cu_2O work functions. The accumulation of charge at the interface makes the electric field decrease much faster near the interface. Therefore, to conserve the area under the electric field profile (which equals V_{bi}), the maximum electric field at the interface must increase and the depletion region must also increase. With passing time, (1) the accumulation of the ionized copper vacancies increases, (2) the electric field near the interface increases, (3) the band bending near the interface increases, (4) the depletion width increases, and (5) the field within the depletion width that is not in the accumulation layer decreases. Eventually, the voltage on the Cu_2O side will effectively all be dropped in the thin accumulation layer, and the field outside of the accumulation layer will be zero.

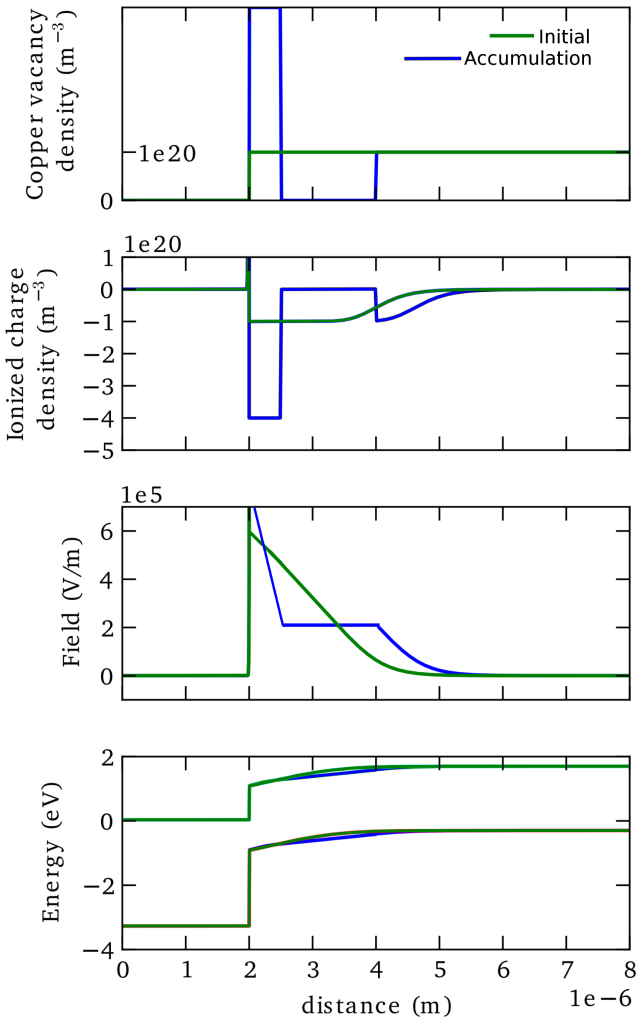

Figure 3.9.7: Effect of the accumulation of ionized copper vacancies near the interface due to drift. (a) Copper vacancy density, (b) ionized copper density, (c) electric field, and (d) energy band diagram with the assumption that all copper vacancies at the ZnO/Cu_2O interface will accumulate.

While we have presented two extreme cases for movement of ionized copper vacancies near the ZnO/Cu_2O junction, the most likely case is a combination of both. In the following sections, we will discuss how the experimental data show evidence of both accumulation and compensation of ionized copper vacancies at the interface.

3.9.4 Blue shift in the EQE at short times

In typical silicon pn junction solar cells, it is assumed that all minority carriers generated within the depletion width of the junction and the a minority carrier diffusion length away form the junction for both p- and n-type regions are collected. The electric field within the depletion region is assumed to be strong enough that all minority carriers that reach this region are instantaneously swept away. The limiting factor for carrier collection is considered the diffusion of the minority carriers. Carriers within a minority carrier diffusion length of the depletion region are considered to be collected, because they are considered to have enough mobility and time to meander to the junction before they recombine.

Recently, it was shown by Musselman et al.[146, 161] that in the ZnO/Cu_2O system, we have to consider both the drift and diffusion length of minority carriers in the Cu_2O. They calculated using the drift diffusion model that the drift length L_{drift} was 110 nm and the diffusion length L_{diff} was 100 nm in electrodeposited Cu_2O[161]. Although these values are only estimates, the fact that the drift length is smaller than the depletion width (2.7μm in their case) implies that recombination within the depletion width is an important issue[161].

The drift length is proportional to the electric field and the minority carrier lifetime. The drift length can be calculated by the following equation:

$$L_{drift} = \mu \vec{E} \tau, \tag{3.18}$$

where μ is the minority carrier mobility, $\vec{E}$ is the electric field, τ is the minority carrier lifetime. Higher electric field values can increase the drift length and thereby increase the probability of carrier collection from the region with the higher magnitude of the electric field. We believe that the blue shift of the EQE in the first 5 hours of light exposure (Figure 3.9.1 and 3.9.2) appearing for both planar and nanowire geometry solar cells is a result of higher electric field near the interface due to the accumulation of ionized copper vacancies. The creation of this accumulation layer close to the interface increases the probability of carrier collection within this layer. Since the layer is very close to the interface, short wavelength photons, photons with energies just below the absorption edge of ZnO, will be absorbed in this layer. From the toy model in the previous section, we can see that the result of copper vacancy accumulation was also a decrease in electric field in the region beyond the accumulation layer. Minority carriers that were generated by longer wavelength photon, that were previously collected by the electric field, no longer are able to drift to the interface for carrier collection. As a result, the EQE decreases for low energy photons and increases for high energy photons (Figure 3.9.2), manifesting in a blue-shift of the EQE curve (Figure 3.9.1).

As seen in Figure 3.7.2, the absorption length is directly correlated to the wavelength of incident light, so an EQE measurement can be used to measure the car-

rier collection efficiency as a function of depth in the Cu_2O. For depths with an increased copper vacancy concentration, the electric field and carrier collection efficiency are increased. For depths with a decreased copper vacancy concentration, the electric field and carrier collection efficiency are decreased. Therefore, the change in EQE can be seen a depth profile for the change in the copper vacancy distribution, which is evidenced by the similarity in Figure 3.9.2a and the copper vacancy density profile after accumulation in Figure 3.9.7.

For the planar solar cell, the changes in copper vacancy distribution occur evenly everywhere along the interface. In contrast, we believe that this initial change in copper vacancy redistribution is due to only an accumulation at the tips of the nanowires. Between nanowires, the Cu_2O is completely depleted and lacks the strong electric field needed to cause the drift of ionized copper vacancies (Figure 3.9.8). At the tips of the nanowire, the Cu_2O extends enough to sustain the full V_{bi} with a full depletion layer. The electric field in this depletion layer can move the ionized copper vacancies to accumulate at the tips of the ZnO nanowires.

After 5 hours, the shifting ceases in both planar and nanowire solar cells. From our model, both drift and diffusion of ionized copper vacancies take place. After sufficient accumulation of copper vacancies at the interface, the concentration gradient becomes large and begins to drive back diffusion at a similar rate to the drift of ionized copper vacancies. Another possibility is that some compensation from the hydrogen defects in ZnO could be slowly eliminating the accumulated copper vacancies. Either case or a combination of both effects could result in a steady state of accumulated ionized copper vacancies at the interface.

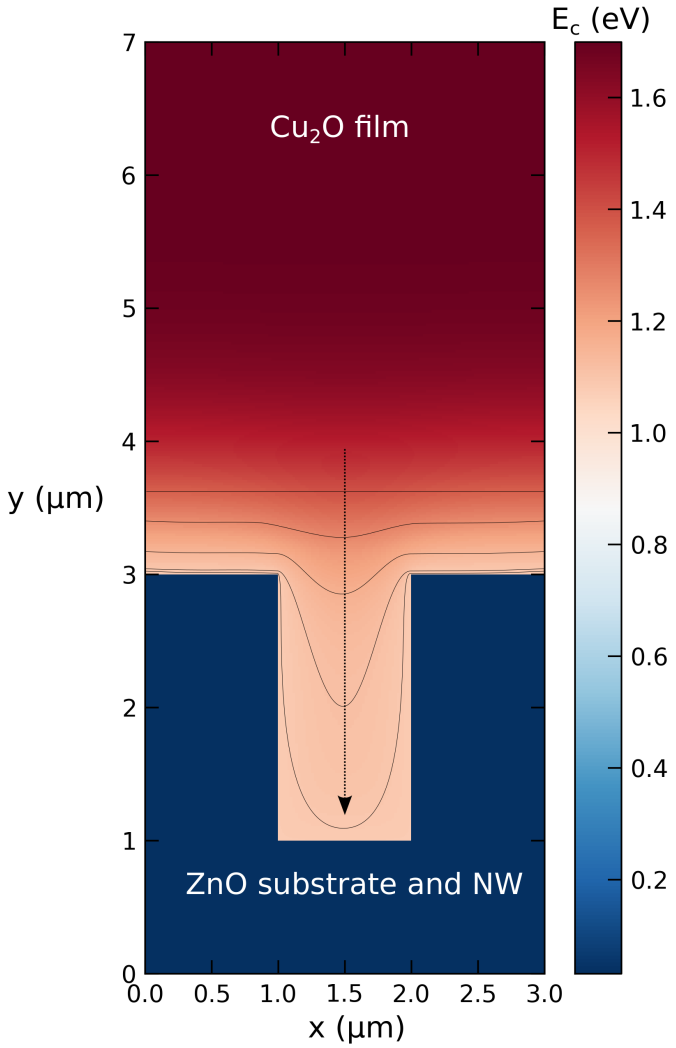

Figure 3.9.8: 2D simulation of the conduction band for a nanowire ZnO/Cu_2O junction. The lines represent the moving front of the high electric field region as copper vacancies move to the region between nanowires.

3.9.5 Red shift of the EQE at long times in nanowire solar cells

In the previous section, we considered the accumulation of ionized copper vacancies in the short time regime (< 6 hours). For planar solar cells, a quasi-steady state is reached. Figure 3.9.1 showed that EQE did not change much for the planar solar cell after 5 hours. On the other hand, the EQE in the long wavelength regime continues to evolve in the nanowire solar cell.

As previously mentioned, the region between the nanowires is completely depleted initially. From Figure 3.9.8, it appears that the effect of the nanowires on the energy band profile is merely smeared out over the nanowires. In other words, a minority carrier, generated in a region above the nanowires, would not feel any effect of the nanowires. Still, diffusion of minority carriers leads to the charge separation between nanowires at the type II heterojunction interface of ZnO and Cu_2O despite the lack of electric field in the region between nanowires.

However, after the drift of ionized copper vacancies causes accumulation near the tip of the nanowires, the redistributed electric field is closer to the nanowires. The electric field is no longer smeared out over the nanowires but instead begins to conform to the outline of the nanowires and causes drift of ionized copper vacancies into the region between nanowires. As a result, the region of Cu_2O between ZnO nanowires slowly becomes rich with ionized copper vacancies. The electric field increases along the full length of the nanowire. Thus, minority carriers generated by lower energy photons in this region of enhanced electric field between the nanowires have a greater probability of being collected. The higher collection probability is manifested by the slowly increasing EQE in the high wave-

length regime (Figure 3.9.2b), which appears as a red shift in the EQE for nanowire solar cells (Figure 3.9.1b).

3.9.6 Lack of shifting EQE when light is off

The shifts in EQE described in the previous sections require light. Between each EQE measurement, the device was illuminated with white light. The illumination ensured that the device was constantly in its photoconductive state. Alternatively, when a similar test was done but without the white light illumination between EQE measurements, no shift was observed (Figure 3.8.2). In agreement with the observed persistent photoconductivity in Cu_2O in literature and in our devices, the decay of photoconductivity is an exponential decay[164, 171–173]. Effects of the initial exposure to light may persist for very long times, but the proportion of ionized copper vacancies decreases rapidly after illumination ceases. When most of the copper vacancies become compensated by donor defects within the Cu_2O (the origin of PPC in Cu_2O), they lose their charge and are not affected by the electric field. Therefore, the drift of ionized copper defects is minimized by the limited availability of ionized copper defects, and the EQE does not shift.

3.10 Darkening of Cu_2O with light exposure

Both accumulation of ionized copper vacancies and the compensation of these ionized copper vacancies at the interface by hydrogen in the ZnO or another compensating defect are possible and likely. The compensation of the ionized copper vacancies result in a defect complex that is neutral. There are likely to be both an ex-

tremely high concentration of ionized copper vacancies and a high concentration of ionized hydrogen interstitials at the interface that are available for compensation process. Other possible compensating defect complexes that may form include copper divacancies[170] or copper vacancy-oxygen vacancy complexes[164]. As a result of many charged defects being compensated, complexing, and becoming neutral, voids may form at the interface. These voids can increase the scattering of light and make it seem like the film is becoming darker. Another compensating mechanism is the oxidation of copper(I) to copper(II). With a very high number of copper vacancies, it is possible pockets of CuO to form at the interface[165].

After these long exposures to bright light, the nanowire solar cells appeared darker than the flat solar cells. Pictures were taken to show the effects of long light exposure on the visual appearance of the solar cells, especially the nanowire solar cells. Since the entire solar cell was not illuminated during the test, the shadowed regions act as a control for the effect of light exposure on the visual appearance of these solar cells. Absorption measurements were done to monitor the change in the absorption after long exposures of light. Absorption still increased dramatically at the wavelength corresponding to the Cu_2O bandgap. At photon energies lower than the bandgap, background absorption increased slightly for areas that had been exposed to light for long periods of time. However, no other distinct changes were observed for the darker regions.

Figure 3.10.1 shows the resulting absorption spectra for solar cells that have been exposed to white light for long periods of time. Figure 3.10.1c shows the change in absorption for each type of solar cell. The gradual increase in absorption

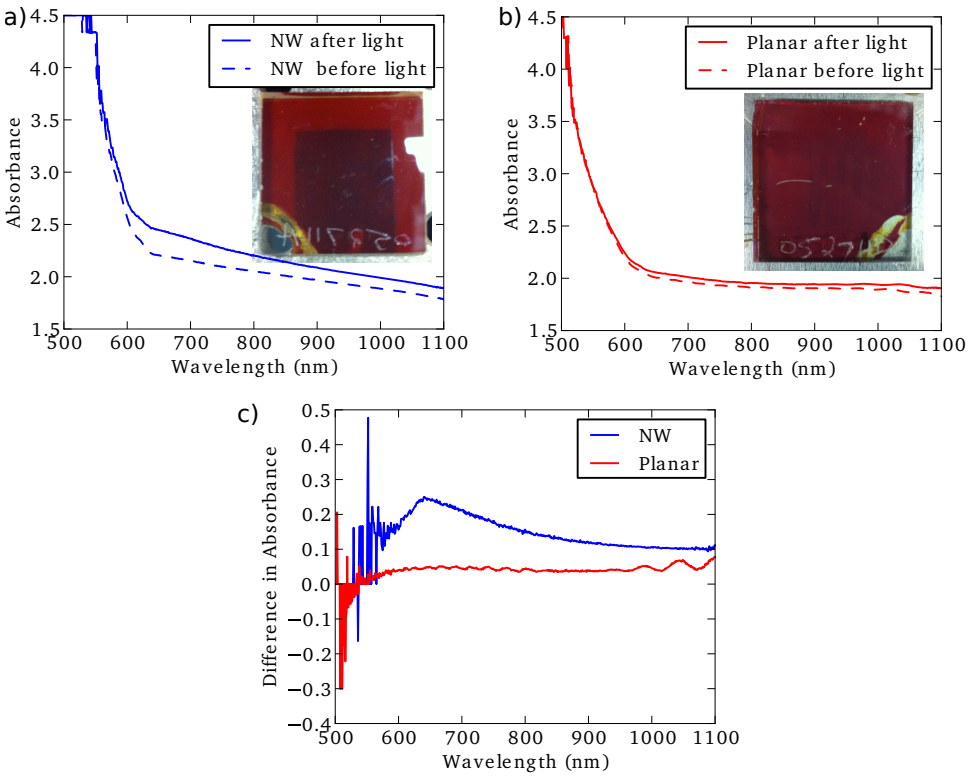

Figure 3.10.1: Comparison of darkening in ZnO/Cu_2O solar cells after long light exposure. (a) Nanowire ZnO/Cu_2O solar cell darkened after long light exposures. (b) Flat ZnO/Cu_2O solar cell remained the same even after long light exposures. c) Difference in absorbance before and after long light exposure for flat and nanowire solar cells.

until 640 nm may be indicative of the formation of CuO, an indirect bandgap material with reported bandgaps between 1.4-1.7 eV[191]. The wavelength-dependent change in absorption in the nanowire solar cell is consistent with the transformation of some Cu_2O to CuO. An alternative explanation is the formation of voids due to the vacancy accumulation at the interface[83]. The formation of small voids on the order of the wavelength of light could scatter light and increase the absorption. When the darkened area of a nanowire solar cell was cross-sectioned and inspected under the SEM, no large voids could be identified. Although the disorder of the nanowire array could make possible voids hard to see, nanowires still maintained intimate contact with the Cu_2O matrix. For these reasons, we believe that the formation of voids is not responsible for the darkening of these solar cells.

The darkening effect was only seen in nanowire solar cells after long exposures to white light. This effect is due to the geometry. The CuO forms along the ZnO/Cu_2O interface. In the planar solar cell, the path length through the CuO region is small. The absorption is therefore minimized. However, the geometry of the nanowires allows the path length of a photon through region of CuO that can be as long as the nanowire itself. Therefore, the absorption in the nanowire geometry is much larger.

The formation of CuO, while increasing absorption in the solar cell, did not increase the efficiency of the solar cell. These defects that form in the most critical point in the device, the interface, likely were sites of recombination. Since the EQE is a product of the probabilities of photon absorption and carrier collection, the increase in absorption likely was dominated by the large decrease in carrier

collection.

3.11 Implications

We have shown the ability to control the nanostructure of ZnO with the chemistry in aqueous solution synthesis to create ZnO/Cu_2O solar cells with planar and nanowire architecture. By easily creating both types of solar cells through aqueous methods, we were able to compare the performance of these solar cells as a function of internal architecture. The incorporation of nanowires into the device architecture of ZnO/Cu_2O solar cells proved to increase the carrier collection of minority carriers that were generated by long wavelength photons. As a result, J_{sc} of the solar cell increased by more than 100% and EQE increased substantially in the 500-600 nm range. These result demonstrated that the nanowires can remove the constraint of only being able to efficiently collect carriers generated within a minority carrier diffusion length from the p-n junction.

However, long-term testing remains critical for new solar cell structures and materials. In this case, we studied both a new structure with the nanowire architecture and an unusual material in Cu_2O. We evaluated the aging characteristics in ZnO/Cu_2O solar cells and determined how they depend on the geometry of the device. The difference in aging behavior was stark in comparing planar and nanowire structures. The motion of dopants created a region of enhanced electric field near the interface and a region of lower electric field in the depletion region. In the planar solar cell, the EQE curves simply became blue-shifted. In the nanowire solar cell, the the region of high EQE in the EQE curve expanded due to where

the enhanced electric fields resided in the overall structure of the solar cell. This result was unexpected and was due to the geometry of the solar cell. These results also imply that the dopant distribution in ionic semiconductors like Cu_2O can be creatively engineered to enhance device performance. One method to control the dopant distribution, as demonstrated in this study, is the geometry of the solar cell.

This method of controlling dopant distribution in ZnO/Cu_2O solar cells may be a way to address a fundamental problem in these solar cells. In ZnO/Cu_2O nanowire solar cells, the minority carrier collection length and the depletion width are incompatible lengths[146]. Because the minority carrier collection length is smaller than the depletion width, the choice is either to collect all of the generated carrier, which maximizes current, or design the solar cell to use the entire built-in bias, which maximizes voltage. By effectively doping the regions between nanowires at a higher concentration through dopant diffusion, it may be possible to not sacrifice current for voltage. Full control over the spacing between ZnO nanowires could help in designing better performing solar cells with predictable aging characteristics.

4

Templated growth of ZnO

4.1 Introduction and motivation

In the design of ZnO/Cu_2O solar cells, we showed in the previous section the importance of of controlling ZnO morphology in the device. Using purely bottom-up methods, we switched the morphology of the ZnO from a planar film to nanowires. However, the nanowires themselves were randomly arranged and poorly aligned.

Although the nanowire solar cells proved to be more efficient than the planar solar cells, more control over the geometry of the nanowires could allow better design and higher efficiency solar cells.

The geometrical requirements for many optoelectronic components and devices is much more rigorous than those needed to fabricate solar cells. In dielectric optical structures like waveguides, photonic crystals, and microdisks, the exact geometry of the structure determines the functionality and the relevant wavelength for the optical component. Larger degrees of confinement require more precise control over the dimensions of the component. For example, in a photonic crystal cavity, the displacement of one of the crystalline elements by nanometers be the difference between a working device and a worthless device[192].

Two optical devices in which ZnO can play a critical role are microdisks and single photon emitters. An advantage of the aqueous solution growth of ZnO is the near atomic control of some features in morphology. ZnO grains develop crystal habits that are defined by the surface energies of the ZnO crystal planes. Typically, ZnO grains form in hexagonal cylinders or prisms that are defined by the low-index planes of ZnO, making each face of the ZnO grain extremely smooth and the morphology predictable by growth conditions.

However, the ability to arbitrarily place these optical components in a specific location on a wafer is also extremely important. By templating the growth of these structures, the location of ZnO growth on the wafer and, to some extent, the shape of the structure can be controlled. Previous approaches to templated growth of ZnO have patterned a mask on a substrate by photolithography[113, 114, 193],

electron beam (e-beam) lithography[194], nanoimprint lithography[195], or laser interference lithography[196, 197] and allowed ZnO to grow through the mask. Some authors have creatively used polystyrene-based colloidal crystals to define masks to create ZnO nanowire arrays or ZnO bowls[198]. In order to create optical structures from aqueously grown ZnO, we created undercut ZnO pillar with flat tops to act as whispering gallery mode (WGM) resonators and tapered ZnO nanowires as a part of a nanowire single photon source device.

4.2 ZnO WGM resonators

Recently, several groups have investigated ZnO WGM resonator by taking advantage of the hexagonal cylindrical shape that results from the growth of ZnO[199–208]. The growth techniques used for these works was vapor phase transport, which requires high temperatures and vacuum systems. From the few reports of ZnO WGM resonators formed through solution synthesis, none of them made the ZnO structure directly on a substrate in a controlled manner[206, 209, 210]. Instead, ZnO microdisks, nanodisks, and microrods are formed in random location with random orientations on the substrates. It may be that the ZnO structures formed in solution and merely adhered to the substrate as the substrate was removed from the solution.

In our synthesis, $MgAl_2O_4$ was used as a substrate. $MgAl_2O_4$ is known as a substrate suitable for the epitaxial growth of ZnO[110]. A continuous, epitaxial thin film of ZnO was first formed on the substrate. The film was patterned with standard photolithography or e-beam lithography. Finally, ZnO was grown through

the pattern to obtain undercut hexagonal structures.

In order to achieve ZnO epitaxy, the substrate had to be cleaned extremely well. The substrate was cleaned in ultrasonically cleaned in acetone and isopropanol. Residual organic surface contaminants were burned off by annealing at 800°C for 8 hours. A "nucleation" layer of ZnO was epitaxially formed on the substrate by suspending the substrate into a solution A, which consisted of 0.2 g of zinc nitrate hexahydrate and 1.25 mL of 15 M ammonium hydroxide in 24 mL of deionized water, and microwave heating it for 25 seconds. The sudden increase in temperature to nearly 100°C caused very small pillars (100 nm tall) to grow epitaxially and densely on the surface of the substrate. A second growth step to grow a continuous thin film of ZnO was performed by by suspending the substrate into a solution B, which consisted of 0.2 g of zinc nitrate hexahydrate, 0.05 g of sodium citrate tribasic dihydrate, and 1.25 mL of 15 M ammonium hydroxide in 24 mL of deionized water, and heating it to 90°C for 18 hours. On some samples, standard photolithographic techniques were used with Shipley 1800 series photoresist to pattern holes of various sizes. On other samples, e-beam lithography was done using PMMA and standard e-beam lithography procedures to pattern smaller holes. After lithography and development, the samples were again suspended in solution B at 90°C for times between 2 hours and 4 hours, creating a hexagonal ZnO structure with a flat top. The photoresist or e-beam resist was removed with acetone, leaving an undercut ZnO structure. We will refer to these structures as "microdisks" for the remainder of this chapter.

Figure 4.2.1 shows a cross section of ZnO growing along the curved shape of

the photoresist, proving that the ZnO can be molded by using resist as a template. Figure 4.2.2 shows the microdisks that are formed growing ZnO through circular patterns in photoresist. The curved stem region indicates that the contrast of the photoresist was poor. Therefore, the undercut was not as sharp as desired. More than 2.25 hours of growth through the patterned photoresist were required to obtain a structure that resembled a hexagonal disk. Figure 4.2.2a shows that for times under 2.25 hours, the the microdisk still lacked the defined crystal facets that are often seen in single crystal ZnO structures. However, for microdisks that grew for longer than 2.25 hours, the facets were extremely smooth, the roughness being much smaller than wavelengths of visible light.

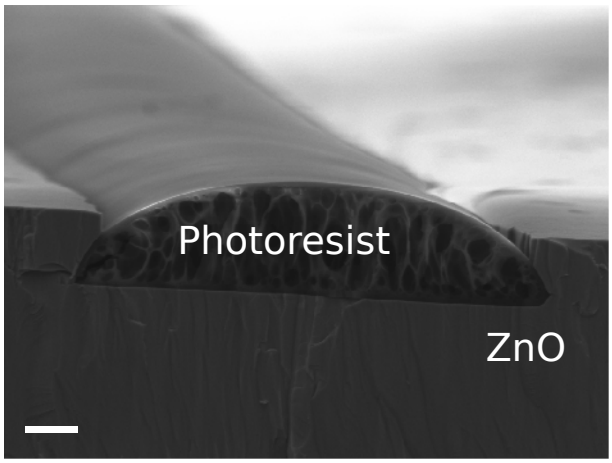

Figure 4.2.1: SEM micrograph of ZnO growth following the shape of photoresist. Scale bar = 2 μm.

At these time scales for growth, the vertical growth rate is approximately equal to the horizontal growth rate as evidenced by the shape of the microdisk. While the citrate ions in the growth solution slow down c-axis growth of the ZnO, it does

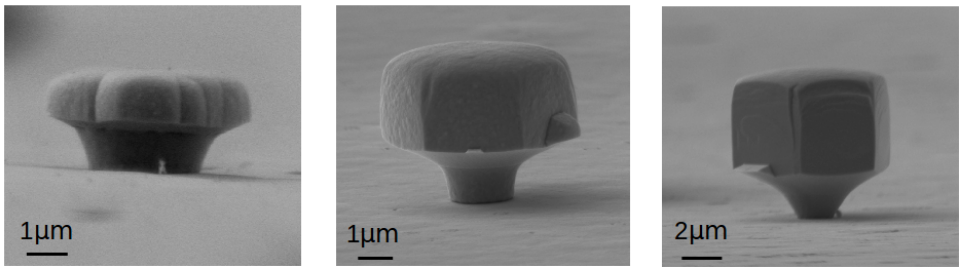

Figure 4.2.2: Time series of ZnO microdisks grown through photoresist.

not affect the growth of the other planes of ZnO[107, 210]. Therefore, microdisks with an aspect ratio of less than 1 should not be expected with this growth technique.

After 3 hours of growth, one of the samples was again immersed in solution B at 90°C for 4 hours 50 minutes. Surprisingly, the microdisk continued to grow on the single crystal of ZnO without any obvious defects signalling that growth was interrupted.

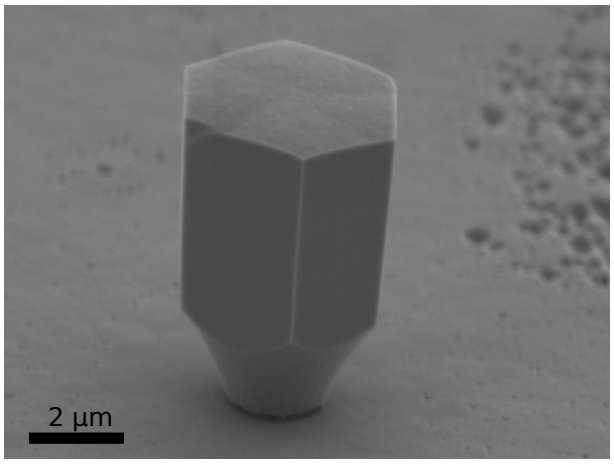

Figure 4.2.3: SEM of microdisk whose growth was interrupted and resumed

Because of the poor resist contrast with photolithography, e-beam lithography was used to create a much sharper undercut. Figure 4.2.4 shows a series of microdisks formed by growing through various size holes in the patterned e-beam resist. The facets of the microdisk were very smooth, except for the base of the microdisk. A defective region circumscribed many of the microdisks formed through e-beam lithography. However, the undercut in these microdisks were are superior to those defined by photolithography.

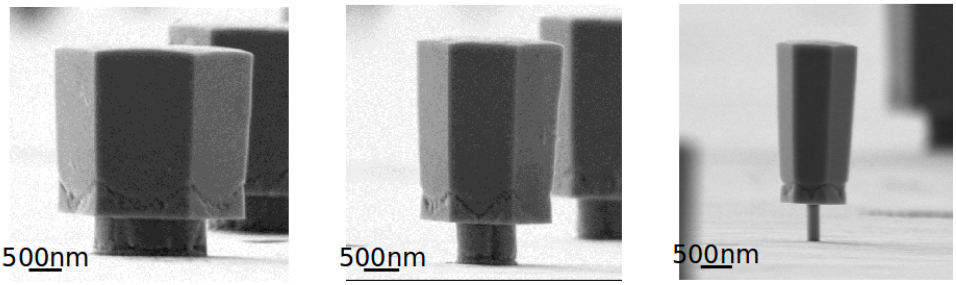

Figure 4.2.4: Series of ZnO microdisks grown through e-beam resist. The hole size through the e-beam resist was varied: (a) 2 μm, (b) 1 μm, and (c) 200 nm.

The defective region at the base of the e-beam defined microdisks is peculiar. The way that the diameter of the microdisk decreases at the center of the defective region is reminiscent of twinning in ZnO microplates[211–213] and microrods[100, 206]. Dai et al.[206] explains the growth of the twin-rods by attributing different growth mechanisms to the (0001) plane and the $(000\bar{1})$ plane of ZnO. As the ZnO grows through the patterned hole, it grows both horizontally and vertically, causing the sides of the microdisk to slant away from the center. Figure 4.2.5 describes two scenarios. In the first case (Figure 4.2.5a), the horizontal and vertical growth

rate are constant throughout growth process. The resulting sidewalls would have a constant slope. In the second case (Figure 4.2.5b), the horizontal growth rate decreases as growth progresses, as described by He et al., who claim that a critical concentration of nutrient ions is required for horizontal growth[214]. As the concentration of nutrients in the closed system decreases during the growth, the horizontal growth rate also decreases. Since the bottom of the microdisk becomes exposed to the solution, a different mechanism of growth on the $(000\bar{1})$ could be responsible for growth in the downward direction. As the space fills in, the defective region is formed.

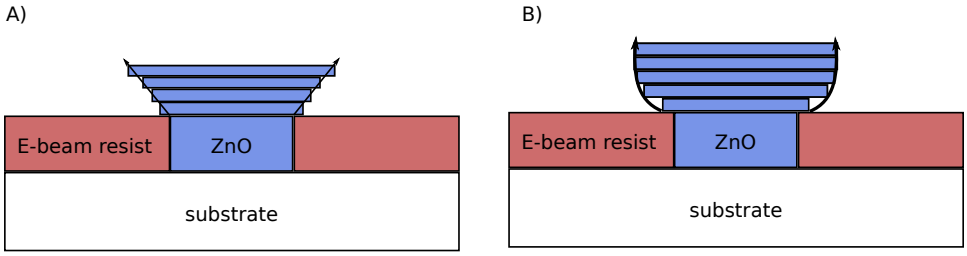

Figure 4.2.5: Schematic of sloping of sidewalls in microdisks. a) Case where the vertical growth rate and the horizontal growth rate are constant throughout the growth process. b) Case where the horizontal growth rate decreases as growth progresses.

We have not been able to detect the presence of whispering gallery modes in these structures through photoluminescence. Even with these minor defects, whispering gallery modes should be able to be detected through photoluminescence if one compares the quality of these structures with those structures that report WGM in literature[206, 209, 210]. Despite the failure of detecting WGMs, we have shown the ability to manufacture ZnO structures that resemble WGM res-

onators at precise locations on a substrate through standard lithography techniques.

4.3 Tapered ZnO nanowires for enhancing photon extraction from a single photon source

The search for a solid-state single photon source is essential in fulfilling the technological advances promised by quantum computation and information processing [215]. The potential benefits for using the GaN nitride family of materials to serves as a single photon source are numerous. The large built-in electric field found along the c-axis of GaN could be used to probe large two-qubit interactions[216]. The wide range of wavelengths available to the nitride family enlarges the potential applications for a nitride single photon source[217]. Furthermore, nitrides have a potential for being able to perform at higher temperatures and can be electrically contacted[217].

Quantum dots in GaN have the potential to be single photon sources[217], but the extraction of emitted photon is complicated by the high index of refraction of GaN. Only 3% of emitted light in LEDs are extracted[34]. This low extraction efficiency poses a serious problem for engineering a reliable single photon emitter in GaN. To address a similar problem in the GaAs system, Claudon et al. used a tapered nanowire to guide photons away from the emitter and avoid scattering at the top facet of the nanowire[218]. We propose a similar approach using ZnO nanowires grown on GaN to extract emitted photons from embedded InGaN quantum dots. In order to enable this technology, tapered ZnO nanowires must be epitaxially grown over a single InGaN quantum dot.

In order to demonstrate the ability to do grow tapered nanowires at pre-determined locations, we used a thin film, gold mask with apertures having diameters between 100 nm to 2 μm and grew through the apertures where only the GaN surface was exposed. The gold mask was prepared through metal lift-off that was patterned with standard e-beam lithography. The gold was deposited in a thermal evaporator with thin layer of chromium (2nm) used as an adhesion layer. The sample was cleaned in oxygen plasma for 5 minutes at 150 W to remove residual organic contaminants. For ZnO growth, the samples were immersed in solution A (ZnO growth solution without citrate) at 90°C for 4, 6, and 17 hours without the deposition of a nucleation layer.

Tapered nanowires were grown from the apertures in the gold film. The height of the nanowires did not vary systematically with the tested times. Likely, most growth stops after around 4 hours. Figure 4.3.1 shows one of the smallest diameter nanowires. The diameter of the nanowire was 270 nm and the height was 4.2 μm. The smallest diameter apertures did not have any nanowires growing from them. On the other hand, the largest apertures often had multiple microwires of ZnO growing from the same aperture. Since ZnO grows epitaxially on GaN[35, 111, 112], all of the ZnO nanowires were vertically aligned from the surface.

Curiously, many nanowires did not occupy the entire space allotted by the aperture as in Figure 4.3.1a. Cole et al. observed that, in Mg-doping GaN, the Mg oxidises at the surface when exposed to oxygen plasma[193]. The MgO at the surface then blocks OH^- attachment to the surface, effectively blocking ZnO nucleation and growth. Although their growth chemistry is slightly different, the same pro-

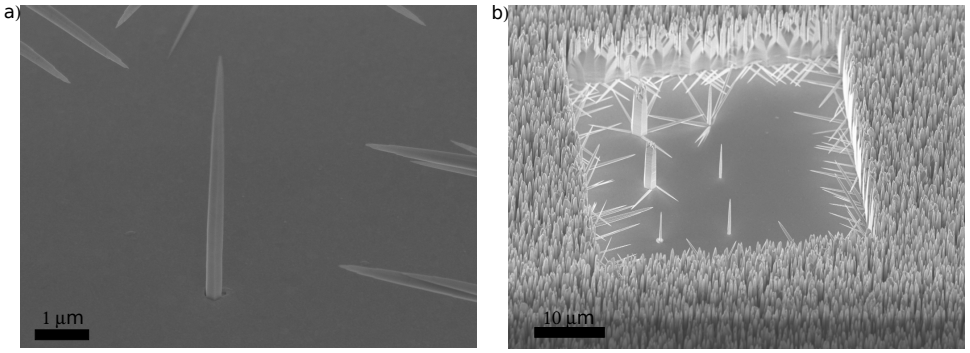

Figure 4.3.1: SEM of tapered ZnO nanowires grown on GaN though Au film apertures. a) Single ZnO nanowire. b) The entire array of aperture sizes from 100 nm to 2 μm.

cess could be occurring here. Some portions of the GaN surface may have MgO blocking nucleation and growth of ZnO. Therefore in some apertures, only a fraction of the apertures is used by the growing ZnO nanowire.

We have seen how difficult good control over the exact shape and position can be. In our case those difficulties were manifested in the defects at the base of the microdisks and off-centered growth of nanowires in apertures. Yet, we have demonstrated the ability to purposefully grow in place ZnO optical components and devices and taken a step in the formation of useful bottom-up ZnO optical devices.

5

Aqueous epitaxial growth of ZnO on single crystalline Au microplates

5.1 Introduction

The quality of metal/oxide interfaces is an important determinant of the efficiency of electrical[219], plasmonic[220, 221], and catalytic devices[222]. Typically,

metal/oxide interfaces are formed by vapor-phase deposition, resulting in polycrystalline films with various morphologies, textures, grain sizes, and orientations. Here we demonstrate a method for growing epitaxial ZnO from an aqueous solution at 90°C on single crystalline Au microplates. These results could have important implications on the advancement of metal/ZnO-based electronic devices[223], plasmonic devices[224, 225], and heterogeneous catalysts[226, 227]. As seen in previous work, in which epitaxial ZnO was used as a current spreading layer in GaN LEDs[35], and in Chapter 4, where the epitaxal growth was critical in the templated growth of ZnO, epitaxial growth on a commonly used metal, like gold, can enable many more optoelectonic applications for ZnO, in which metal-semiconductor integration is essential.

While epitaxial growth of ZnO on nearly lattice-matched substrates, including GaN[228], sapphire[9, 229], and SiC[229], has become well established, heteroepitaxy with metals has not been as well explored. The common challenges of epitaxial growth on highly dissimilar materials[230] apply to the Au/ZnO system as well. Au and ZnO have different crystal structures, chemical bonding, and lattice constants. Gold has a face-centered cubic (FCC) crystal structure with a lattice constant a = 0.4079 nm. ZnO has a hexagonal wurtzite crystal structure with lattice constants a = b = 0.3250 nm and c = 0.5207 nm. In the close-packed plane of each structure, this yields a lattice mismatch of

$$(a_{ZnO} - a_{Au}\sqrt{2}/2)/(a_{Au}\sqrt{2}/2) = 12.7\%. \tag{5.1}$$

Despite these challenges, there has been some success in epitaxial growth of

ZnO on Au[231]. Because the thermal expansion coefficients of the two materials are so different, low temperature deposition techniques have been crucial in their heteroepitaxy. Aqueous, epitaxial electrodeposition of ZnO nanopillars on large single crystalline gold substrates has been demonstrated[232, 233]. However, smooth ZnO films are often required for most practical optoelectronic applications. Additionally, gold, while ubiquitous in semiconductor technologies and plasmonics, is rarely used as single crystalline substrates. Recently, a simple thermolysis procedure for producing very large, gold microplates[234, 235] has been developed. These plates are single crystalline, making them atomically smooth and ideal for modular plasmonic[234] and microelectronic devices.

Our technique is a simple solution-based aqueous synthesis, and, unlike the previously demonstrated epitaxial electrodeposition of ZnO on Au[232, 233], does not require an external electrical bias. Another advantage of our work is that we demonstrate the coalescence of epitaxial ZnO columns into a smooth, thin film; which is essential for most device fabrication. The single crystalline gold plates can also be grown on any substrate that can survive the 130°C deposition and be stable in the growth solution[235]. The simple synthesis method for obtaining epitaxial ZnO therefore opens more opportunities for modular Au/ZnO devices made through bottom-up processes.

5.2 Experimental methods

Single crystalline Au microplates were first grown on Si substrates by thermolysis of $(AuCl_4)^-$-tetraoctylammonium bromide (TOAB) complex in air[234, 235].

Briefly, 3.2 mL of 25 mM hydrogen tetrachloroaurate(III) hydrate in deionized water were mixed with 8 mL of 50mM tetraoctylammonium bromide (TOAB) in toluene. After vigorous stirring, the top layer, consisting of a Au-TOAB complex in toluene, was separated and drop-cast onto a Si substrate. The substrate was heated to 130°C on a hotplate for 24-48 hours and gently rinsed with toluene and dried.

Aqueous ZnO deposition followed procedures similar to those reported in literature [110, 112, 236]. In order to maintain control over film morphology, a two step method was used to separate the nucleation and growth of the ZnO films as much as possible. The nucleation step was either done by rapid heating using a microwave oven or by slow heating in a conventional oven. Substrates were cleaned with an Anatech 106 oxygen plasma barrel asher for 1 minute immediately prior to seed layer deposition to remove adsorbed organic contaminants. For the microwave-based nucleation, the substrate was suspended with the growth-face facing down in a solution of 0.2 g zinc nitrate hexahydrate, 1.25 mL of 15 M ammonium hydroxide, and 24 mL of deionized water in a Teflon vessel. The vessel was heated on high power for 25 seconds in a microwave oven (GE model JES738WJ02), heating the solution to approximately 95°C very rapidly. The substrate was immediately removed from the vessel after heating, gently rinsed in water, and dried. For nucleation in a conventional oven, the substrate was identically suspended face down in a Teflon vessel with the same solution. The vessel was then kept at 90°C in an oven for at least 1.5 hours. Afterwards, the sample was removed, gently rinsed in water, and dried.

The second step was to grow the nucleated seed layer into a continuous, co-

alesced film. The growth solution consisted of 0.2 g of zinc nitrate hexahydrate, 1.25 mL of 15 M ammonium hydroxide, 24 mL of deionized water, and 0.05 g of sodium citrate tribasic dihydrate. Again, the substrate was sealed in a Teflon vessel face down in the solution and heated in a conventional oven to 90°C for 4-24 hours. The growth rate decreases substantially after the first 4 hours, but some samples remained in the oven for 24 hours to ensure completion of the growth process. Afterwards, the substrate was removed, gently rinsed in water, and dried.

To reveal the bottom surface of the ZnO, the sample was flipped and pressed onto a new, resist-coated Si substrate. AZ 5214E (Clariant) photoresist was spun onto the Si substrate 2000 rpm for 30 seconds, then soft-baked at 100°C for 1 minute, resulting in a resist thickness of approximately 2 μm. A metal block weighing 1.6 kg was placed on top of the sandwich structure, and the structure was heated to 130°C, above the glass temperature of the photoresist[237]. The sandwiched structure remained at 130°C for 30 minutes and was slowly cooled back to room temperature. The metal block was then removed, and the two Si substrates were separated with tweezers. As a result, some of the microplates were transferred into the layer of photoresist on the new Si substrate. This sample, with flipped microplates on it, was dipped into Au etchant Type TFA (Transene Company) until all Au was removed. Since the Au microplates were of various thicknesses, the total etching time also varied from 10 minutes to 60 minutes. The bottom surface of the ZnO was revealed after all of the Au was removed.

Scanning electron microscopy (SEM) and electron backscattered diffraction (EBSD) were performed using a Supra55VP field emission SEM (Carl Zeiss AG,

Germany) equipped with an EBSD detector. AFM was performed using an Asylum MFP-3D AFM. Photoluminescence (PL) was performed on the grown ZnO using a LabRAM ARAMIS system (HORIBA Scientific, Japan). Samples were excited with a 325 nm (HeCd) laser for PL. Cross-sectional specimens for transmission electron microscopy (TEM) were prepared using the "lift-out" technique in a focused ion beam (FIB) (Zeiss NVision 40) system. TEM (JEOL-2100 at 200kV) and selected area electron diffraction (SAED) were conducted in order to study the orientational relationship between the Au and the ZnO. The HRTEM micrograph was acquired using a Zeiss Libra 200 monochromic, Cs-corrected transmission electron microscope (TEM) at 200 kV (Cs-corrected to -1μm).

5.3 Results and discussion

ZnO films on the Au microplates were made by a two step procedure to separate nucleation and growth as much as possible, and therefore to exercise better control on the structure and morphology of the ZnO. We refer to the ZnO grown on the Au microplates after the nucleation step as the seed layer. Growth of the ZnO proceeded by slowly decreasing the solubility of zinc species in solution through the gradual elevation of temperature[106, 236]. The main difference between the nucleation step and the growth step was the speed at which the temperature was raised. Figures 5.3.1b,d and 5.3.2a,c show schematics of the overall structure of ZnO grown on Au microplates at the different stages of synthesis. Also shown are micrographs from scanning electron microscopy (SEM) of the ZnO film at various stages of growth. Overall film morphology could be changed from flat and smooth

(Figure 5.3.1b,c and 5.3.2a,b) to rough and faceted (Figure 5.3.1d,e and 5.3.2c,d) by altering the kinetics of the nucleation step.

When the nucleation step was fast, the resulting ZnO film after the growth step was smooth (AFM RMS roughness was 7nm) and uniform in height. Individual grains were nearly impossible to discern by SEM (Figure 5.3.1g). Microwave heating was used to raise the temperature to 90°C in 25 seconds in order to make the nucleation step fast and increase the rate of ZnO formation. Figure 5.3.1c shows that the initial seed layer was composed of small densely packed ZnO crystallites on the Au surface. The crystallites were faceted with the expected hexagonal crystal habits and had a columnar structure. The height of each crystallite was uniform across the surface of each Au microplate. Each crystallite grew and coalesced during the growth stage at the same rate, resulting in a smooth ZnO film.

Conversely, a conventional oven raised the sample temperature to 90°C over 1.5 hours, resulting in a much slower nucleation rate. It has been previously shown by Wen et al. that ZnO nanowire arrays may grow without the aid of a seed layer on metal films[24]. The nucleation step in the oven described in this work is akin to a very short growth by the method described by these authors. The final ZnO film morphology was composed of many large, hexagonal grains of ZnO with each hexagonal grain oriented in the same direction (Figure 5.3.2d). The alignment of each grain indicates that there was an epitaxial relationship between the film and the substrate. Each grain appears smooth and sharply faceted, but since the film is composed of many of these grains, each with a different height, the overall film is

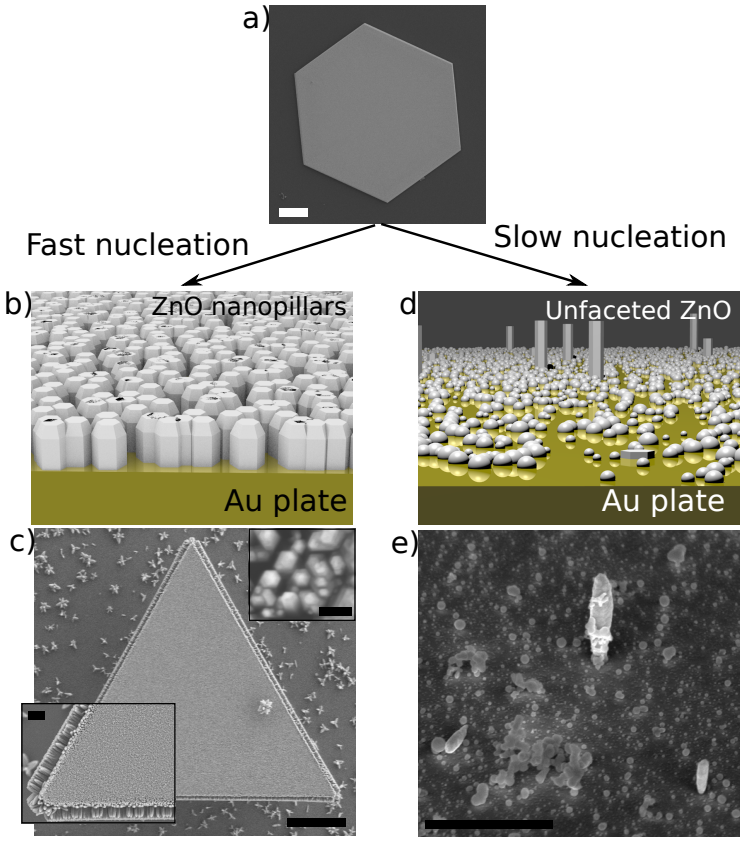

Figure 5.3.1: Film morphology of epitaxial ZnO nucleation layer on Au controlled through growth kinetics. (a) SEM micrograph of the initial Au microplate. Scale bar = 10μm. Left column: Nucleation and growth steps of microwave-nucleated ZnO on Au. (b) Schematic of dense nanopillars formed on the Au microplate during the fast nucleation step. (c) SEM micrograph showing ZnO on Au microplate after the fast nucleation step. Scale bar = 5μm. Insets show high magnification views of the corner of the plate, showing the uniform height of the nanopillars (lower left, scale bar = 1μm), and middle of the plate, showing the crystal habits (top right, scale bar = 200nm) of the ZnO. (d) Schematic of sparse, unfaceted ZnO of varying sizes on a Au microplate formed during the slow nucleation step. (e) SEM micrograph showing Au microplate after the slow nucleation step, viewed at a tilt of 45°. Scale bar = 1μm.

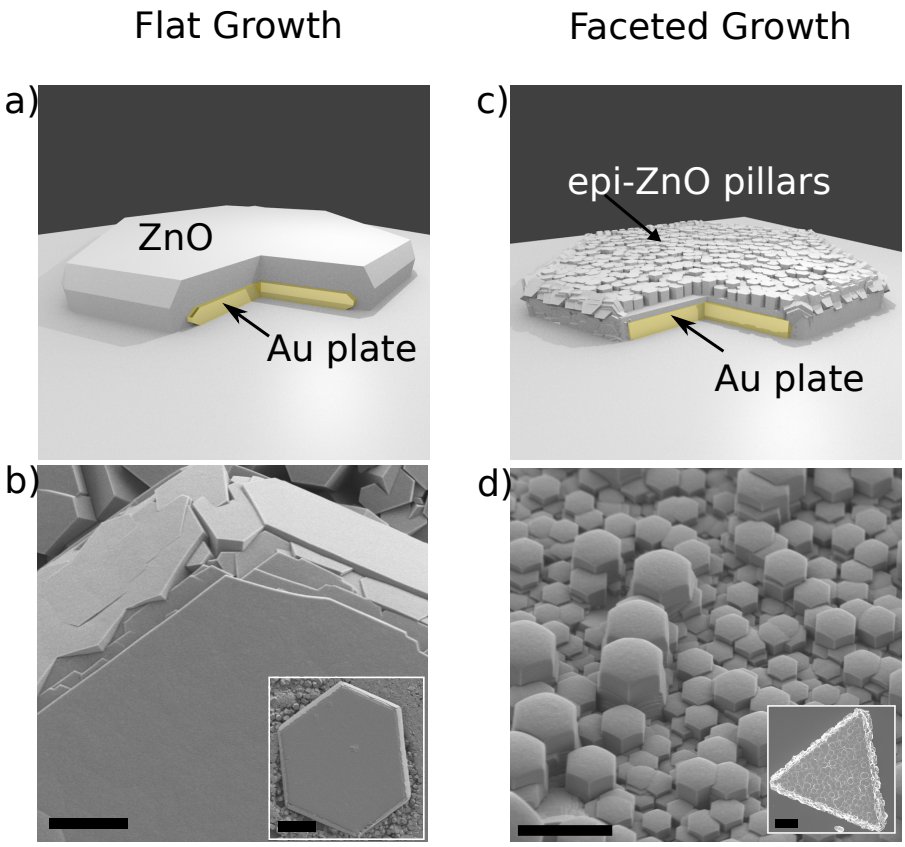

Figure 5.3.2: Film morphology of epitaxial ZnO growth layer on Au controlled through growth kinetics. (a) Schematic of flat ZnO on Au showing the Au substrate underneath a smooth ZnO film. (b) SEM micrograph showing the smooth and flat morphology of microwave-nucleated ZnO after the growth step. Scale bar = 5μm. Inset shows a low magnification view of the entire film on the Au microplate. Scale bar = 40μm. Right column: Nucleation and growth steps of oven-nucleated ZnO on Au. (c) Schematic of ZnO on Au showing the Au substrate underneath a highly faceted ZnO film. (d) SEM micrograph showing rough and faceted morphology of oven-nucleated ZnO after the growth step viewed at a tilt of 45°. Scale bar = 5μm. Inset shows a low magnification view of the entire film on the Au microplate. Scale bar = 20μm.

extremely rough. ZnO grown on the Si substrate, but not on the Au microplates, shows no signature of alignment. Figure 5.3.1e shows that the initial seed layer was composed of islands of ZnO that formed over the course of the nucleation step. ZnO crystallites sparsely populated the surface of the Au. The crystallites that formed were columnar and tall. Because the nucleation did not occur all at the same time, the height of each ZnO column depended on when it was formed during the 1.5 hour period. The largest crystallites were 1 μm tall. A large portion of the surface after the slow nucleation step was populated by granular ZnO particles that lacked any obvious crystal facets. Each of these crystallites, which started growing at different times within the 1.5 hour nucleation period, eventually coalesced into a film during the growth step, resulting in a film composed of large hexagonal grains of different heights.

The final thickness of the film grown by fast nucleation was approximately 3 μm (Figure 5.3.3a) whereas the final thickness of films grown by slow nucleation was approximately 10 μm (Figure 5.3.3b). The discrepancy in the thickness is due selectivity of ZnO growth. The amount of ZnO precursor was the same in both growth solutions, and so we expected to see the total volume of ZnO grown to be equal. When fast nucleation was used, non-selective nucleation occurred on the Si substrate in addition to the nucleation on the Au microplates. Therefore, during the growth step, ZnO was deposited over a large area. In contrast, during slow nucleation, ZnO only nucleated on the metal, which is similar to a previous report[24]. Hence, all of the ZnO growth occurred only on the Au microplates. As a result, the ZnO grown on the slow nucleated samples are much thicker, because

the ZnO grew over a smaller area.

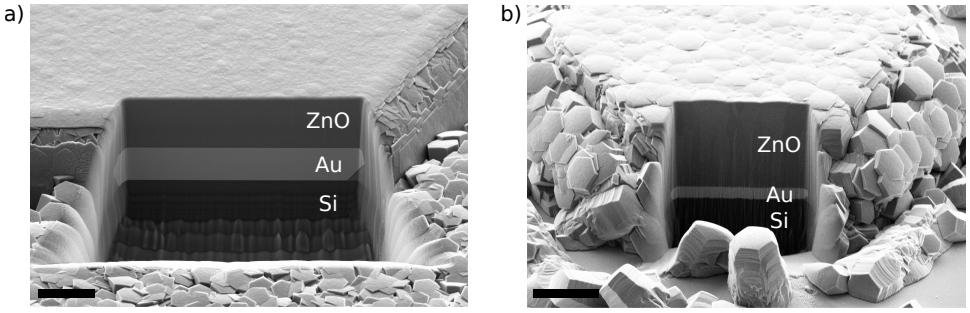

Figure 5.3.3: Focused ion beam (FIB) cross-section of ZnO/Au film. (a) ZnO on Au grown though the fast nucleation method. Scale bar = 4μm. (b) ZnO on Au grown through the slow nucleation method. Scale bar = 10μm.

To examine the bottom surfaces of films produced by both techniques, the films were inverted and the Au was removed using a gold wet etch. The bottom surfaces of the films indicate the quality of the interface on larger scale than cross-sectional TEM and reveal some of the kinetics at the beginning of ZnO growth. The bottom surface of the film produced by fast nucleation was porous (Figure 5.3.4) and had a root-mean-squared roughness of approximately 50 nm as measured by atomic force microscopy (AFM) (Figure 5.3.4b). Rapid nucleation and growth of the ZnO using microwave heating caused gaps to form between each ZnO nanopillar in the initial ZnO layer. Growth of the ZnO nanopillars and their eventual coalescence occurs as the zinc species in solution undergo a condensation reaction at the surface of the nanopillars. However, for films produced by fast nucleation, we believe that the high density of nanopillars makes it difficult for the zinc species to diffuse to the bottom of the pillars, preventing coalescence of the ZnO near the Au surface before access to the solution is cut off by the growing film. SEM and AFM

(Figure 5.3.4c) of the film produced by slow nucleation revealed a much smoother surface (RMS roughness of approximately 4 nm) compared to the film prepared by fast nucleation. Here, the nucleation process is much slower and the seed layer is much less dense. Therefore, the zinc species more readily access the space between ZnO seeds, creating intimate contact with the Au surface. Large grains are visible in the SEM and AFM micrographs, but the boundaries do not correspond to a specific crystallographic direction. We are currently investigating the origin of the boundaries which may result from disturbances in the solution growth during the long nucleation period, such as loose precipitates adhering to the substrate, or deformation in the Au microplate.

Electron backscatter diffraction (EBSD) was used to reveal the single crystalline nature of the ZnO film on the (111) Au surface and infer the epitaxial relationship over large areas. EBSD IPF (inverse pole figure) determined the surface of the ZnO to be a single grain of (0001) ZnO (Figure 5.3.5b) on monocrystalline (111) Au (Figure 5.3.5a). Relative misorientation in ZnO and Au at each measured point on the plate was negligible (Figure 5.3.6), confirming the absence of large angle grain boundaries. The tight distribution of crystallographic directions in both pole figures showed that the Au microplate and ZnO film were single crystalline or very close to single crystalline (Figure 5.3.6a,b). The distribution of crystallographic directions for the Au microplate appeared tighter than for the ZnO film in the pole figures, and the distubution is represented in the histogram of point-to-point angular misorientation (Figure 5.3.6c). A small portion (less than 3%) of the points measured in the ZnO film registered an angular misorientation greater than 2°,

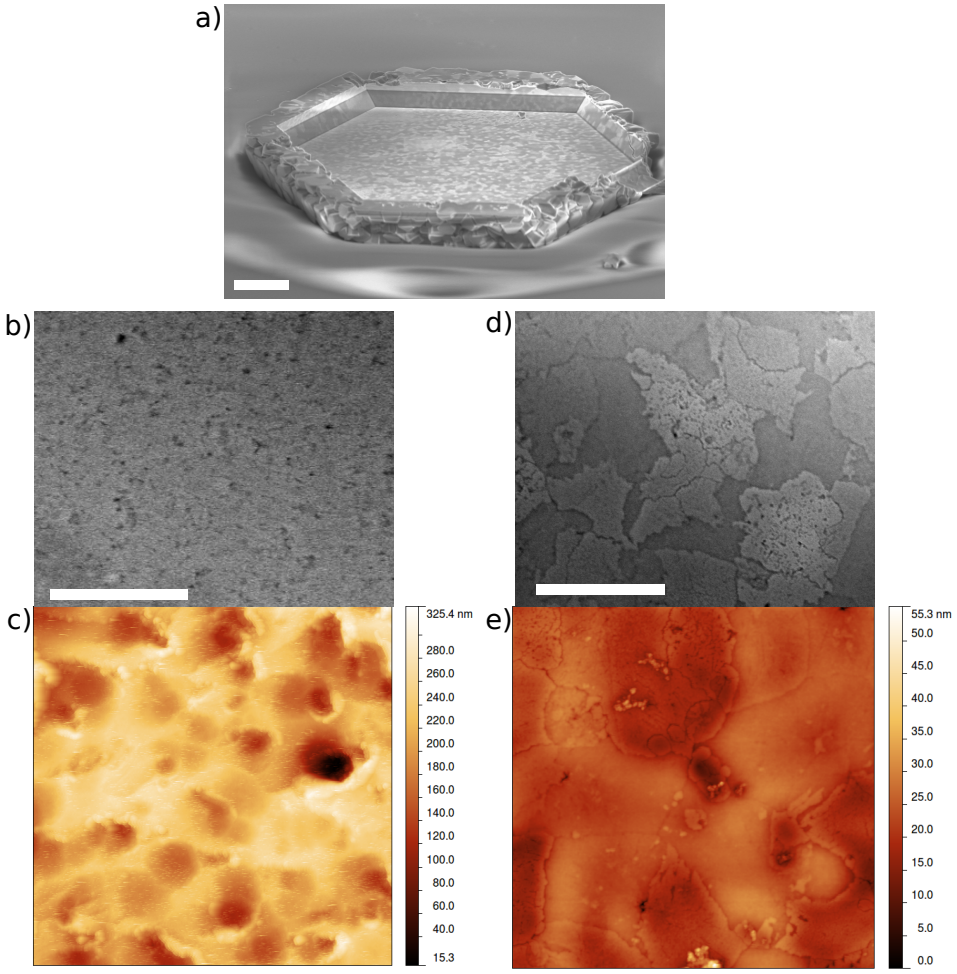

Figure 5.3.4: Bottom surface of the ZnO. SEM and AFM micrographs of the flipped ZnO/Au microplates after the Au has been removed. a) Low magnification, 45° tilt view (SEM) of the entire flipped ZnO membrane embedded in photoresist after Au has been etched away. Scale bar = 10μm. b) Bottom surface of ZnO nucleated rapidly by microwave heating. (Top: SEM, scale bar = 1μm; bottom: AFM, 5μm x 5μm image.) c) Bottom surface of ZnO nucleated slowly by heating in a conventional oven. (Top: SEM, scale bar = 1μm; bottom: AFM, 5μm x 5μm image).

the approximate resolution of the EBSD measurement. The points on the ZnO film with greater than 2° misorientation indicated that small angle grain boundaries were present in the ZnO film.

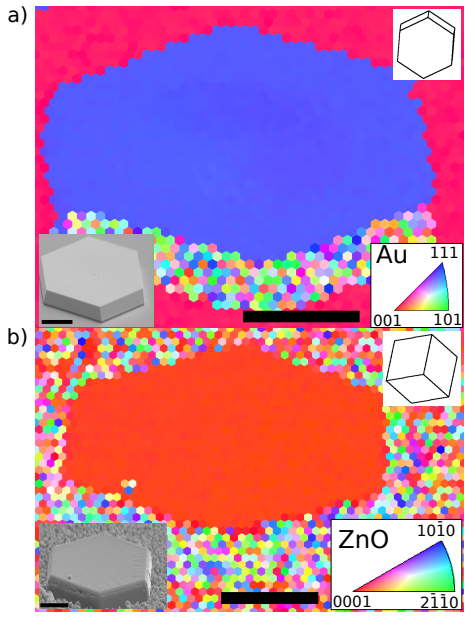

Figure 5.3.5: EBSD of a Au microplate before and after ZnO growth. (a) EBSD IPF map of single crystalline Au microplate. (b) EBSD IPF map of ZnO grown on the same Au microplate. Insets for a) and b): top right indicates the orientation of the unit cell of the Au microplate; bottom left is the corresponding SEM micrograph for the EBSD IPF map. Scale bars = 25μm.

After accounting for the slight difference of rotation between the two SEM micrographs, the unit cell orientations corresponding to the Au microplate and the ZnO are shown in the insets of Figure 5.3.5a,b, which demonstrate the epitaxial relationship. From the EBSD data, we can infer the full epitaxial relationship between the ZnO film and the Au substrate, ZnO $[1\bar{1}00](0002)||$Au $[2\bar{1}\bar{1}](111)$, which persists over the area of the entire Au microplate. The fast nucleation

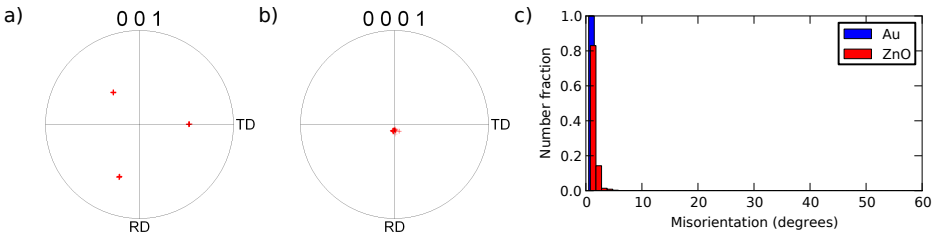

Figure 5.3.6: Angular characterization of a Au microplate and ZnO film from electron backscattered diffraction. a) Pole figure from a Au microplate. b) Pole figure from the ZnO film. c) Distribution of point-to-point angular misorientation of Au plate and ZnO.

method was used to produce the film shown in Figure 5.3.5. However, ZnO films produced by the slow nucleation method also showed the same epitaxial relationship as probed by EBSD. Ultimately, due to the low angular resolution in EBSD, we relied on TEM and electron diffraction to confirm the epitaxial relationship.

Cross-sectional TEM was acquired to confirm the epitaxy between the ZnO film and Au microplate. The ZnO film used in cross-sectional TEM was produced by the fast nucleation process. The high-resolution cross-sectional TEM (HRTEM) micrograph (Figure 5.3.7c) shows alignment between the Au and ZnO planes and a fully crystalline interface between Au and ZnO. Fourier mask filtering was applied to cross-sectional HRTEM micrographs to reduce noise and delineate dislocations present at the interface. Fourier mask filtering is done by first applying a Fourier transform to the original image. A specific filter is used to select only certain spatial frequencies for the subsequent inverse Fourier transform. The inverse Fourier transform reconstructs the real space image from the selectively filtered spatial frequencies. In Figure 5.3.8b, a pattern mask is applied corresponding to the expected ZnO and Au periodicity, resulting in a less noisy image. In Figure

5.3.8c, we selected only the spots in the Fourier transformed image corresponding the set of planes parallel to the dislocations. The resulting real-space image delineates the location of the dislocations. By Fourier filtering the HRTEM image using only the $(11\bar{2}0)$ ZnO and $(02\bar{2})$ Au planes (Figure 5.3.8), we obtained an image that highlights the dislocations. On average, dislocations were present for every 8.7 planes of Au and for every 7.7 planes of ZnO (s_{Au} planes = 1.4, s_{ZnO} planes = 1.3, and n = 38 dislocations). The observed frequency of dislocations corresponds closely with the expected frequency of dislocations when the two lattices are not rotated with respect to each other, 9 Au planes for every 8 ZnO planes (Figure 5.3.7b).

Bright field TEM imaging (Figure 5.3.9) shows a columnar microstructure, signaling that ZnO on Au initially grew in islands before coalescing. Selected area electron diffraction (SAED) was used to index the planes present in the cross-sectional TEM micrograph at the interface (Figure 5.3.7a). (Streaks in the SAED are camera artifacts.) Unexpectedly, two zone axes of ZnO were present in the SAED, indicating that two orientations of ZnO were epitaxial to the Au substrate at the interface: ZnO $[1\bar{1}00](0002)||$Au $[2\overline{11}](111)$, which has no rotation between the two close packed lattices, and ZnO $[\bar{1}2\bar{1}0](0002)||$Au $[2\overline{11}](111)$, which has a 30° rotation between the two close packed lattices(Figure 5.3.7b). The $[1\bar{1}00]$ reflections from the ZnO were much stronger than the $[\bar{1}2\bar{1}0]$ reflections, indicating a preferred and dominant crystal orientation. While the 30° rotation is favored in some epitaxial wurtzite films on cubic (111) surfaces, such as ZnO on

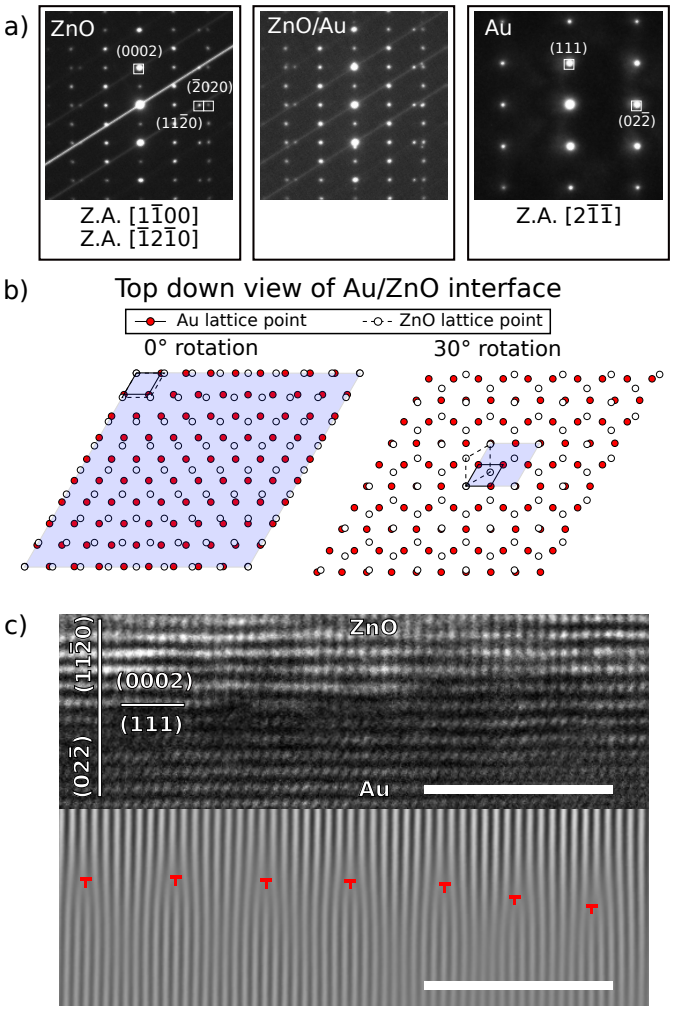

Figure 5.3.7: Cross-sectional TEM and SAED confirm epitaxial relationship between Au and ZnO. a) SAED of (left) ZnO only, (middle) ZnO and Au, and (right) Au only near the interface. b) Schematic of the 2D projection of the close-packed planes of ZnO (0001) and Au (111) at the interface. The solid line represents the unit cell for Au. The dashed line represents the unit cell for ZnO. The shaded region represents the coincidence lattice. The two possible orientations are those with the ZnO lattice rotated 0º and 30º about the [0001] axis with respect to the (111)[111] Au lattice. These orientations correspond to the two epitaxial relationships found in the SAED. c) The top panel shows high resolution TEM micrograph of the ZnO/Au interface. The bottom panel is a Fourier filtered image of the top panel, which highlights shows the misfit dislocations present at the interface. Scale bars = 5 nm.

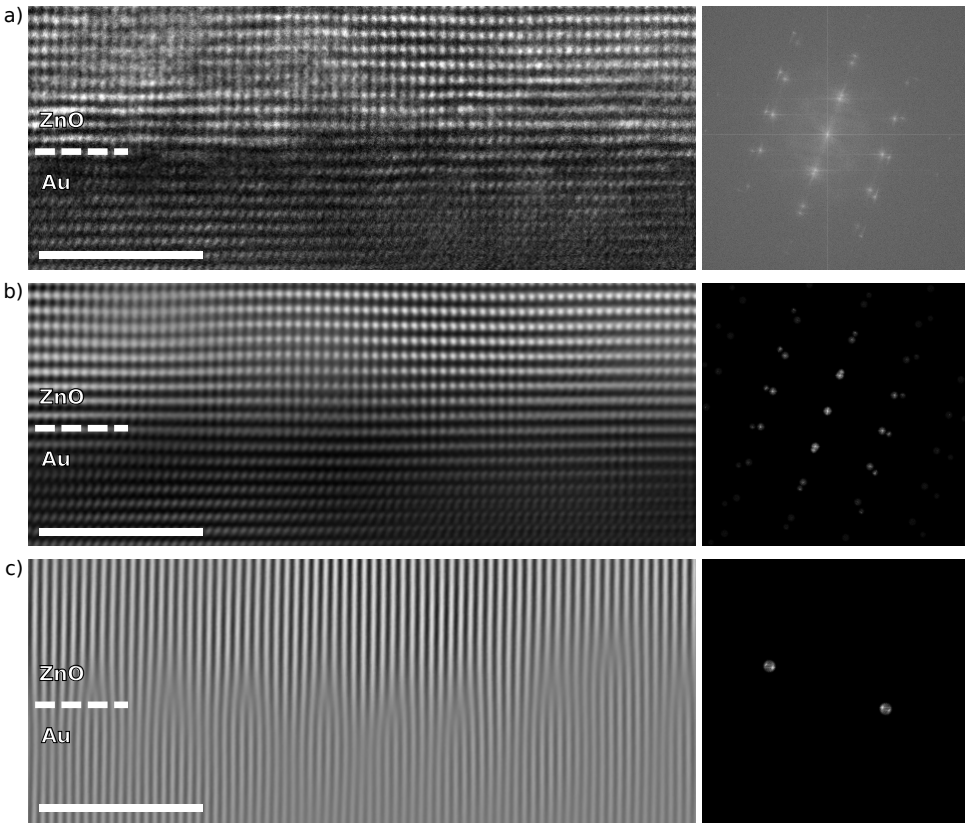

Figure 5.3.8: Image processing of cross-sectional HRTEM micrograph. Left panels show the real space representation. Right panels show the corresponding Fourier transform of the image. Lines delineating the interface are meant to guide the eye. The interface is not completely flat and cannot be represented by a flat line. a) Raw micrograph without any post-processing. b) Fourier-filtered image with pattern mask filtering. c) Fourier-filtered image, selecting only the planes parallel to the dislocations. Scale bars = 5 nm.

$MgAl_2O_4$[110], it is slightly more unusual for an analogous epitaxial system, Ag/ZnO [238]. Both Ag and Au have similar lattice constants, 4.08 Å and 4.09 Å respectively, and the same crystal structure. For the Ag/ZnO system, both epitaxial relationships had similar interfacial energies and the resulting structure was dependent on surface conditions. In experiments of Ag nanocrystal deposition on ZnO[239], both variants were initially observed, but the 30° epitaxial growth was strongly inhibited by the compressive strain in the Ag. In other cases of ZnO grown on textured Ag films by solution growth, the 30° rotated growth was not observed at all[240]. Similarly, since we did not observe evidence of the 30° rotation in EBSD after complete growth of the ZnO films, we believe that the not rotated variant also dominated our growth process.

Finally, to confirm the quality of the ZnO, photoluminescence spectra were measured (Figure 5.3.10). Data presented in Figure 5.3.10 is from ZnO films produced after a fast nucleation step. Similar PL spectra were also obtained from films produced after a slow nucleation step. As-grown ZnO films showed photoluminescence at unexpectedly low wavelengths. Two peaks were resolved at 354 nm and 377 nm corresponding to energies of 3.50 eV and 3.28 eV, respectively, with the peak at 377 nm being more intense. After a stepped annealing of the sample on a hotplate at 250°C for 30 minutes and then 300°C for 30 minutes, an asymmetric peak was observed around 380 nm (3.26 eV). The shift in photoluminescence was attributed to the effects of residual water remaining in the film after growth in an aqueous solution[82]. After annealing, residual $Zn(OH)_2$ was dehydrated and the remaining water was expelled from the film. With quenching defects from the ex-

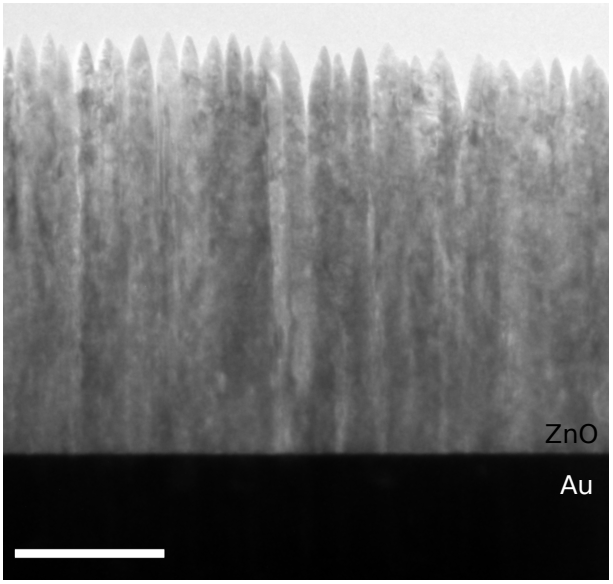

Figure 5.3.9: Bright field TEM of ZnO/Au cross-section. Columnar structures near the interface imply an island growth mechanism at the initial stages of film growth. The top part of the columns are due to thinning involved sample preparation. The original thickness of the film was several microns. Scale bar = 200 nm.

cess water eliminated by the short anneal, the annealed ZnO exhibited strong UV band edge photoluminescence, characteristic of high quality ZnO, with a small defect band centered around 600 nm.

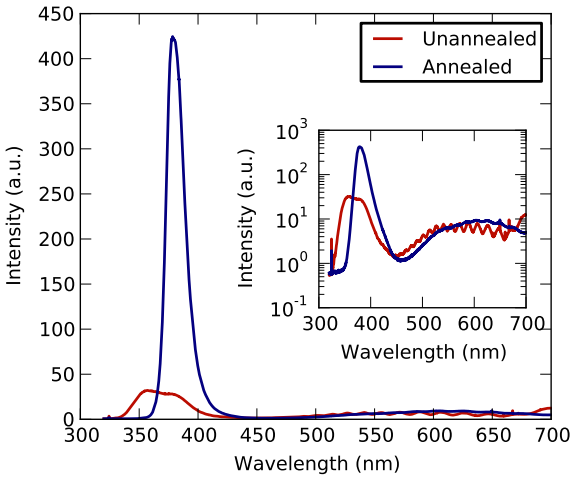

Figure 5.3.10: Effects of annealing on photoluminescence of ZnO grown on Au microplates. Photoluminescence spectra of ZnO grown on Au microplates as-grown and after a stepped anneal. The fast nucleation method was chosen to produce the ZnO film for this sample. Inset: Logarithmic-linear scale shows the effects of thin film interference in the defect band of the ZnO.

5.4 Conclusion

In summary, heteroepitaxial deposition of continuous ZnO films on single crystalline Au microplates through solution-based techniques has been demonstrated. Our method improves on previous work of epitaxial deposition of ZnO on Au by using a deposition technique without a need for electrical contacts and by obtaining a fully continuous and smooth film. Nucleation of the ZnO seed layer was also investigated and shown to dramatically affect the morphology of the resulting

film after growth. Our method of producing modular single crystalline ZnO/Au plates, which may be formed on a large range of substrates, can facilitate detailed study of metal - semiconductor junctions and new devices, such as microsystems-enabled photovoltaics[241], micron-scale metal/oxide catalysts, or fully epitaxial ZnO nanopiezoelectric generators[109]. These promising results will enable further studies of the electrical and optical properties of the epitaxial ZnO/Au junction.

6

Conclusions

In this work, we showed an example of how ZnO could affect the performance of a solar cell and critical methods to making controlled ZnO structures for future applications in optoelectronics. The incorporation of nanowire ZnO to create a nanostructured p-Cu_2O/n-ZnO junction improved the immediate performance of the solar cells. Carrier collection of minority carriers created in Cu_2O

increased as evidenced by the increase in short-circuit current, and the expansion of the wavelength range in which external quantum efficiency was substantial. We also showed that the movement of copper vacancies, the doping defect in Cu_2O, driven by the internal electric field could alter the performance of the solar cell over time. The ageing behavior was substantially different between nanowire and planar solar cells, which implies that future design of nanostructured solar cells must long term ageing effects.

The investigation of the effects of nanostructure ZnO/Cu_2O solar cells was made possible by controlling the morphology of ZnO made by aqueous solution growth. Only the solution parameters were changed, but even this allowed control in switching from planar to nanowire geometries. To further control ZnO structures to be applicable for more sophisticated optical devices, we used templated growth to obtain tall, undercut, hexagonal ZnO microdisks and precisely, placed, tapered ZnO nanowires. The purpose for the undercut, microdisk was to demonstrate the ability to create structures that could act as WGM cavities. The tapered ZnO nanowires could be used for enhancing extraction of photons emitted from a quantum dot on in a GaN device, providing a single photon source.

Epitaxy was critical for the controlled growth of these patterned structures. In these cases, the epitaxial substrate for ZnO was always a dielectric: GaN or $MgAl_2O_4$. It may be desirable to have a substrate that is metallic for some optoelectronic applications to have a reflecting interface, a high quality electrical contact, or to serve as a sacrificial layer. We produced single crystal Au plates to be used as epitaxial substrates for aqueously grown ZnO. The ZnO was confirmed to be epitaxial with

the underlying Au plates through EBSD and TEM. The morphology of the ZnO on the Au plates could again be controlled through solution chemistry (through the presence of citrate ions) and through the kinetics of growth.

We are hopeful that these advances in understanding the role of ZnO nanostructure in devices and in controlling ZnO structure during growth will enable advances in optoelectronic devices.

References

[1] J. Kilby, Miniaturized electronics circuits (1964).

[2] R. Noyce, Semiconductor device-and-lead structure (1961).

[3] Isi web of science (2013).

[4] S. Nakamura, T. Mukai, M. Senoh, *Japanese Journal of Applied Physics* **30**, L1998 (1991).

[5] S. Nakamura, *et al.*, *Japanese Journal of Applied Physics* **35**, L74 (1996).

[6] C. Bundesmann, R. Schmidt-Grund, M. Schubert, *Transparent Conductive Zinc Oxide: Basics and Applications in Thin Film Solar Cells*, K. Ellmer, A. Klein, B. Rech, eds. (Springer, Berlin, Germany, 2008), chap. 3, pp. 79–124.

[7] B. Monemar, *et al.*, *physica status solidi (b)* **245**, 1723–1740 (2008).

[8] A. Teke, *et al.*, *Physical Review B* **70**, 195207 (2004).

[9] C. R. Gorla, *et al.*, *Journal of Applied Physics* **85**, 2595 (1999).

[10] M. Martínez, J. Herrero, M. Gutiérrez, *Solar Energy Materials and Solar Cells* **45**, 75 (1997).

[11] F. Maldonado, A. Stashans, *Journal of Physics and Chemistry of Solids* **71**, 784 (2010).

[12] C. H. Park, S. B. Zhang, S.-H. Wei, *Physical Review B* **66**, 073202 (2002).

[13] T. M. Barnes, K. Olson, C. A. Wolden, *Applied Physics Letters* **86**, 112112 (2005).

[14] R. Triboulet, V. Munoz-Sanjose, R. Tena-Zaera, M. Martinez-Tomas, S. Hassani, *Zinc Oxide - A Materials for Micro- and Optoelectronic Applications*, N. Nickel, E. Terukov, eds. (Springer, Dordrecht, The Netherlands, 2005), chap. 1, pp. 3–14.

[15] M. Raula, M. H. Rashid, T. K. Paira, E. Dinda, T. K. Mandal, *Langmuir* **26**, 8769 (2010).

[16] S. Baruah, J. Dutta, *Science and Technology of Advanced Materials* **10**, 013001 (2009).

[17] S. Cho, S.-H. Jung, K.-H. Lee, *The Journal of Physical Chemistry C* **112**, 12769 (2008).

[18] T. L. Sounart, *et al.*, *Journal of the American Chemical Society* **129**, 15786 (2007).

[19] Z. Wang, X.-f. Qian, J. Yin, Z.-k. Zhu, *Langmuir* **20**, 3441 (2004).

[20] K. Ellmer, *Journal of Physics D: Applied Physics* **34**, 3097 (2001).

[21] K. Ellmer, *Transparent Conductive Zinc Oxide: Basics and Applications in Thin Film Solar Cells*, K. Ellmer, A. Klein, B. Rech, eds. (Springer, Berlin, Germany, 2008), chap. 2, pp. 35–78.

[22] E. M. Likovich, R. Jaramillo, K. J. Russell, S. Ramanathan, V. Narayanamurti, *Physical Review B* **83**, 075430 (2011).

[23] Y. Lu, P. Reyes, J. Zhong, H. Chen, *GaN and ZnO-based Materials and Devices*, S. Pearton, ed. (Springer, Berlin, Germany, 2012), chap. 13, pp. 361–411.

[24] X. Wen, W. Wu, Y. Ding, Z. L. Wang, *Journal of Materials Chemistry* **22**, 9469 (2012).

[25] X. Wang, J. Song, J. Liu, Z. L. Wang, *Science* **316**, 102 (2007).

[26] V. Anisimkim, M. Penza, A. Valentini, F. Quaranta, L. Vasanelli, *Sensors and Actuators B: Chemical* **23**, 197 (1995).

[27] T.-J. Hsueh, S.-J. Chang, C.-L. Hsu, Y.-R. Lin, I.-C. Chen, *Applied Physics Letters* **91**, 053111 (2007).

[28] P. I. Reyes, *et al.*, *IEEE Sensors Journal* **9**, 1302 (2009).

[29] O. Taratula, *et al.*, *Langmuir* **25**, 2107 (2009).

[30] Z. Zhang, *et al.*, *IEEE Transactions on Ultrasonics, Ferroelectrics and Frequency Control* **53**, 786 (2006).

[31] Y. Chen, *et al.*, *Journal of Electronic Materials* **38**, 1605 (2009).

[32] Z. Zhang, H. Chen, J. Zhong, G. Saraf, Y. Lu, *Journal of Electronic Materials* **36**, 895 (2007).

[33] M. McCune, W. Zhang, Y. Deng, *Nano Letters* **12**, 3656 (2012).

[34] J. Zhong, *et al.*, *Applied Physics Letters* **90**, 203515 (2007).

[35] A. H. Reading, J. J. Richardson, C.-C. Pan, S. Nakamura, S. P. DenBaars, *Optics Express* **20**, A13 (2011).

[36] V. L. Solozhenko, O. O. Kurakevych, P. S. Sokolov, A. N. Baranov, *The Journal of Physical Chemistry A* **115**, 4354 (2011).

[37] A. N. Baranov, *et al.*, *Chemistry of Materials* (2013).

[38] K. Ellmer, K. A, *Transparent Conductive Zinc Oxide: Basics and Applications in Thin Film Solar Cells*, K. Ellmer, A. Klein, B. Rech, eds. (Springer, Berlin, Germany, 2008), chap. 1, pp. 1–33.

[39] A. Klein, F. Sauberlich, *Transparent Conductive Zinc Oxide: Basics and Applications in Thin Film Solar Cells*, K. Ellmer, A. Klein, B. Rech, eds. (Springer, Berlin, Germany, 2008), chap. 4, pp. 125–185.

[40] C. Noguera, *Journal of Physics: Condensed Matter* **12**, R367 (2000).

[41] D. M. Bagnall, *et al.*, *Applied Physics Letters* **70**, 2230 (1997).

[42] M. Willander, *et al.*, *Materials* **3**, 2643 (2010).

[43] A. Janotti, C. G. Van de Walle, *Physical Review B* **76**, 165202 (2007).

[44] C. Klingshirn, *physica status solidi (b)* **244**, 3027–3073 (2007).

[45] Ü. Özgür, *et al.*, *Journal of Applied Physics* **98**, 041301 (2005).

[46] E. G. Bylander, *Journal of Applied Physics* **49**, 1188 (1978).

[47] M. Liu, A. Kitai, P. Mascher, *Journal of Luminescence* **54**, 35 (1992).

[48] D. Reynolds, D. Look, B. Jogai, H. Morkoç, *Solid State Communications* **101**, 643 (1997).

[49] F. Tuomisto, K. Saarinen, D. C. Look, *physica status solidi (a)* **201**, 2219–2224 (2004).

[50] F. Tuomisto, K. Saarinen, D. C. Look, G. C. Farlow, *Physical Review B* **72**, 085206 (2005).

[51] M. Willander, *et al.*, *Nanotechnology* **20**, 332001 (2009).

[52] A. B. Djurišić, Y. H. Leung, *Small* **2**, 944–961 (2006).

[53] A. B. Djurišić, *et al.*, *Nanotechnology* **18**, 095702 (2007).

[54] O. Schirmer, D. Zwingel, *Solid State Communications* **8**, 1559 (1970).

[55] D. Zwingel, *Journal of Luminescence* **5**, 385 (1972).

[56] D. Li, *et al.*, *Applied Physics Letters* **85**, 1601 (2004).

[57] K. H. Tam, *et al.*, *The Journal of Physical Chemistry B* **110**, 20865 (2006).

[58] L. E. Greene, *et al.*, *Angewandte Chemie International Edition* **42**, 3031–3034 (2003).

[59] M. Gomi, N. Oohira, K. Ozaki, M. Koyano, *Japanese Journal of Applied Physics* **42**, 481 (2003).

[60] C.-Y. Chen, *et al.*, *Pure and Applied Chemistry* **82**, 2055 (2010).

[61] Y. Gu, I. L. Kuskovsky, M. Yin, S. O'Brien, G. F. Neumark, *Applied Physics Letters* **85**, 3833 (2004).

[62] T.-B. Hur, Y.-H. Hwang, H.-K. Kim, *Applied Physics Letters* **86**, 193113 (2005).

[63] Y.-Y. Peng, T.-E. Hsieh, C.-H. Hsu, *Applied Physics Letters* **89**, 211909 (2006).

[64] N. E. Hsu, W. K. Hung, Y. F. Chen, *Journal of Applied Physics* **96**, 4671 (2004).

[65] A. B. Djurišić, *et al.*, *Advanced Functional Materials* **14**, 856–864 (2004).

[66] I. Shalish, H. Temkin, V. Narayanamurti, *Physical Review B* **69**, 245401 (2004).

[67] A. Hutson, *Journal of Physics and Chemistry of Solids* **8**, 467 (1959).

[68] G. Masetti, M. Severi, S. Solmi, *IEEE Transactions on Electron Devices* **30**, 764 (1983).

[69] O. Caporaletti, *Solar Energy Materials* **7**, 65 (1982).

[70] M. Miyake, H. Fukui, T. Hirato, *physica status solidi (a)* **209**, 945–948 (2012).

[71] M. Podlogar, *et al.*, *Advanced Functional Materials* **22**, 3136–3145 (2012).

[72] G. Xiong, *et al.*, *Applied Physics Letters* **80**, 1195 (2002).

[73] S. B. Zhang, S.-H. Wei, A. Zunger, *Physical Review B* **63**, 075205 (2001).

[74] S. B. Zhang, S.-H. Wei, A. Zunger, *Journal of Applied Physics* **83**, 3192 (1998).

[75] M. Caglar, S. Ilican, Y. Caglar, F. Yakuphanoglu, *Journal of Materials Science: Materials in Electronics* **19**, 704 (2008).

[76] E. Mollwo, *Zeitschrift für Physik* **138**, 478 (1954).

[77] D. G. Thomas, J. J. Lander, *The Journal of Chemical Physics* **25**, 1136 (1956).

[78] A. R. Hutson, *Physical Review* **108**, 222 (1957).

[79] D. C. Look, J. W. Hemsky, J. R. Sizelove, *Physical Review Letters* **82**, 2552 (1999).

[80] C. G. Van de Walle, *Physical Review Letters* **85**, 1012 (2000).

[81] D. M. Hofmann, *et al.*, *Physical Review Letters* **88**, 045504 (2002).

[82] N. Saito, H. Haneda, T. Sekiguchi, T. Ishigaki, K. Koumoto, *Journal of The Electrochemical Society* **151**, H169 (2004).

[83] J. J. Richardson, *et al.*, *Crystal Growth & Design* **11**, 3558 (2011).

[84] S. Y. Myong, S. I. Park, K. S. Lim, *Thin Solid Films* **513**, 148 (2006).

[85] O. Schmidt, *et al.*, *Japanese Journal of Applied Physics* **44**, 7271 (2005).

[86] B. Claflin, D. C. Look (AVS, 2009), vol. 27, pp. 1722–1725.

[87] C. H. Swartz, *Journal of Materials Research* **27**, 2205 (2012).

[88] R. J. Collins, D. G. Thomas, *Physical Review* **112**, 388 (1958).

[89] D. C. Look, B. Claflin, H. E. Smith, *Applied Physics Letters* **92**, 122108 (2008).

[90] D. Look, H. Mosbacker, Y. Strzhemechny, L. Brillson, *Superlattices and Microstructures* **38**, 406 (2005).

[91] P. F. Carcia, R. S. McLean, M. H. Reilly, G. Nunes, *Applied Physics Letters* **82**, 1117 (2003).

[92] J.-J. Wu, S.-C. Liu, *Advanced Materials* **14**, 215–218 (2002).

[93] X. W. Sun, H. S. Kwok, *Journal of Applied Physics* **86**, 408 (1999).

[94] D. Bagnall, *et al.*, *Journal of Crystal Growth* **184–185**, 605 (1998).

[95] P. F. Carcia, R. S. McLean, M. H. Reilly, *Applied Physics Letters* **88**, 123509 (2006).

[96] S. A. Studenikin, N. Golego, M. Cocivera, *Journal of Applied Physics* **84**, 2287 (1998).

[97] S. Peulon, D. Lincot, *Journal of The Electrochemical Society* **145**, 864 (1998).

[98] L. Spanhel, M. A. Anderson, *Journal of the American Chemical Society* **113**, 2826 (1991).

[99] E. Ohshima, *et al.*, *Journal of Crystal Growth* **260**, 166 (2004).

[100] K. Govender, D. S. Boyle, P. B. Kenway, P. O'Brien, *Journal of Materials Chemistry* **14**, 2575 (2004).

[101] L. E. Greene, *et al.*, *Nano Letters* **5**, 1231 (2005).

[102] M. Law, L. E. Greene, J. C. Johnson, R. Saykally, P. Yang, *Nature Materials* **4**, 455 (2005).

[103] I. V. Markov, *Crystal Growth for Begineers: Fundamentals of Nucleation, Crystal Growth and Epitaxy* (World Scientific, Singapore, 1995).

[104] U. Diebold, L. V. Koplitz, O. Dulub, *Applied Surface Science* **237**, 336 (2004).

[105] L. Vayssieres, K. Keis, S.-E. Lindquist, A. Hagfeldt, *The Journal of Physical Chemistry B* **105**, 3350 (2001).

[106] J. J. Richardson, F. F. Lange, *Crystal Growth & Design* **9**, 2570 (2009).

[107] Z. R. Tian, *et al.*, *Nature Materials* **2**, 821 (2003).

[108] I.-C. Yao, P. Lin, T.-Y. Tseng, *Nanotechnology* **20**, 125202 (2009).

[109] J. Volk, *et al.*, *Nanoscale Research Letters* **4**, 699 (2009). PMID: 20596319 PMCID: PMC2894249.

[110] D. Andeen, L. Loeffler, N. Padture, F. Lange, *Journal of Crystal Growth* **259**, 103 (2003).

[111] J. H. Kim, *et al.*, *Advanced Functional Materials* **17**, 463–471 (2007).

[112] D. B. Thompson, J. J. Richardson, S. P. DenBaars, F. F. Lange, *Applied Physics Express* **2**, 042101 (2009).

[113] D. Andeen, J. H. Kim, F. F. Lange, G. K. L. Goh, S. Tripathy, *Advanced Functional Materials* **16**, 799–804 (2006).

[114] J. H. Kim, D. Andeen, F. F. Lange, *Advanced Materials* **18**, 2453–2457 (2006).

[115] E. Becquerel, *Comptes rendus* **9**, 561–567 (1839).

[116] G. Carr, *The Economist* **The World in 2013** (2012).

[117] M. Bazilian, *et al.*, *Bloomberg New Energy Finance* (Bloomberg New Energy Finance, 2012).

[118] V. M. Fthenakis, *Renewable and Sustainable Energy Reviews* **8**, 303 (2004).

[119] P. Sinha, *et al.*, *Energy Policy* **36**, 381 (2008).

[120] C. Candelise, J. F. Speirs, R. J. Gross, *Renewable and Sustainable Energy Reviews* **15**, 4972 (2011).

[121] P. G. Loutzenhiser, O. Tuerk, A. Steinfeld, *JOM* **62**, 49 (2010).

[122] C. Wadia, A. P. Alivisatos, D. M. Kammen, *Environmental Science & Technology* **43**, 2072 (2009).

[123] B. A. Andersson, Material constraints on technology evolution: The case of scarce metals and emerging energy technologies, Ph.D. thesis, Chalmers University of Technology and Göteborg University, Göteborg, Sweden (2001).

[124] L. C. Olsen, R. C. Bohara, M. W. Urie, *Applied Physics Letters* **34**, 47 (1979).

[125] J. Herion, E. Niekisch, G. Scharl, *Solar Energy Materials* **4**, 101 (1980).

[126] E. Fortin, D. Masson, *Solid-State Electronics* **25**, 281 (1982).

[127] L. Olsen, F. Addis, W. Miller, *Solar Cells* **7**, 247 (1982).

[128] B. Rai, *Solar Cells* **25**, 265 (1988).

[129] P. Y. Yu, M. Cardona, *Fundamentals of Semiconductors: Physics and Materials Properties* (Springer, 2010).

[130] C. Malerba, *et al.*, *Solar Energy Materials and Solar Cells* **95**, 2848 (2011).

[131] L. M. Wong, *et al.*, *Journal of Applied Physics* **108**, 033702 (2010).

[132] M. Ichimura, Y. Song, *Japanese Journal of Applied Physics* **50**, 051002 (2011).

[133] B. Kramm, *et al.*, *Applied Physics Letters* **100**, 094102 (2012).

[134] M. J. Siegfried, K.-S. Choi, *Advanced Materials* **16**, 1743–1746 (2004).

[135] T. D. Golden, *et al.*, *Chemistry of Materials* **8**, 2499 (1996).

[136] H. Yu, J. Yu, S. Liu, S. Mann, *Chemistry of Materials* **19**, 4327 (2007).

[137] Z.-Z. Chen, *et al.*, *Journal of Crystal Growth* **249**, 294 (2003).

[138] Q. Pan, M. Wang, Z. Wang, *Electrochemical and Solid-State Letters* **12**, A50 (2009).

[139] A. Musa, T. Akomolafe, M. Carter, *Solar Energy Materials and Solar Cells* **51**, 305 (1998).

[140] R. N. Briskman, *Solar Energy Materials and Solar Cells* **27**, 361 (1992).

[141] J. Katayama, K. Ito, M. Matsuoka, J. Tamaki, *Journal of Applied Electrochemistry* **34**, 687 (2004).

[142] D. Zhang, Y. Liu, Y. Liu, H. Yang, *Physica B: Condensed Matter* **351**, 178 (2004).

[143] M. Izaki, *et al.*, *Journal of Physics D: Applied Physics* **40**, 3326 (2007).

[144] S. Jeong, A. Mittiga, E. Salza, A. Masci, S. Passerini, *Electrochimica Acta* **53**, 2226 (2008).

[145] A. T. Marin, *et al.*, *Advanced Functional Materials* p. n/a–n/a (2013).

[146] K. P. Musselman, A. Marin, L. Schmidt-Mende, J. L. MacManus-Driscoll, *Advanced Functional Materials* **22**, 2202–2208 (2012).

[147] M. Li, W. Wu, K. Liu, G. Hu, H. Xu, *Electrochimica Acta* **71**, 100 (2012).

[148] T. Gershon, K. P. Musselman, A. Marin, R. H. Friend, J. L. MacManus-Driscoll, *Solar Energy Materials and Solar Cells* **96**, 148 (2012).

[149] H. Wei, *et al.*, *CrystEngComm* **13**, 6065 (2011).

[150] K. P. Musselman, *et al.*, *Advanced Functional Materials* **21**, 573–582 (2011).

[151] J.-W. Chen, D.-C. Perng, J.-F. Fang, *Solar Energy Materials and Solar Cells* **95**, 2471 (2011).

[152] J. Zhang, W. Que, P. Zhong, G. Zhu, *Journal of Nanoscience and Nanotechnology* **10**, 7473 (2010).

[153] K. P. Musselman, *et al.*, *Advanced Materials* **22**, E254–E258 (2010).

[154] J. Cui, U. J. Gibson, *The Journal of Physical Chemistry C* **114**, 6408 (2010).

[155] Y. Nishi, T. Miyata, T. Minami, *Journal of Vacuum Science & Technology A: Vacuum, Surfaces, and Films* **30**, 04D103 (2012).

[156] B. M. Kayes, H. A. Atwater, N. S. Lewis, *Journal of Applied Physics* **97**, 114302 (2005).

[157] K. Yu, J. Chen, *Nanoscale Research Letters* **4**, 1 (2008). PMID: 20596408.

[158] A. Kandala, T. Betti, A. Fontcuberta i Morral, *physica status solidi (a)* **206**, 173–178 (2009).

[159] K. Hagedorn, C. Forgacs, S. Collins, S. Maldonado, *The Journal of Physical Chemistry C* **114**, 12010 (2010).

[160] Z. Yu, A. Raman, S. Fan, *Proceedings of the National Academy of Sciences* **107**, 17491 (2010).

[161] K. P. Musselman, Y. Ievskaya, J. L. MacManus-Driscoll, *Applied Physics Letters* **101**, 253503 (2012).

[162] H.-M. Wei, L. Chen, H.-B. Gong, B.-Q. Cao, *Journal of Inorganic Materials* **27**, 833 (2012).

[163] J. Maier, *Angewandte Chemie International Edition in English* **32**, 313–335 (1993).

[164] A. Mittiga, F. Biccari, C. Malerba, *Thin Solid Films* **517**, 2469 (2009).

[165] H. Raebiger, S. Lany, A. Zunger, *Physical Review B* **76**, 045209 (2007).

[166] D. O. Scanlon, B. J. Morgan, G. W. Watson, A. Walsh, *Physical Review Letters* **103**, 096405 (2009).

[167] F. Biccari, C. Malerba, A. Mittiga, *Solar Energy Materials and Solar Cells* **94**, 1947 (2010).

[168] D. O. Scanlon, G. W. Watson, *The Journal of Physical Chemistry Letters* **1**, 2582 (2010).

[169] A. Stokłosa, *Journal of Solid State Chemistry* **194**, 313 (2012).

[170] L. Y. Isseroff, E. A. Carter, *Chemistry of Materials* **25**, 253 (2013).

[171] C. Noguet, M. Tapiero, J. P. Zielinger, *physica status solidi (a)* **24**, 565–574 (1974).

[172] M. Tapiero, J. P. Zielinger, C. Noguet, *physica status solidi (a)* **33**, 155–166 (1976).

[173] J. P. Zielinger, C. Noguet, M. Tapiero, *physica status solidi (a)* **42**, 91–100 (1977).

[174] R. Haugsrud, T. Norby, *Journal of The Electrochemical Society* **146**, 999 (1999).

[175] A. Rakhshani, A. Al-Jassar, J. Varghese, *Thin Solid Films* **148**, 191 (1987).

[176] A. Mukhopadhyay, A. Chakraborty, A. Chatterjee, S. Lahiri, *Thin Solid Films* **209**, 92 (1992).

[177] P. E. de Jongh, D. Vanmaekelbergh, J. J. Kelly, *Chemistry of Materials* **11**, 3512 (1999).

[178] Mahalingam T., Chitra J.S.P., Rajendran S., Jayachandran M., Chockalingam M.J., *Journal of Crystal Growth* **216**, 304 (2000).

[179] S. Joseph, P. V. Kamath, *Solid State Sciences* **10**, 1215 (2008).

[180] T. E. Murphy, K. Moazzami, J. D. Phillips, *Journal of Electronic Materials* **35**, 543 (2006).

[181] J. A. v. Windheim, H. Wynands, M. Cocivera, *Journal of The Electrochemical Society* **138**, 3435 (1991).

[182] K. Mizuno, *et al.*, *Journal of The Electrochemical Society* **152**, C179 (2005).

[183] J. S. Christensen, H. H. Radamson, A. Y. Kuznetsov, B. G. Svensson, *Applied Physics Letters* **82**, 2254 (2003).

[184] K. H. Warnick, *et al.*, *Physical Review B* **84**, 214109 (2011).

[185] L. J. Brillson, *et al.*, *Journal of Vacuum Science & Technology B: Microelectronics and Nanometer Structures* **30**, 050801 (2012).

[186] I. Markevich, V. Kushnirenko, L. Borkovska, B. Bulakh, *Solid State Communications* **136**, 475 (2005).

[187] D. O. Scanlon, G. W. Watson, *Physical Review Letters* **106**, 186403 (2011).

[188] S. Ishizuka, S. Kato, Y. Okamoto, K. Akimoto, *Journal of Crystal Growth* **237–239, Part 1**, 616 (2002).

[189] S. Ishizuka, *et al.*, *Applied Surface Science* **216**, 94 (2003).

[190] G. Brown, B. Lindsay, *Solid-State Electronics* **19**, 991 (1976).

[191] M. Heinemann, B. Eifert, C. Heiliger, *Physical Review B* **87**, 115111 (2013).

[192] J. P. Reithmaier, *et al.*, *Nature* **432**, 197 (2004).

[193] J. J. Cole, X. Wang, R. J. Knuesel, H. O. Jacobs, *Advanced Materials* **20**, 1474–1478 (2008).

[194] J. Cui, U. Gibson, *Nanotechnology* **18**, 155302 (2007).

[195] J. J. Richardson, D. Estrada, S. P. DenBaars, C. J. Hawker, L. M. Campos, *Journal of Materials Chemistry* **21**, 14417 (2011).

[196] T.-U. Kim, J.-A. Kim, S. M. Pawar, J.-H. Moon, J. H. Kim, *Crystal Growth & Design* **10**, 4256 (2010).

[197] Y. Wei, *et al.*, *Nano Letters* **10**, 3414 (2010).

[198] C. Li, G. Hong, P. Wang, D. Yu, L. Qi, *Chemistry of Materials* **21**, 891 (2009).

[199] D. J. Gargas, *et al.*, *ACS Nano* **4**, 3270 (2010).

[200] D. Xu, W. Liu, S. Zhang, X. Shen, Z. Chen, *Optics Express* **21**, 3911 (2013).

[201] G. Zhu, *et al.*, *ACS Applied Materials & Interfaces* **4**, 6195 (2012).

[202] C. P. Dietrich, M. Lange, T. Böntgen, M. Grundmann, *Applied Physics Letters* **101**, 141116 (2012).

[203] L. Cai, S. Chen, X. Zhang, Y. Zhu, *Materials Letters* **89**, 327 (2012).

[204] C.-Y. Ni, *et al.*, *IEEE Journal of Quantum Electronics* **47**, 245 (2011).

[205] J. Dai, C. X. Xu, X. W. Sun, *Advanced Materials* **23**, 4115–4119 (2011).

[206] J. Dai, *et al.*, *Optical Materials* **33**, 288 (2011).

[207] J. Dai, C. X. Xu, X. W. Sun, X. H. Zhang, *Applied Physics Letters* **98**, 161110 (2011).

[208] R. Chen, B. Ling, X. W. Sun, H. D. Sun, *Advanced Materials* **23**, 2199–2204 (2011).

[209] S. S. Kim, Y.-J. Kim, G.-C. Yi, H. Cheong, *Journal of Applied Physics* **106**, 094310 (2009).

[210] C. Kim, Y.-J. Kim, E.-S. Jang, G.-C. Yi, H. H. Kim, *Applied Physics Letters* **88**, 093104 (2006).

[211] B. G. Wang, E. W. Shi, W. Z. Zhong, *Crystal Research and Technology* **33**, 937–941 (1998).

[212] H. F. Greer, W. Zhou, M.-H. Liu, Y.-H. Tseng, C.-Y. Mou, *CrystEngComm* **14**, 1247 (2012).

[213] Y.-H. Tseng, *et al.*, *Chemical Communications* **48**, 3215 (2012).

[214] Y. He, *et al.*, *The Journal of Physical Chemistry C* **117**, 1197 (2013).

[215] A. J. Shields, *Nature Photonics* **1**, 215 (2007).

[216] S. De Rinaldis, I. D'Amico, F. Rossi, *Physical Review B* **69**, 235316 (2004).

[217] C. Santori, *et al.*, *Applied Physics Letters* **87**, 051916 (2005).

[218] J. Claudon, *et al.*, *Nature Photonics* **4**, 174 (2010).

[219] R. T. Tung, *Proceedings of the 20th annual conference on the physics and chemistry of semiconductors interfaces* (AVS, 1993), vol. 11, pp. 1546–1552.

[220] K. J. Russell, T.-L. Liu, S. Cui, E. L. Hu, *Nature Photonics* **6**, 459 (2012).

[221] Y.-J. Lu, *et al.*, *Science* **337**, 450 (2012).

[222] J. P. S. Badyal, R. M. Nix, T. Rayment, R. M. Lambert, *Faraday Discussions of the Chemical Society* **87**, 121 (1989).

[223] K. Ip, *et al.*, *Journal of Crystal Growth* **287**, 149 (2006).

[224] M. Gwon, *et al.*, *Optics Express* **19**, 5895 (2011).

[225] B. J. Lawrie, R. Mu, R. F. Haglund, *Optics Letters* **37**, 1538 (2012).

[226] P. Li, Z. Wei, T. Wu, Q. Peng, Y. Li, *Journal of the American Chemical Society* **133**, 5660 (2011).

[227] P. Kundu, N. Singhania, G. Madras, N. Ravishankar, *Dalton Transactions* **41**, 8762 (2012).

[228] R. D. Vispute, *et al.*, *Applied Physics Letters* **73**, 348 (1998).

[229] M. Johnson, *et al.*, *Journal of Electronic Materials* **25**, 855 (1996).

[230] C. J. Palmstrom, *Annual Review of Materials Science* **25**, 389 (1995).

[231] Y. Yoshino, K. Inoue, M. Takeuchi, K. Ohwada, *Vacuum* **51**, 601 (1998).

[232] R. Liu, A. A. Vertegel, E. W. Bohannan, T. A. Sorenson, J. A. Switzer, *Chemistry of Materials* **13**, 508 (2001).

[233] S. J. Limmer, E. A. Kulp, J. A. Switzer, *Langmuir* **22**, 10535 (2006).

[234] B. Radha, M. Arif, R. Datta, T. Kundu, G. Kulkarni, *Nano Research* **3**, 738 (2010).

[235] B. Radha, G. U. Kulkarni, *Crystal Growth & Design* **11**, 320 (2011).

[236] J. J. Richardson, F. F. Lange, *Journal of Materials Chemistry* **21**, 1859 (2011).

[237] R. R. Dammel, *Diazonaphthoquinone-based Resists*, vol. TT11 of *SPIE Tutorial Texts in Optical Engineering* (SPIE Publications, Bellingham, Washington, 1993).

[238] Z. Lin, P. D. Bristowe, *Physical Review B* **75**, 205423 (2007).

[239] N. Jedrecy, G. Renaud, R. Lazzari, J. Jupille, *Physical Review B* **72**, 195404 (2005).

[240] J. Floro, J. Michael, L. Brewer, J. Hsu, *Journal of Materials Research* **25**, 1352 (2010).

[241] J. L. Cruz-Campa, *et al.*, *Solar Energy Materials and Solar Cells* **95**, 551 (2011).